Search for the $nn\Lambda$ state via the $^{3}\mathrm{H}(\mathrm{e},\mathrm{e}'\mathrm{K}^{+})\mathrm{X}$ reaction at JLab

Kazuki Suzuki

Abstract

In 2013, the existence of the $nn\Lambda$ bound state with a binding energy of about 0.5 MeV was claimed by the HypHI collaboration at GSI. Considering that the ground-state binding energy of hypertriton that is the isosinglet state (I = 0) is as small as 130 keV, the $nn\Lambda$ (I = 1) state is hard to be bound. In contrast, several theoretical calculations suggest the existence of a resonant state near the threshold. Therefore, it is desirable to conduct $nn\Lambda$ search experiments that can explore a wide range from the bound region to the resonance region. In the electro-production of hypernuclei, the $nn\Lambda$ state can be investigated by using a tritium target (pnn) by changing a proton to Λ. We performed a search experiment for the $nn\Lambda$ states using the ^{3}H$(e, e'K^+)$X reaction at the experimental Hall A in Jefferson Laboratory.

The experiment was performed using a 4.32-GeV electron beam. The momenta of the scattered electron and K^+ were measured by the existing spectrometers, HRS-L and HRS-R, respectively. The central momenta of the scattered electron and K^+ were set to cover the expected kinematics of $nn\Lambda$ production, which were 2.22 and 1.82 GeV/c, respectively. To estimate the various efficiency and correction factors required for cross-section analysis, a Monte Carlo simulation was newly developed to reproduce the experimental data in the framework of Geant4.

There seemed some enhancement around the energy threshold of the $nn\Lambda$ bound state in the cross-section spectrum for the ^{3}H(γ^*, K^+)X reaction. However, no clear peak structures were observed. Therefore, spectral fits with assumed peak position (B_Λ) and decay width (Γ) were performed to quantitatively discuss the excess above the expected background distribution. Typical theoretical predictions that show the small and large decay widths were used for the fits, which are $(-B_\Lambda, \Gamma) = (0.25, 0.8)$ MeV and $(0.55, 4.7)$ MeV. As a result of the fitting, no peak structure with a statistical significance exceeding 3σ was observed. The upper limit of the differential cross section at the 90%-confidence level was obtained to be 21 and 31 nb/sr, respectively, when $(-B_\Lambda, \Gamma) = (0.25, 0.8)$ and $(0.55, 4.7)$ MeV were assumed. In addition, the cross-section upper limit with various B_Λ and Γ other than the above fixed assumptions were obtained to provide data that are independent on the theoretical predictions.

The upper limit of the $nn\Lambda$ production cross section was obtained for the first time. In the theoretical calculations, the existence of the $nn\Lambda$ resonant state strongly depend on the models of the Λn interaction and calculation methods. The present result would constrain the interaction models and calculation methods. Theoretical calculations of the $nn\Lambda$ production cross section to be compared with the present result are highly desirable.

Contents

List of Tables

List of Figures

Chapter 1

Introduction

1.1 Baryon-Baryon Interactions

A nucleus is composed of protons and neutrons; they are called necleons. Nucleon–nucleon interactions are well understood through scattering experiments, and in the 1990s, several groups succeeded in constructing a realistic nucleon–nucleon interaction model that reproduced the scattering data in $\chi^2 \sim 1$ [1–3]. There exists only one two-body bound system, deuteron, which consists of a proton and a neutron. There are no bound systems in p–p and n–n systems. This property makes our present world as what it is today. If the nucleon forces were different from those in this universe, our world would be completely different, and there is a high possibility that stars and life would not be created. Is this exquisite fine tuning really a coincidence?

To answer this question, it is important to extend the world of SU(2), which consists of u-quarks and d-quarks, to the world of SU(3), which consists of u-quarks, d-quarks, and s-quarks. By adding one more degree of freedom, we can see nucleon interactions from a higher perspective view. The Λ particle is the lightest baryon that includes an s-quark, and it is important to understand the Λ-nucleon interaction. The Λ particle decays in only 263 ps, which makes scattering experiments difficult. Therefore, the interaction between Λ-particles and nucleons has been mainly obtained by creating Λ hypernuclei, which are bound states of Λ-particles and nucleons. Since the discovery of hypernuclei in 1953, numerous hypernuclei have been investigated.

1.2 Few body hypernulcear system

Many-body calculations based on the baryon-baryon interactions are available for few-body systems due to the recent improvements of super computer power. The ΛN interaction can be precisely extracted by comparing with the few-body hypernuclear structures. While these studies have yielded various results, new puzzles have arisen that cannot be explained by the simple ΛN interaction alone.

The established s-shell hypernuclei are $^{3}_{\Lambda}$H, $^{4}_{\Lambda}$H, and $^{4}_{\Lambda}$He. In the four-body (A = 4) system, two types of hypernuclei—$^{4}_{\Lambda}$H and $^{4}_{\Lambda}$He—have been found, and two states with spins of 0 and 1 have been measured, in each system. The existence of charge symmetry breaking (CSB) has been reported in recently developed high-precision measurements [4,5]. Figure 1.2 shows level schemes of the A = 4 hypernuclei. Although there is no CSB in the excited state with $S = 1$, there is a CSB of $\Delta B_{\Lambda} = 350$ keV in the ground state. Considering that $\Delta B(^3\text{He} - ^3\text{H}) = 70$ keV in ordinally nuclei, the effect of CSB is very large in hypernuclei. Any theoretical explanation for this effect has not yet been found, and further theoretical work is needed.

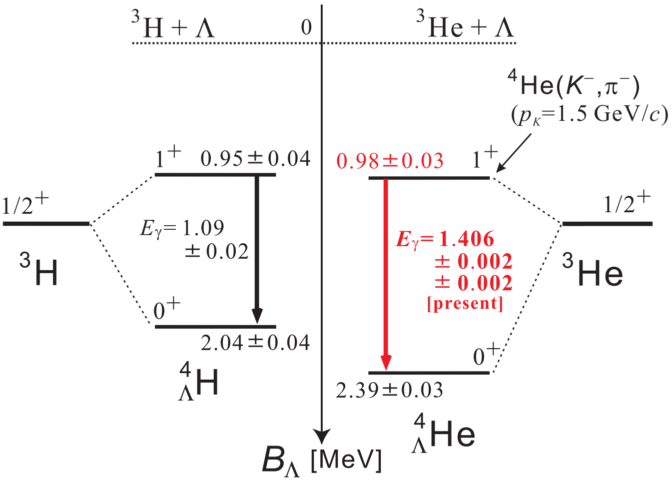

Figure 1.1 Level schemes of the A=4 hypernuclear system [5].

A currently established hypernucleus in the A = 3 system is $^{3}_{\Lambda}$H. $^{3}_{\Lambda}$H is the lightest hypernucleus consisting of p, n, and Λ with spin 1/2 and isospin 0. Its binding energy was measured to be $B_{\Lambda} = 130 \pm 50$ keV by emulsion experiments [6]. Considering that the binding energy of the deuteron composed of p and n is 2.22 MeV, we assume that $^{3}_{\Lambda}$H is a system in which the deuteron and Λ are weakly bound. In contrast, the recent STAR experiment using relativistic heavy ion collisions has claimed that $B_{\Lambda} = 0.41 \pm 0.12 \pm 0.11$ MeV [7], and further experimental confirmation is desirable. Given the shallow bound state of $^{3}_{\Lambda}$H, as shown in Fig. 1.2, the existence of other three-body hyper-nuclei ($NN\Lambda$) is unlikely. However, as mentioned above, there are still many puzzles left to be answered in few-body hypernuclei. ΛNN three-body forces or ΛN-ΣN conversion, which are not yet well understood, may be the key to solve these problems. Such effects may lead to the emergence of new bound and resonant states of $NN\Lambda$. In particular, the $NN\Lambda$ state with I=1 and S=1/2 has been an important topic in hyper-nuclear physics since the 2010s, starting from the experimental results by HypHI collaboration described in the next section.

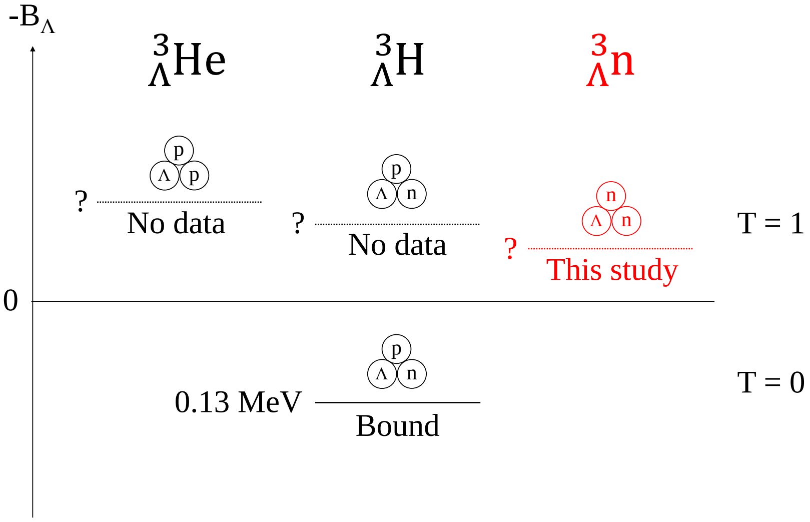

Figure 1.2 Level schemes of the A=3 hypernuclear system.

1.3 $nn\Lambda$ experiment by HypHI collaboration

The HypHI collaboration at GSI attempted to produce hypernuclei using a relativistic ion beam. A 2A GeV beam of ^{6}Li was irradiated onto a ^{12}C target. The initial goal of the experiment was to generate Λ, $^3_\Lambda$H, and $^4_\Lambda$H to demonstrate the feasibility of the production method. The results have been reported in Refs. [8–10]. In the same dataset, the $n\Lambda$ and $nn\Lambda$ bound states were searched by measuring $d+\pi^-$, $t+\pi^-$ invariant masses [11]. The results are shown in Figure 1.3. The upper figures show the invariant mass distributions of $d+\pi^-$, and the lower figures show the invariant mass distributions of $t+\pi^-$. On the left, the decay vertex was selected at $-10 < Z < 30$ cm, and on the right, at $-2 < Z < 30$ cm. Here, the target was set at $-6 < Z < -2$ cm. In this experiment, the existence of both bound states of $n\Lambda$ and $nn\Lambda$ is reported. In particular, the $nn\Lambda$ bound state was observed with a significance of 5.0σ in the wide Z region (b1) and 5.2σ in the narrow Z region (b2). The width at (b2) was 5.4 ± 1.4 MeV, and the binding energy was $-B_\Lambda = -0.5 \pm 1.1 \pm 2.2$ MeV.

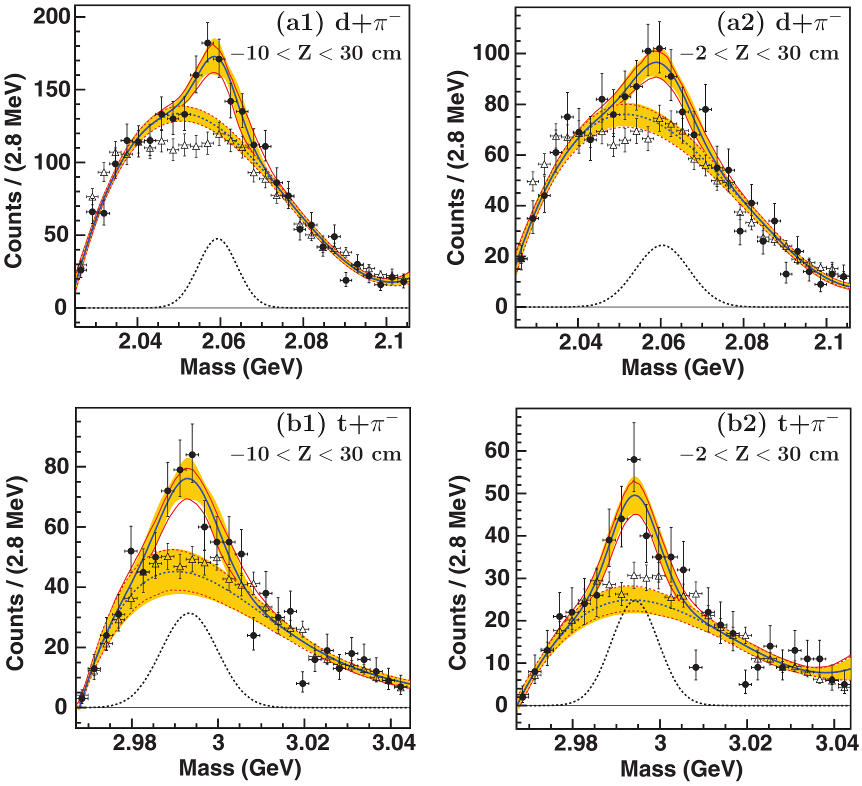

Figure 1.3 Invariant mass distributions of $d+\pi^-$ and $t+\pi^-$ at GSI [11]. The upper figures show $d+\pi^-$ and the bottom figures show $t+\pi^-$ invariant mass. The difference between the left and right is the production vertex cut.

1.4 Theoretical calculations for $nn\Lambda$ state

Various theoretical calculations have been performed to investigate the existence of the $nn\Lambda$ three-body system. If its binding energy is defined as $-B_\Lambda = M_{nn\Lambda} - 2M_n - M_\Lambda$, the observed state can be a bound state with $-B_\Lambda < 0$ or a resonant state with $-B_\Lambda > 0$. In the following sections, these two possibilities will be described for each of the theoretical studies so far. The details of the theoretical studies are summarized in Appendix A.

1.4.1 Bound state

Many calculations on the bound state of $nn\Lambda$ have been carried out by using various interaction models and techniques of few-body calculation. The currently established hypernuclei, in particular ${}^{3}_{\Lambda}$H, ${}^{4}_{\Lambda}$H, and ${}^{4}_{\Lambda}$He, were used as a reference to see whether the bound state of $nn\Lambda$ can exist or not.

The first theoretical calculation for a three-body system including hyperons was reported by Downs and Dalitz [12] in 1958, only six years after the discovery of the hypernuclei. The calculations were carried out with a variational method. They concluded that it is difficult to bound the $NN\Lambda$ system with I = 1. After that, the first calculation incorporating Λ-Σ conversion was performed by Miyagawa *et al.* [13]. Faddeev method was used to calculate the $NN\Lambda$ three-body system. The interaction due to Λ-Σ conversion was found to be attractive and played an important role in the binding of hypertriton. In the case of $(I, J) = (1, 1/2)$, which is the same quantum number as the $nn\Lambda$ state, it was also found to be attractive, but still not enough to bind it.

After the report by HypHI collaboration, theoretical calculations were carried out by Hiyama [14], Gal [15] and Garcilazo [16, 17] to explain the result with novel interaction models. They used different interactions and calculation methods. For instance, Hiyama *et al.* performed variational calculations with NSC97f as YN interaction which incorporate ΛN-ΣN coupling. Garcilazo *et al.* used the chiral constituent quark model to derive the interactions [16, 17]. In this model, a baryon is represented as a three-body cluster of constituent quarks, and its mass is generated by spontaneous breaking of chiral symmetry. The Faddeev equation was solved to calculate the $nn\Lambda$ bound state using this interaction. However, all calculations show that the existence of the bound state is difficult to explain within our current understanding of hypernuclei.

On the other hand, Ando *et al.* considered the possibility of $nn\Lambda$ bound states from the new perspective of Effimov states. The $nn\Lambda$ state was calculated by solving the coupled integral equation using pion-less effective field theory ($\not{\pi}$EFT) of the leading order [18]. As a consequence of the calculation, the possibility of the existence of Effimov states was suggested. However, since the experimental data to determine the parameters of three-body forces are very scarce, no quantitative discussion has been presented.

As mentioned above, almost all theoretical calculations have shown that the existence of bound states is difficult. Theoretical studies on bound states are summarized in Tab. 1.2.

1.4.2 Resonant state

Table 1.1 Theoretical calculation of complex resonance energies taken from Refs. [19].

Λn potential	A	B	C
E_0 (MeV)	0.551-$\frac{i}{2}$4.698	0.456-$\frac{i}{2}$4.885	-0.149-$\frac{i}{2}$5.783

A calculation of resonant states is more difficult than the bound state, so the calculation results are limited. The resonant states in $nn\Lambda$ three-body systems were studied by Belyaev *et al.* [19] for the first time. The resonant state was searched for by calculating the zeros of the three-body Jost function. Three Λn potentials were proposed by Nemura [20] *et al.*, denoted A, B, and C. Figure 1.4 shows the potential of the S-state under the assumption of these potentials. In all of them, there is a pocket of weak attraction. The results of the calculation with these potentials are shown in Tab. 1.1. It can be seen that there is a broad resonance in A and B, while there is no resonance in C.

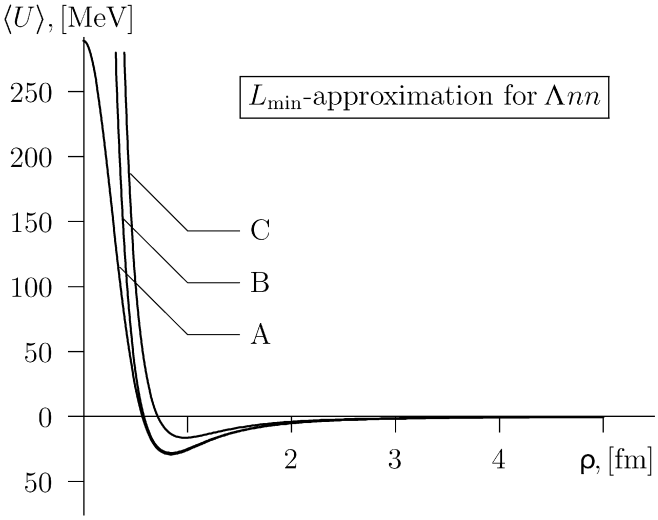

Figure 1.4 The hypercentral potential for the $nn\Lambda$ system [19]. The different Λn potentials are shown as A, B, and C.

Immediately after the HypHI report, three calculations on resonant states were reported by Afnan *et al.* [21], Filikhin *et al.* [22] and Kamada *et al.* [23]. They came to different conclusions. Afnan *et al.* performed a Faddeev calculation using a separate potential. The calculation result was $E = -0.107 - i0.622$ MeV, and no resonant state existed. However, by multiplying the strength of ${}^1S_0$, ${}^3S_1$ components by 1.05, a resonant state appeared. On the other hand, Filikhin reported a resonant state of rather wide width of $E = 0.2 - i1$ MeV with NSC97f potential. Kamada also reported a resonant state of $E = 0.25 - i0.40$ MeV with YN Nijmegen potential (Nijmegen89).

Theoretical calculations using the pionless effective field theory ($\not{\pi}$EFT) were recently reported by Schäfer *et al.* [24,25]. No $nn\Lambda$ bound state was found, but there existed a resonant state depending on the interaction. The interaction models NSC97f and Chiral EFT (NLO) showed the existence of resonant states, while Alexander B and Chiral EFT (LO) showed no resonant states. The pole position of the resonant state differs depending on the model, but it exists in the energy range of $E \leq 0.3$ MeV and the width range of $1.16 \leq \Gamma \leq 2.00$ MeV. These calculations on resonant states are summarized in Tab. 1.3.

Table 1.2 Theoretical calculations for the bound state.

Author	Method	YN interaction	Bound	Regards
Downs [12]	variational method	exponential	×	-
Miyagawa [13]	Faddeev	Nijmegen89	×	-
Hiyama [14]	variational method	NSC97f	×	-
Gal [15]	Faddeev	NSC97e,f	×	-
Garcilazo [16,17]	Faddeev	CCQM	×	-
Ando [18]	coupled integral equation	$\not{\pi}$EFT	△	Efimov state
Belyaev [19]	hyperspherical harmonics	Minesota	×	V ↑ 50% bound
Afnan [21]	Faddeev	Yamaguchi etc.	×	Λn ↑ 25% bound
Filikhin [22]	Faddeev	NSC97f	×	-
Kamada [23]	Faddeev	Nijmegen89	×	YN ↑ 20% bound

Table 1.3 Theoretical calculations of the resonant state.

Author	Method	YN interaction	Resonance	Regards
Belyaev [19]	hyperspherical harmonics	Minesota	○	-
Afnan [21]	Faddeev	Yamaguchi etc.	×	Λn ↑ 5% resonance
Filikhin [22]	Faddeev	NSC97f	○	-
Kamada [23]	Faddeev	Nijmegen89	○	-
Schäfer [24,25]	IACCC, CSM	NSC97f etc.	○	-

1.5 Current status of study on $nn\Lambda$ state

The present experimental data other than $nn\Lambda$ are consistent and does not accept the existence of $nn\Lambda$ bound state. As mentioned in the previous section, almost all theoretical calculations have shown that the existence of $nn\Lambda$ bound states is difficult. In contrast, many papers suggest the existence of $nn\Lambda$ resonant states, but there are large uncertainties in their binding energies and widths. Therefore, an experiment for investing $nn\Lambda$ state is desired.

There are many experimental difficulties in the $nn\Lambda$ production. It is difficult to detect neutron-rich hypernuclei such as $nn\Lambda$ in an emulsion experiment that captures trajectories. In the conventional counter experiments using (π^+, K^+) or (K^-, π^-) reactions, the unstable target (nnn) was required because the neutron is converted to Λ as shown in Fig. 1.5. Since the invariant mass methods such as the GSI experiment or emulsion methods detect weak decayed particles, only bound states can be searched for. Furthermore, since ion-beam reactions are rather new reactions to be used for hyper-nuclear productions, the feasibility of the reaction should be investigated.

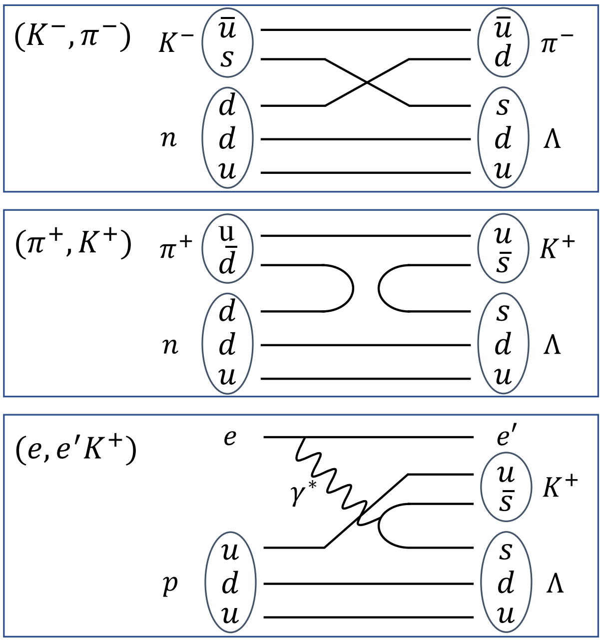

Figure 1.5 The reaction process of Λ production.

1.6 Our experiment

In this study, the electro-production of $nn\Lambda$ in the ^{3}H$(e, e'K^+)$X reaction is presented. Since the $(e, e'K^+)$ reaction converts a proton to Λ, the experiment can be performed using the ^{3}H target. The use of the ^{3}H target is very restricted due to its radioactivity. We can, however, use it at the Jefferson Laboratory (JLab) thanks to thorough safety control. JLab can provide electron beams with high accuracy. The advantages of hypernuclear production in the $(e, e'K^+)$ reaction are as follows:

- Excitation of spin-flipped states,
- Absolute energy measurement using the $p(e, e'K^+)\Lambda/\Sigma^0$ reactions,
- High mass resolution.

Figure 1.6 shows the momentum transfer of the Λ particle by (K^-, π^-), (K^+, π^+), and $(e, e'K^+)$ reactions. In the (K^-, π^-) reaction, where the momentum transfer is small, Λ is generated on the same orbit as the neutron causing the reaction. In contrast, in the $(e, e'K^+)$ reaction, the momentum transfer of Λ is large. It is relatively easy to produce a deeply bound state of Λ or spin-flipped states. In addition, the Λ (1115.683 ± 0.006 MeV) and Σ^0 (1192.642 ± 0.024 MeV) produced by the $p(e, e'K^+)\Lambda/\Sigma^0$ reactions can be used to accurately calibrate the mass. Since there is no appropriate target in the (K^-, π^-) and (π^+, K^+) reactions, the binding energy of $^{12}_{\Lambda}$C measured in the emulsion is used as a reference. The electron beam used in the $(e, e'K^+)$ reaction is a primary beam, which allows measurements with higher energy resolution than hadronic beams, which are secondary beams. Therefore, sub-MeV resolution has been achieved in previous experiments, and the best resolution can be achieved in counter experiments.

In contrast, the disadvantages of the $(e, e'K^+)$ reaction are as follows:

- Low production cross section,
- High background event due to electromagnetic reaction.

The $(e, e'K^+)$ reaction has a much lower cross section than the hadronic reaction due to the property of the electromagnetic reactions. This is compensated by using a high intensity electron beam at JLab. In addition, it is important to remove background events such as Mϕller scattering and bremsstrahlung, which occur at a very high rate. Even a very low fraction of background can be a serious problem since a very high intensity beam is required in electro-hypernuclear production.

Hypernuclear studies using electron beams started in 2000. Four experiments (E89-009 [26], E91-016 [27,28], E01-011 [29], E05-115 [30–34]) were performed in Hall C and one experiment (E94-107 [35]) was performed in Hall A to establish the hypernuclear production by the

$(e, e'K^+)$ reaction. In particular, in the most recent E05-115 experiment, various hypernuclei in the light- to medium-heavy nuclear regions were successfully produced, and a resolution of 0.5 MeV (FWHM) was achieved [30].

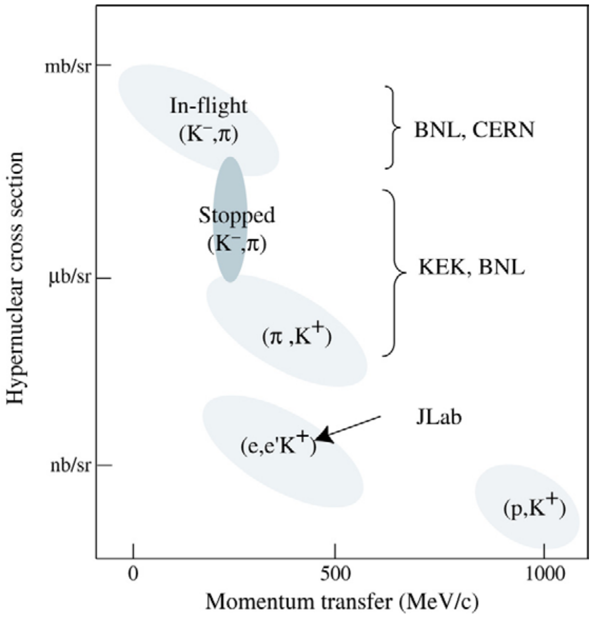

Figure 1.6 Momentum transfer and hypernuclear cross section for each Λ production process. The figure is taken from Ref. [36].

1.7 Purpose of this paper

Bound states of $nn\Lambda$ were reported by GSI collaboration, but the theoretical calculations are dominated by negative results. However, there are many positive theoretical calculations on the existence of the resonant state, and experimental results obtained using other methods are strongly desired. The counter experiment at JLab using the $(e, e'K^+)$ reaction is the only method that can produce $nn\Lambda$ in a missing-mass spectroscopy. This method has been established by experiments in the past 20 years, and bound and resonant states can be searched for with very high sensitivity.

In this study, we report the results of the cross section measurements of the $^3\text{H}(e, e'K^+)\text{X}$ reaction. In Chapter 2, the properties of the $(e, e'K^+)$ reaction and its experimental setup are described. After that, an analysis of the obtained data is performed in Chapter 3. In Chapter 4, Monte Carlo Simulations, necessary for the analysis of this experiment, are explained. Chapter 5 contains the results and discussion, and the summary is given at the end.

Chapter 2

Experiment

2.1 $(e, e'K^+)$ reaction

In the experiment, the Λ hypernucleus was produced by the $(e, e'K^+)$ reaction using the high-energy electron beam. A schematic diagram of this reaction is shown in Fig. 2.1. The electron beam is scattered from the target and virtual photons are emitted at a certain probability. Hyperons are produced by the reaction of a nucleon in the nucleus with the virtual photon. In this process, K^+s are produced to preserve strangeness. We measured the incident electron, scattered electron (e'), and K^+ in this experiment. By measuring the momentum and energy of these three particles, the mass of the hypernucleus M_X is reconstructed with the missing mass method, as follows:

$$M_X = \sqrt{(E_e + M_t - E_{e'} - E_K)^2 - (\vec{p}_e - \vec{p}_{e'} - \vec{p}_Y)^2}, \tag{2.1}$$

where $\vec{p}$ and E represent the momentum vector and the energy, and the subscripts show the particle. M_t is the mass of the target.

The hyperon was produced with the following elementary reactions,

$$\gamma^* + p \longrightarrow K^+ + \Lambda, \tag{2.2}$$

$$\gamma^* + p \longrightarrow K^+ + \Sigma^0, \tag{2.3}$$

$$\gamma^* + n \longrightarrow K^+ + \Sigma^-. \tag{2.4}$$

For the Λ hypernuclear production, Eq. (2.2) was used. In this reaction, a proton in the nucleus was converted to Λ. Other reaction methods such as (π^-, K^-), (K^+, π^+) convert a neutron to Λ. These various reactions can be used to perform complementary hypernuclear studies because there are only a limited number of stable nuclei that can be used as targets.

Furthermore, a major advantage of this reaction is that Λ and Σ^0 particles can be measured using a proton target, as shown in Eqs. (2.2) and (2.3). Since the masses of these particles have been measured very accurately, we can use these masses to achieve spectrometer calibration with high accuracy.

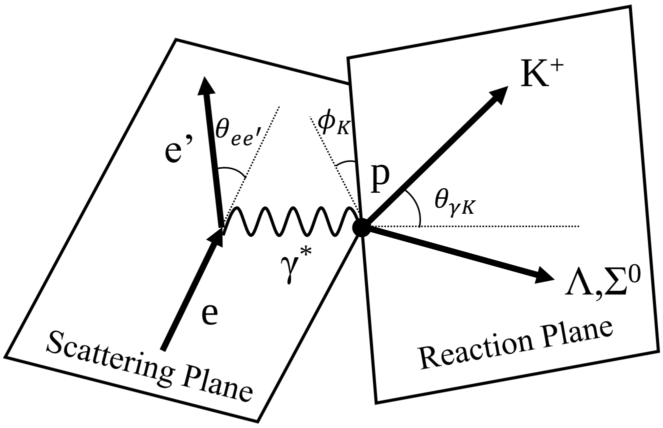

Figure 2.1 A diagram of $(e, e'K^+)$ reaction. The diagram assumes a one-photon approximation.

2.1.1 Kinematics

The triple differential cross section of $(e, e'K^+)$ reaction is defined as

$$\frac{d^3\sigma}{dE_{e'}d\Omega_{e'}d\Omega_K} = \Gamma\left(\frac{d\sigma_U}{d\Omega_K} + \epsilon_L\frac{d\sigma_L}{d\Omega_K} + \epsilon\frac{d\sigma_P}{d\Omega_K} + \sqrt{\epsilon_L(1+\epsilon)}\frac{d\sigma_I}{d\Omega_K}\right) \tag{2.5}$$

$$= \Gamma\left(\frac{d\sigma}{d\Omega_K}\right), \tag{2.6}$$

where σ_U, σ_L, σ_P, and σ_I are the unpolarized transverse, longitudinal, polarized transverse, and interference cross section, respectively [37–39]. Ω_e and Ω_K are the solid angle of the spectrometer for each particle. $d\sigma/d\Omega_K$ is the differential cross section for $(\gamma^{(*)}, K^+)$ reaction. Here, Γ is a parameter introduced to convert the cross section of electron-production to that of photo-production,

$$\Gamma = \frac{\alpha}{2\pi^2 Q^2}\frac{E_\gamma}{1-\epsilon}\frac{E_{e'}}{E_e}, \tag{2.7}$$

where α is the fine structure constant, E_γ is the effective photon energy ($E_\gamma = \omega + q^2/2m_p$), and Q^2 is defined as $Q^2 = -q^2$. The transverse polarization ϵ and longitudinal polarization

ϵ_L are defined as follows:

$$\epsilon = \left(1 + \frac{2|\vec{q}|^2}{Q^2}\tan^2\frac{\theta_{e'}}{2}\right)^{-1}, \tag{2.8}$$

$$\epsilon_L = \frac{Q^2}{\omega^2}\epsilon, \tag{2.9}$$

where ω and q are the energy and momentum of the virtual photon, which are defined as

$$\omega = E_e - E_{e'}, \tag{2.10}$$

$$\vec{q} = \vec{p}_e - \vec{p}_{e'}. \tag{2.11}$$

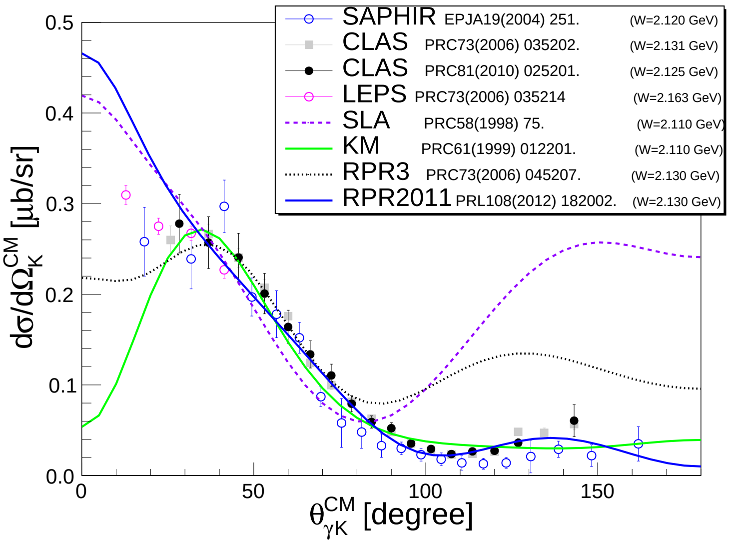

Figure 2.2 The angle dependence of the cross section of Λ photo-production [40].

The K^+ momentum in this experiment were determined to maximize the yield of Λ. The angular dependence of the $p(\gamma, K^+)\Lambda$ reaction [40] is shown in Fig. 2.2. The cross section increases in the forward region ($\theta^{\mathrm{CM}}_{\gamma K} \sim 0°$). Although there are few experimental data and the theoretical calculations depend on the calculation methods, most of them support an increase of the cross section in the very forward region. Therefore, we adopted $\theta^{\mathrm{CM}}_{\gamma K} \sim 0°$ as the central angle. The center-of-mass energy dependence of the $p(\gamma, K^+)\Lambda$ reaction cross section [41] at the forward angle ($\cos\theta^{\mathrm{CM}}_{\gamma K} = 0.9$) is shown in Fig. 2.3. The cross-section reaches the maximum around $W(= \sqrt{s}) = 1.8$ GeV and then gradually decreases in the higher energy region. To reduce the K^+ decay in a spectrometer, we adopted $W = 2.1$ GeV, which is a sightly larger energy region. The momentum of K^+ under these conditions is 1.82 GeV/c.

The virtual photon flux increases as it becomes more forward as shown in Eq. (2.7). At the same time, background events from bremsstrahlung and Mϕllor scattering also increase at the

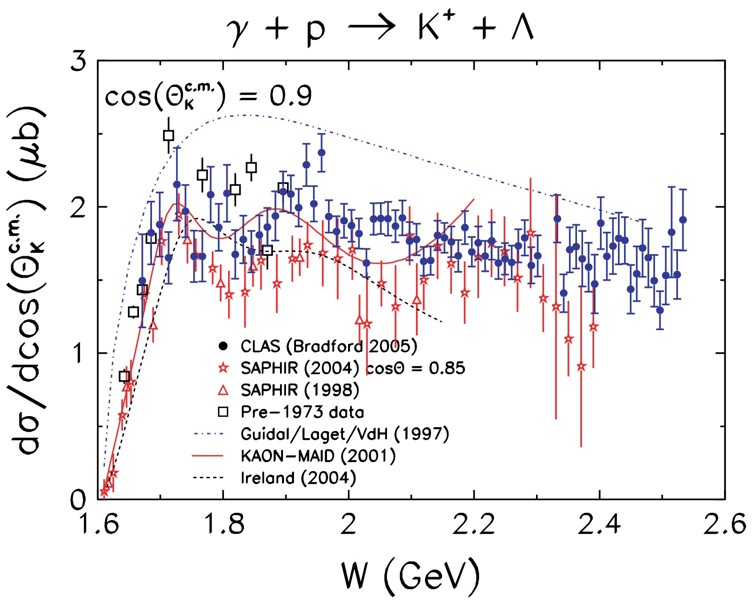

Figure 2.3 The energy dependence of the cross section of $p(\gamma, K^+)\Lambda$ reaction [41]. W(= $\sqrt{s}$) represents the center-of-mass energies.

forward region. Owing to the mechanical constraints of spectrometers, they can only move in a range over 12.5° relative to the beam. These background events are sufficiently small at this angle. Therefore, to set the $\theta^{\mathrm{CM}}_{\gamma K} \sim 0°$, the angle of the spectrometer was determined to be 13.2° for both the electron and K^+ measurements.

Under the kinematic range mentioned above, the momenta of e' and K^+ pair are plotted in Fig. 2.4. Each point is the pair of electron and K^+ momentum obtained by a simulation. The black points represent $^3\mathrm{H}(e, e'K^+)nn\Lambda$ events, the green points represent $p(e, e'K^+)\Lambda$, and the red points represent $p(e, e'K^+)\Sigma^0$ events. First, the central momentum of e' was set to cover the expected kinematics of $nn\Lambda$ production, which was 2.22 GeV/c. The kinematics setting is called the Physics-Mode ($M_{\mathrm{phys.}}$), and the momentum acceptance is shown with the red line in Fig. 2.4. We also used the $p(e, e'K^+)\Lambda$ and $p(e, e'K^+)\Sigma^0$ events as calibration. Since the $p(e, e'K^+)\Sigma^0$ event is almost out of acceptance in the Physics-Mode, we took data in the Calibration-Mode ($M_{\mathrm{calib.}}$). In this mode, the momentum of e' is reduced to 2.10 GeV/c. The momentum acceptance in the calibration mode is shown with the blue line in Fig. 2.4. Here, the momentum of e' instead of K^+ was lowered in the calibration-mode to avoid increasing the decay fraction of K^+. The parameters in these settings are listed in Tab. 2.1.

2.2 Electron beam provided by Jefferson Laboratory

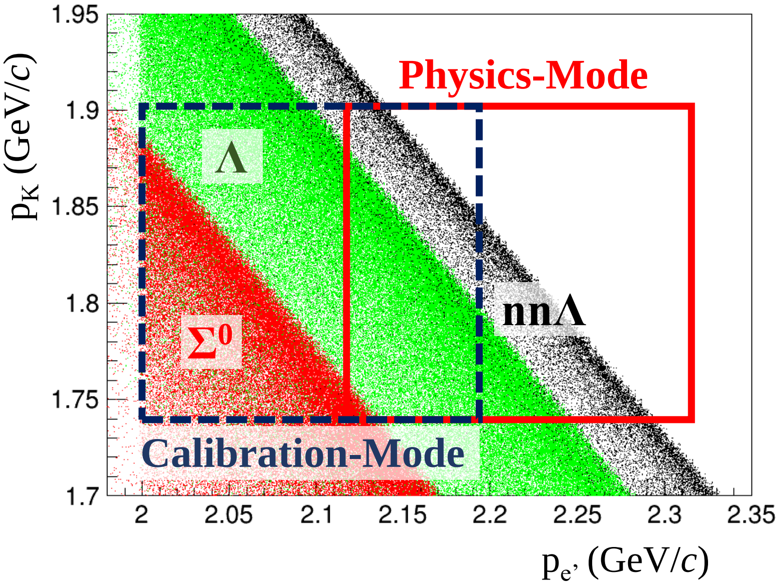

Figure 2.4 Momentum correlations of e' and K^+ for the reactions in this experiment. The $p(e,e'K^+)\Lambda$, $p(e,e'K^+)\Sigma^0$ and $^3\mathrm{H}(e,e'K^+)nn\Lambda$ reactions are shown in green, red and black dots, respectively. Blue dashed line and red solid line show the acceptances of the calibration ($M_{\mathrm{calib.}}$) and the physics modes ($M_{\mathrm{phys.}}$), respectively.

The experiment was carried out at the Thomas Jefferson National Accelerator Facility (JLab) in Virginia, USA. The continuous electron beam accelerator (CEBAF) at JLab was used to extract high-energy electrons. The electrons accelerated by the CEBAF accelerator are injected into one of four experimental Halls A, B, C, or D. Figure 2.5 shows the drawing of the CEBAF accelerator and four experimental halls.

2.2.1 CEBAF

The CEBAF can provide a continuous beam of 100% duty with an intensity of up to 200 μA. A schematic diagram of the CEBAF is shown in Fig. 2.5. First, the electrons are accelerated to 123 MeV by the injector. The electrons are then injected into a ring with a circumference of approximately 1400 m. The ring consists of two parts: a linear accelerator for acceleration and a circular ring for circumference. Each time the electrons passe through the linear accelerator, they are accelerated by 1.1 GeV and are ejected into each experimental hall. The orbiting ring consists of five different paths, and electrons take different paths depending on their

Table 2.1 Major reaction parameters of the present experiment. The $p(e,e'K^+)\Lambda$ reaction was assumed for calculations of $\sqrt{s}$ and the momentum transfer q.

	Calibration Mode ($\mathrm{M_{calib.}}$)	Physics Mode ($\mathrm{M_{phys.}}$)
Reaction	$p(e,e'K^+)\Lambda/\Sigma^0$	$p(e,e'K^+)\Lambda$ $^3\mathrm{H}(e,e'K^+)nn\Lambda$
$p_{e'}^{\mathrm{cent.}}$ (GeV/c)	2.100	2.218
$p_{K}^{\mathrm{cent.}}$ (GeV/c)	1.823	1.823
Q^2 (GeV/c)^2	0.479	0.505
$\theta_{e\gamma}$ (deg)	11.9	13.2
q (GeV/c)	0.497	0.389
$\sqrt{s}(=W)$ (GeV)	2.13	2.07
ϵ	0.769	0.794
ϵ_L	0.075	0.092

energy. The maximum energy was originally 6 GeV, but it was upgraded to 12 GeV. Electrons of 4.32 GeV were used in this experiment. The beam current was limited to 22.5 μA for the safety of the tritium target.

2.2.2 Beam measurement

In this section, the methods of measuring the position, direction, energy, and charge of the incident electron beam are described. The beam position was measured using the beam position monitor (BPM). Two BPMs were installed, located at 7.524 m and 1.286 m upstream of the target, respectively. The BPM consisted of four antennas, which were pointed in the direction of the beam. Each time the beam passed by, the BPM measured its voltage. This allows the BPM to achieve a position accuracy of 100 μm. The directions of the beam can also be determined using information from the two BPMs. Although the BPM is a nondestructive measurement device, the harp must first be used to calibrate the BPM, which is a destructive measurement. The harp was scanned in the direction perpendicular to the beam axis, and the absolute position was determined by reading the signal of the wire.

In this experiment, we adopted a raster system in which the electrons moved periodically in the x- and y-axes to avoid thermal effects on the target cell. The raster is caused by four dipole magnets placed 2 m upstream of the target. Two of each are used for the horizontal and vertical directions. The period is 25 kHz, and the electrons are shaken in the range of 2×2 mm^2. The BPM was used to compensate for this effect as shown in Sec. 3.4.2.

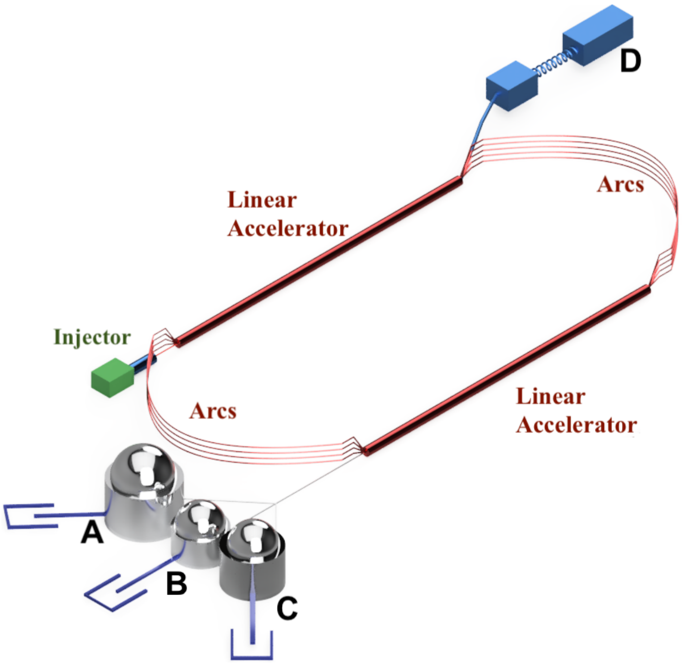

Figure 2.5 The schematic view of CEBAF [42].

The electron energy was measured using the arc method [42,43]. Dipole magnets were used to bend the electrons when they are transported from CEBAF to Hall A. Four harps, two each at the front and rear of the magnet, were installed. By measuring the position of the particle with the harp, the bending angle of the particle can be obtained. Furthermore, the energy of the electrons can be derived by measuring the integrated $B\Delta l$ of the magnet. Since the magnetic field of the magnets in the arc cannot be measured directly, another magnet (Ninth Dipole in Fig. 2.6), which is connected to the magnets in series with the power supply, is prepared externally. By constantly measuring this magnetic field, the energy of the electrons can be calculated.

The beam charge was measured using a beam current monitor (BCM). The BCM comprises an Unser Monitor located in the center with RF cavities located upstream and downstream. The amount of charge can be measured as an oscillation frequency. The advantage of Unser is that it is self-calibrated, but it cannot be used for a long period of time because the offset due to drift current changes in a few minutes. In contrast, RF is not self-calibrated, but it is very stable and can maintain an accuracy of 0.5% for several months. The BCM achieves high accuracy by combining these. First, the RF is calibrated using the results of the Unser calibration. This RF is then used to measure the amount of charge. This allows the amount of charge to be determined within an accuracy of 1.0 %.

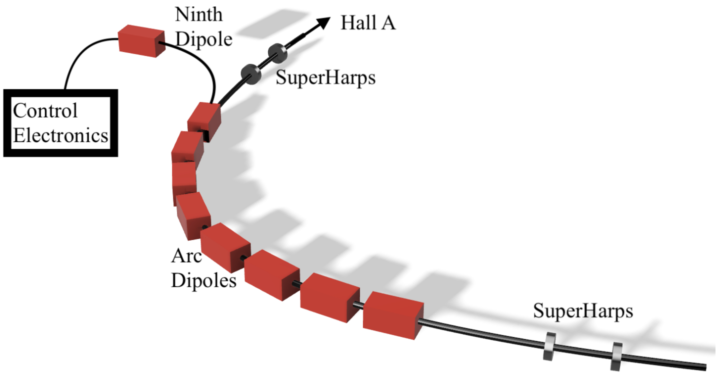

Figure 2.6 The schematic view of arc method [42].

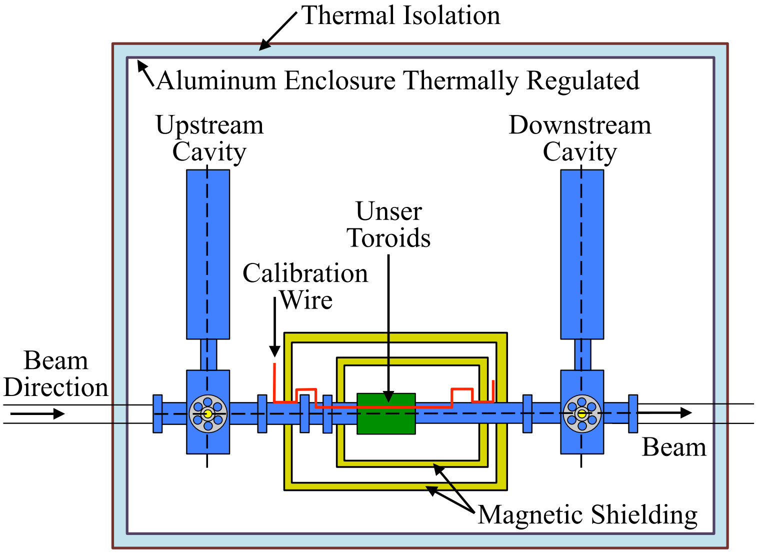

Figure 2.7 The schematic view of BCM. The figure is taken from Ref. [44]

2.3 Spectrometer

In Hall A, there are two existing spectrometers, High Resolution Spectrometers (HRSs). These two spectrometers have almost the same configuration; the one on the left is called HRS-L, and the one on the right is called HRS-R. A schematic diagram of the HRS installed in Hall A is shown in Fig. 2.8. We measured the scattered electron in HRS-L and K^+ in HRS-R.

The HRS was designed as a multipurpose spectrometer to achieve high momentum resolution ($\Delta p/p = 1.0 \times 10^{-4}$, FWHM) over a wide range of momentum (0.3–4.0 GeV/c). The configuration of the HRS spectrometer is shown in Tab. 2.2. The magnets used in HRS-L

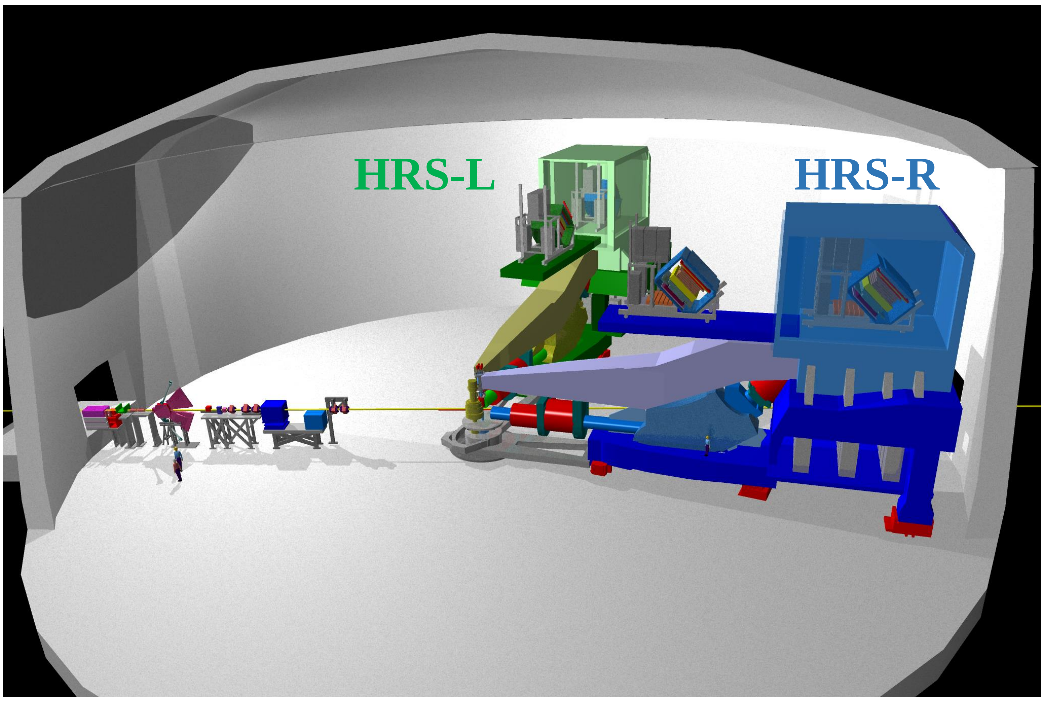

Figure 2.8 High Resolution Spectrometers in Hall A. The electron beam is directed from the left to right.

and HRS-R are identical. Both have a QQDQ configuration with three quadrupole magnets and one dipole magnet. Originally, the QQQDQQ configuration was required to achieve a high performance. Instead, by using an index dipole containing a Q component as D, sufficient performance with the QQDQ configuration could be achieved. Q1, Q2, D, and Q3 are superconducting magnets and are always cooled with liquid helium.

One of the most important features of this spectrometer is that it is vertically bent. A major advantage of vertical bending is that there is little deterioration in resolution when a long target is used in the beam axis direction. In horizontal bending, the momentum resolution deteriorates because the shift in the z-axis direction appears in the dispersive direction. In contrast, in vertical bending, the deviation in the beam axis direction appears as the deviation in the non-dispersive direction, which reduces the deterioration of resolution. Therefore, high resolution can be achieved even with a gas target such as the one used in this experiment. The experimental resolution is discussed in Sec. 5.2. A layout of the magnets is shown in Fig. 2.9.

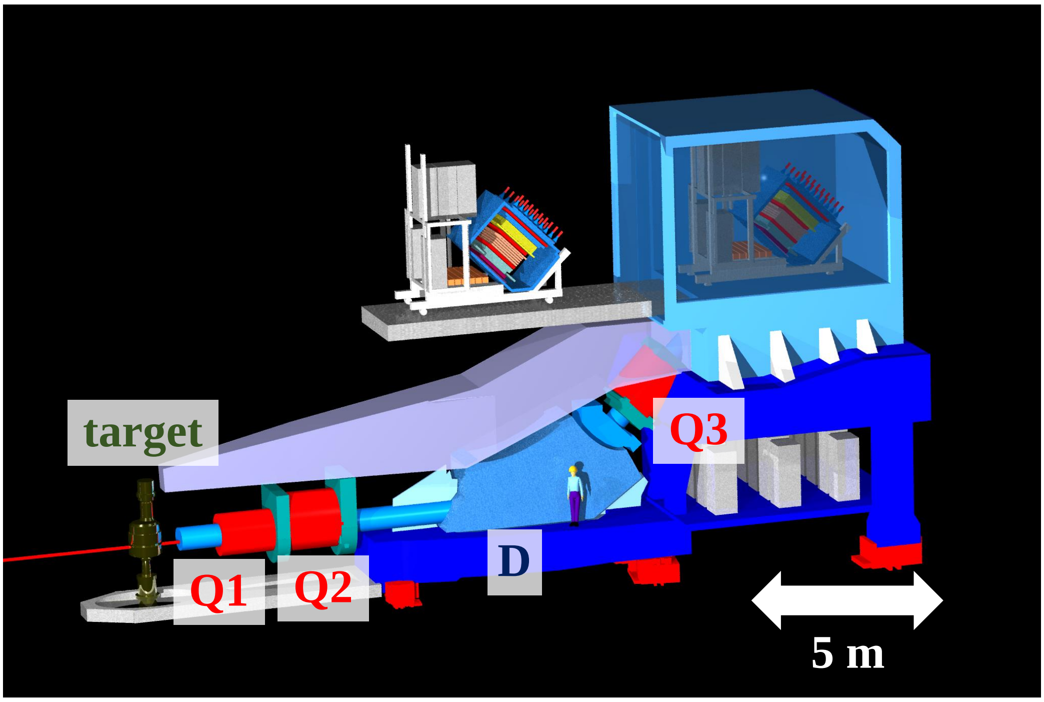

Figure 2.9 The magnetic configuration of HRS.

Table 2.2 Design value of HRS.

Bending angle	45°
Optical length	23.4 m
Momentum range	0.3–4.0 GeV/c
Momentum acceptance	$\lvert\delta p/p\rvert < 4.5\%$
Momentum resolution	$\Delta p/p = 1.0 \times 10^{-4}$ (FWHM)
Solid angle	6.0 msr

2.4 Target

The targets were tritium and hydrogen. In addition, ^{2}H, ^{3}He, empty and carbon targets were also installed. Since the tritium and hydrogen target are gaseous, a cigar-type cell with a length of 25 cm in the beam direction was used. Tritium was subject to very strict regulations due to its radiation. Therefore, a sealed-off type cell was used, which was designed to prevent gas leakage. The cell was cooled to 40 K to avoid cell breakdown due to heat, and the pressure at this condition was 0.3 MPa. The thickness of the gas was 84.8 ± 0.8 mg/cm^2 for tritium and 70.8 ± 0.4 mg/cm^2 for hydrogen. The heat generated in the target by the electron beam irradiation causes convection in the gas, which changes the local density of the target [45]. This will be discussed in Sec. 3.2.2. A picture of the target is shown in Fig. 2.10. Each target was set in the direction of gravity, and the electron beam was irradiated to the target by moving it in this direction.

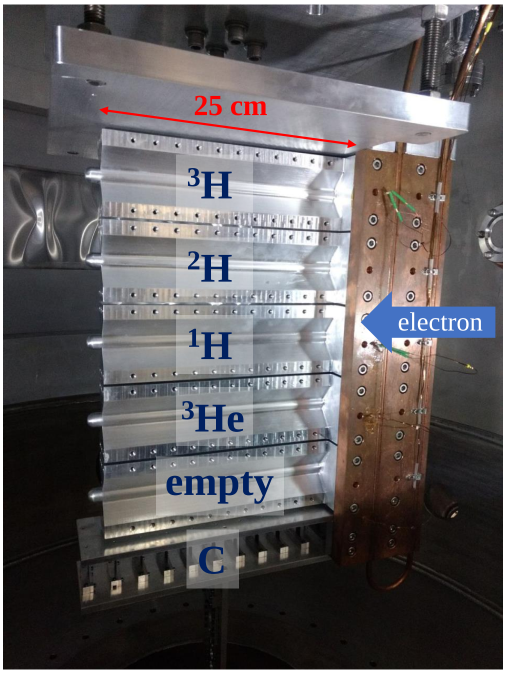

Figure 2.10 The target assembly used in this experiment. This figure is taken from [45].

2.5 Detectors

The charged particles entering the spectrometer were detected by a set of detectors located at the far end. Figure 2.5 shows an overview of the HRS-L and HRS-R detector array. Each uses mostly the same detectors, but the detectors for particle identification (PID) are different in the HRS-L and HRS-R.

Two identical vertical drift chambers (VDCs) are installed in front of the HRS-L detector array to reconstruct the momentum and angle of the particles by measuring their positions and angles. Scintillation counters, S0 and S2, are installed behind the VDCs. These are used to make the trigger and measure the timing of particles. Between S0 and S2, a gas Cherenkov detector is installed to remove π^-, which are background events. In HRS-R, VDCs, S0, and S2 are installed in the same configuration as in HRS-L. Instead of the gas Cherenkov detectors, two aerogel detectors (AC1 and AC2) are installed to remove π^+ and p background events.

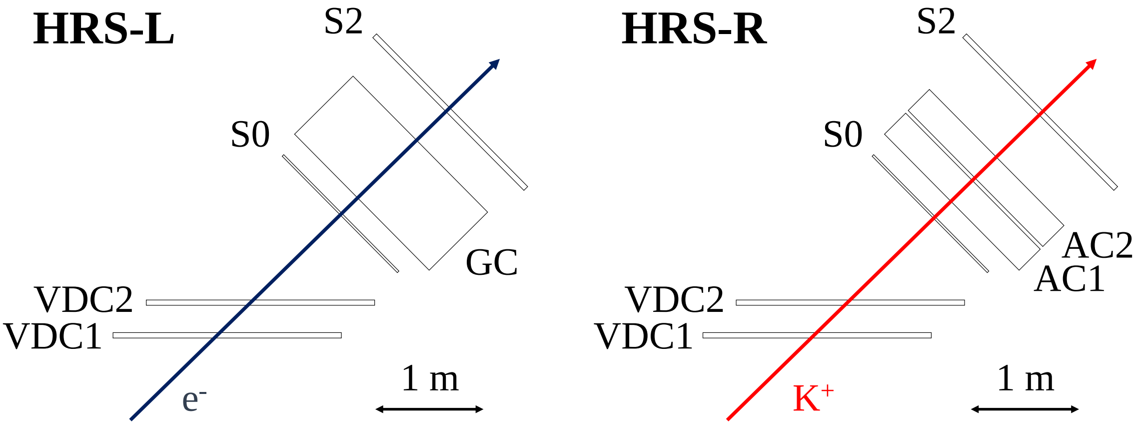

Figure 2.11 A schematic diagram of HRS detectors. Left and right figures show HRS-L and HRS-R detectors, respectively.

2.5.1 Tracking detectors

VDCs are used for particle tracking [46]. They are installed on the focal plane of the HRS optics. Each spectrometer has two VDCs—upper VDC and lower VDC—as shown in Fig. 2.12, which are placed horizontally at a distance of 33.5 cm. The central trajectory particle is incident on the VDC in the 45° direction since the particle is bent by the dipole magnet. The VDC consists of two layers, u- and v-layers 2.6 cm apart, and they are orthogonal to each other. 368 wires are attached at intervals of 4.24 mm, and the effective area is 211.8 cm in the dispersive direction and 28.8 cm in the non-dispersive direction. The VDCs have an applied voltage of -4 kV, and the gas composition is Ar (62%) and ethane (38%). The amount of material per VDC is 7.8×10^{-4} X_0 (radiation length). The position and angle resolution are $\sigma_{x(y)} \sim 100$ μm and $\sigma_{x'(y')} \sim 0.5$ mrad, respectively. Here, $x(, y)$, $x'(, y')$ are the position and angle of (non-)dispersive direction.

A special method called the cluster method was employed for particle tracking. VDCs are tilted in the direction of 45° relative to the direction of the particle trajectory, so that multiple wires coherently emit signals for a single particle. The number of wires that emit signals is an average of 3 ~ 7 wires for each particle. Since these wires emit signals in the order in which the particles pass, the time information can be used to determine the position and angle of the incident particles. Since this can be done in the u- and v-layers, the position and angle of the particle can be determined completely using a single VDC. The second VDC can also measure the position and angle of the particles and was used for a consistency check.

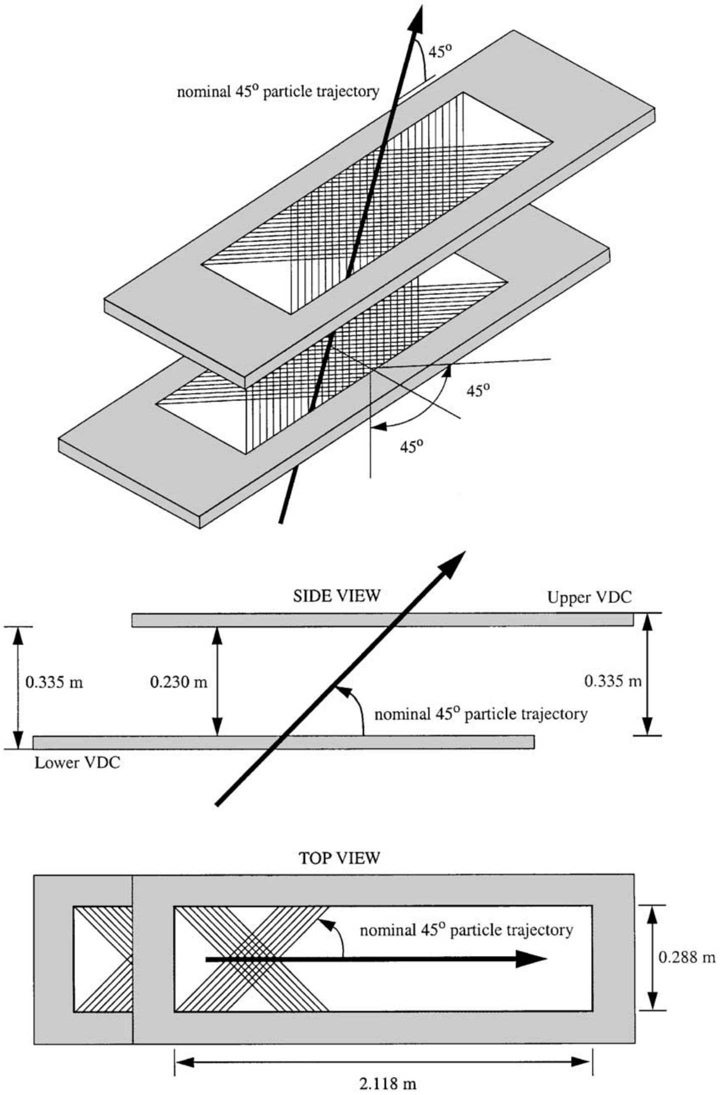

Figure 2.12 Schematic diagram of the vertical drift chamber [46].

2.5.2 Cherenkov counters

The measured particles were electrons in HRS-L and K^+ in HRS-R. However, a very large number of background events were also present. Therefore, Cherenkov detectors suitable for each spectrometer were installed.

The main background particles in HRS-L are π^-. Therefore, a gas Cherenkov detector (atmospheric pressure, $n = 1.00041$) filled with CO_2 was installed to reject π^- [47]. Since only electrons emit photons in the momentum region of this experiment ($2.1 \sim 2.3$ GeV), the π^- was rejected by selecting photon emission events. Basic information regarding the gas Cherenkov detector is shown in Tab. 2.3. The average of the number of photo-electrons at high energy electrons is approximately 7.3. The calculation results of the number of photo-electrons in the GC are shown on the left of Fig. 2.13. The momentum region of this experiment is shown by the gray shaded area.

The background particles for HRS-R are p and π^+. In general, the production cross section of K^+ is considerably low compared to the background particles, so a more powerful PID is required in HRS-R. Therefore, two aerogel Cherenkov detectors—AC1 and AC2—were installed [48]. The basic information of ACs is shown in Tab. 2.3. The average number of photo-electrons for high energy electrons is typically 8 for AC1 and 30 for AC2. The calculation results of the number of photo-electrons in AC1 and AC2 with the respective particles are shown in Fig. 2.13. The momentum region of this experiment (1.7 ~ 1.9 GeV) is shown by the gray shaded area. AC1 emits photons for π^+ and K^+ and AC2 for π^+.

Table 2.3 Basic information of the Cherenkov detectors.

	refractive index	radiator length (cm)	PMT	N_{PMT}
GC	1.00041	120	ET 9390 KB	10
AC1	1.015	9	Burle RCA 8854	24
AC2	1.055	5	Photonis XP 4572B	26

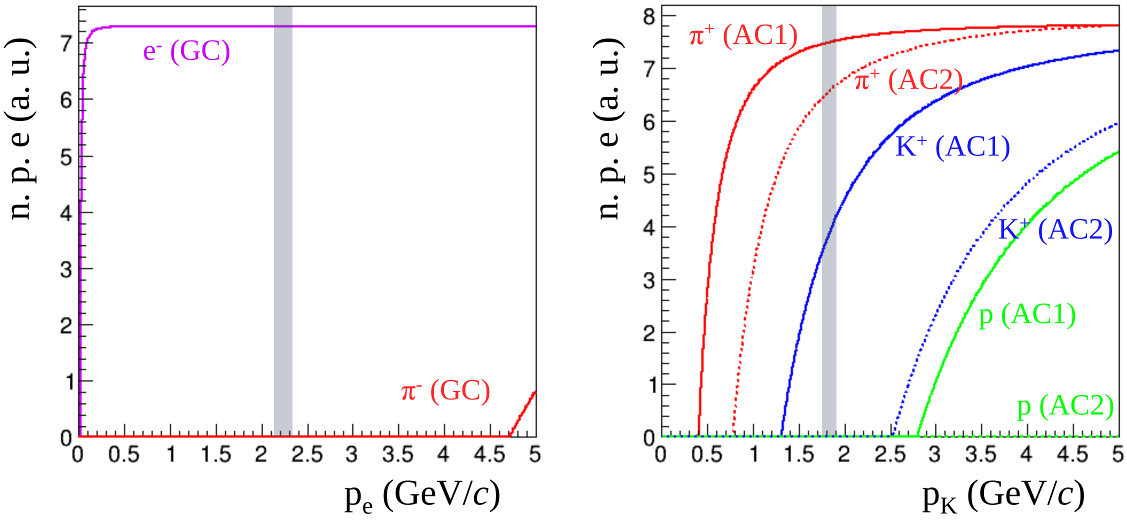

Figure 2.13 Momentum dependence of the number of photo-electrons in the Cherenkov detectors. Left and right show the number of photo-electrons of the gas Cherenkov (GC) detector and aerogel Cherenkov (AC) detectors, respectively. The gray shaded areas show the momentum region of this experiment.

2.5.3 Scintillation counters

There are two scintillation counters, S0 and S2. These were installed for particle timing information and triggering. S0 is one large plate made from plastic scintillator (BICRON 408) and is placed just after the VDC. The signal is read from PMTs (3-inch XP2312B) in both sides. The active area is 190 × 40 cm^2 and the thickness is 10 cm. S2 is located at the far end of the spectrometer. The timing information of S2 is used to calculate the coincidence time (Sec. 3.3.1). S2 is composed of 16 scintillators made from plastic scintillator (EJ-230). The schematic diagram is shown in Fig. 2.14. The signal is read from PMTs (2-inch Photonis 2282B) in both sides. The active area is 220 × 54 cm^2 and the thickness is 2 inch.

2.6 DAQ

Data from the detectors were taken using the FASTBUS and VME modules with ADC and TDC. The DAQ trigger was formed with NIM modules. These DAQ trigger events were processed with CODA (CEBAF Online Data Acquisition). The beam information was stored using EPICS software.

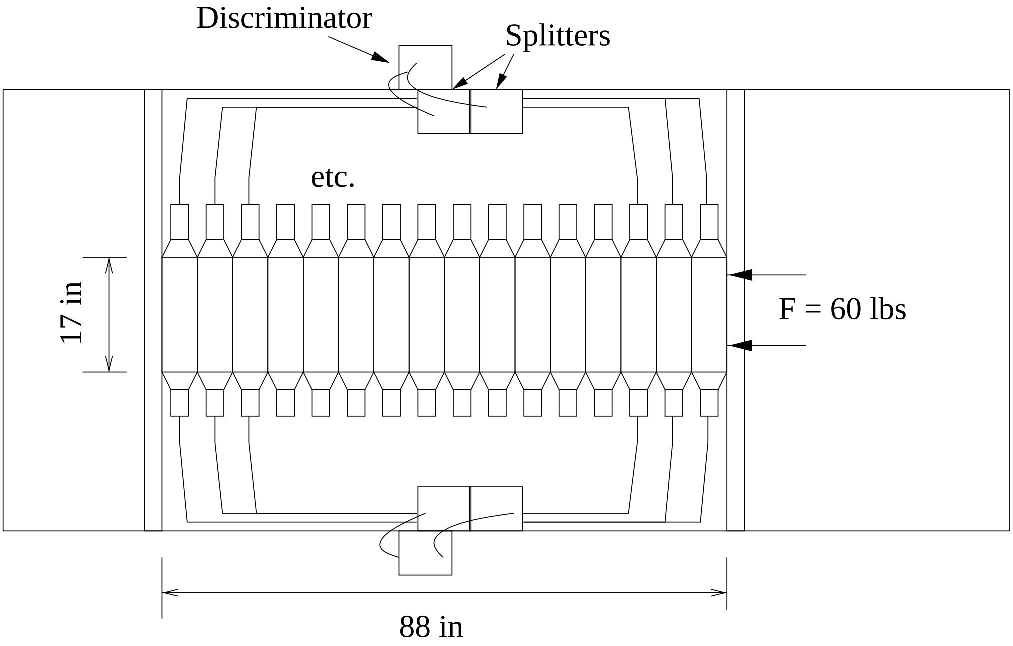

Figure 2.14 Schematic diagram of S2 [49].

The scintillators, S0 and S2, were used for triggering. The trigger conditions are shown in Tab. 2.4. T1 and T4 were used for data acquisition in a single arm. T1 is for HRS-L and T4 for HRS-R, and the condition for data acquisition is S0⊗S2 in each spectrometer. In contrast, T5 is the trigger for the coincidence condition, and the condition for data acquisition is that S0 and S2 of the left and right spectrometers emit the signal simultaneously. The main data were acquired by T5. T1 and T4 were acquired to measure the properties of the single spectrometer. These were acquired simultaneously with the T5 data. The rates were typically 1 kHz, 2 kHz, and 60 Hz for T1, T4, and T5, respectively. An overview of the trigger timing is shown in Fig. 2.6. The signal widths for S0 and S2 were set at 50 ns for HRS-L and 150 ns for HRS-R, respectively, and the timing was adjusted so that the HRS-L signal came later.

Table 2.4 Trigger condition.

T1	$(\mathrm{S0}{\otimes}S2)_{\mathrm{L}}$
T4	$(\mathrm{S0}{\otimes}S2)_{\mathrm{R}}$
T5	$(\mathrm{S0}{\otimes}S2)_{\mathrm{L}} \otimes (S0 \otimes S2)_{\mathrm{R}}$

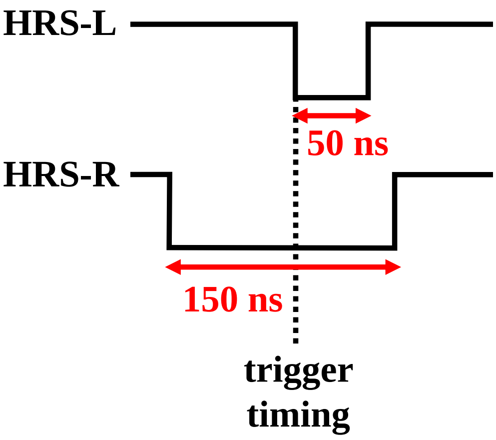

Figure 2.15 Trigger timing with T5 condition.

Chapter 3

Analysis

In this chapter, the detail of a data analysis to calculate the cross section of the ^{3}H$(e,e'K^{+})nn\Lambda$ reaction is described. First, the optics calibration to obtain the missing mass spectrum is explained. After that, event selections to improve the signal to noise ratio (S/N) are described. The efficiencies that originate from the various event selections and hardware specifications etc., and other correction factors are described. There are correction factors which need to be evaluated by using a Monte Carlo simulation. Details about the MC simulation, and the correction factors that we evaluated by the MC simulation are described in the next Chapter (Chap. 4).

3.1 Optics calibration

The missing mass was reconstructed with the following equation,

$$M_X = \sqrt{(E_e + M_t - E_K - E_{e'})^2 - (\vec{p_e} - \vec{p_k} - \vec{p_{e'}})^2}. \tag{3.1}$$

Here, $\vec{p}$ and E represent the momentum vector and the energy, and the subscripts show the particle. M_t is the mass of the target. The momentum and the angle at the production point were reconstructed with the backward transfer matrix (BTM) for which the inputs are the particles position and angle at VDC. The BTM is defined as follows:

$$x'_T = \sum_{a+b+c+d+e=0}^{n_1} C_{x'}(a,b,c,d,e) x^a x'^b y^c y'^d z_T^e \tag{3.2}$$

$$y'_T = \sum_{a+b+c+d+e=0}^{n_2} C_{y'}(a,b,c,d,e) x^a x'^b y^c y'^d z_T^e \tag{3.3}$$

$$p_T = \sum_{a+b+c+d+e=0}^{n_3} C_{p}(a,b,c,d,e) x^a x'^b y^c y'^d z_T^e, \tag{3.4}$$

where $x(,\ y)$, $x'(,\ y')$, p, z_T are the position and angle of (non-)dispersive direction, the momentum and the vertex positon along the beam direction. The angles x' and y' are defined as p_x/p_z and p_y/p_z, respectively. The variables with and without the subscript T are the ones at the production point and those at VDC, respectively. The n stand for the powers of each polynomial function. $C_{x',y',p}$ are the parameters to be optimized in the calibration.

At first, the production point z_T is required to calculate Eqs. (3.2), (3.3), (3.4). z_T is reconstructed with the following equation,

$$z_T = \sum_{a+b+c+d=0}^{n_4} C_z(a,b,c,d) x^a x'^b y^c y'^d \tag{3.5}$$

The parameters of Eq. (3.5) were optimized with carbon multi foil data. Ten thin foils (45 mg/cm^2) were placed at 2.5 cm intervals, and the reconstructed data are shown in Fig. 3.1. These optimizations were performed so that the events make peaks at the ideal foil positions. The MINUIT package in ROOT framework [50, 51] was used to minimize χ^2 of the result of Eq. (3.5). In this analysis, the 3rd-order parameters ($n_4 = 3$) were used.

The angle parameters of Eqs. (3.2) and (3.3) were calibrated with sieve slits, which have multi holes. A drawing of the sieve slit is shown in Fig. 3.2. The slit has two types of holes—large holes with a radius of 3.0 mm and small holes with a radius of 2.0 mm. There are two large holes, which are convenient for checking the direction. These slits were placed in front of the Q1 magnet and are shown in Fig. 3.3. Sieve-slit patterns of HRS-L and R with the initial parameters of Eqs. (3.2) and (3.3) are shown in Fig. 3.4. The black points show the position of the small hole, and red points show the position of the large hole. The reconstructed hole images at the sieve-slit for both HRS-L and HRS-R were not at the right position with the initial parameters. The parameter optimization needed to be performed taking into account the finite size of the beam and the finite thickness of target. The particle-position images at the sieve slits after the optimization are shown in Fig. 3.5 in which the right and left panels are for HRS-L and HRS-R, respectively. The hole image is much clear in HRS-L because the electrons have larger energy loss due to the radiation and more probability to be stopped in the slit plate compared to the hadron particles in HRS-R. The hadron particles punched through the sieve slit, and they caused large backgrounds in the HRS-R image. The 4th-order polynomials ($n_{1,2} = 4$) were used to optimize the angle parameters. Here, the parameters related to z_T were limited up to the second order; the parameters tuned to be zero if the power of z_T became more than 2.

Finally, missing mass distribution of the elementary process from the hydrogen target was used to optimize the momentum parameters of Eq. (3.4). Two spectrometer settings were used in the experiment: $M_{\text{phys.}}$ and $M_{\text{calib.}}$ as shown in Tab. 2.1. The $nn\Lambda$ production data were taken with $M_{\text{phys.}}$. However, only $p(e, e'K^+)\Lambda$ production which is the energy calibration

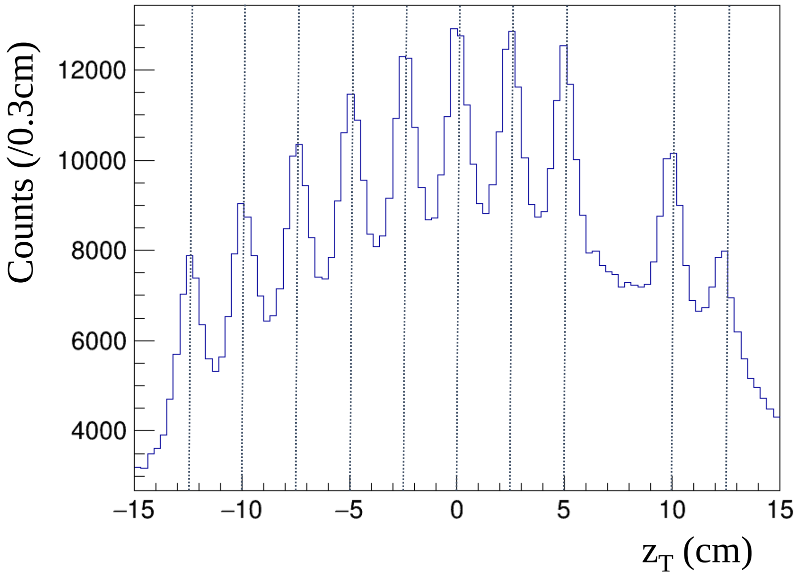

Figure 3.1 The carbon foil profile reconstructed with Eq. (3.5). Ten carbon foils were used as targets. The targets were placed at 2.5 cm intervals. No foil was placed at $z = 7.5$ cm.

source was in the acceptance. For purpose of better calibration, data with the lowered central momentum for e' detection ($M_{\mathrm{calib.}}$) were taken to simultaneously measure the Λ and Σ^0 productions as shown in Fig. 2.4. The parameters were tuned so that the events make Λ and Σ^0 peaks are at PDG values [52]. The missing mass distribution obtained by the optimization are shown in Fig. 3.6. The 5th order of polynomials ($n_3 = 5$) were used for the momentum. The parameters with the power of more than 2 for z_T were set to zero as were for the angle polynomial functions. It is noted that the parameters for the momentum function (Eq. (3.4)) in $M_{\mathrm{phys.}}$ and $M_{\mathrm{calib.}}$ are the same, but, for a conversion, a scale factor was applied by 2.218/2.210 which is the ratio of the central momentum settings. The missing-mass resolution of the peak of $p(e, e'K^+)\Lambda$ reaction after the all above calibrations was $\sigma = 1.3 \pm 0.1$ MeV/c^2 when a fit was performed with a Gaussian function over a range of $|\mathrm{M_X} - \mathrm{M_\Lambda}| < 2$ MeV/c^2.

3.2 Number of target nuclei

A gas target was enclosed in an aluminum cell with a length of 25 cm along the beam line. When the density is ρ mg/cm^2, the Avogadro number is N_A, and the atomic weight is A, the number of targets N_{targ} with the unit of cm^{-2} is expressed by the following equation:

$$N_{\mathrm{targ}} = \frac{\rho N_A}{\mathrm{A}} \tag{3.6}$$

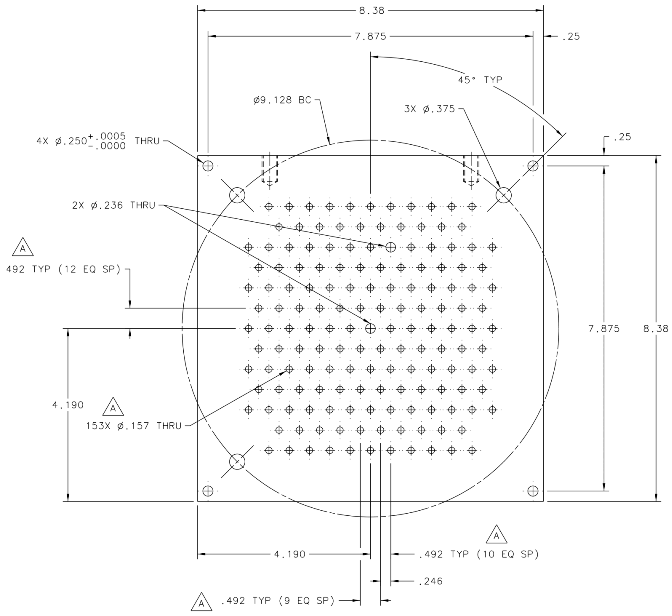

Figure 3.2 A drawing of the sieve slit.

The density of tritium gas was 84.8 ± 0.8 mg/cm^2 and A = 3.016 [53], so the number of target nuclei is $(1.69 \pm 0.02) \times 10^{22}$ cm^{-2}. The number of target nuclei used for the analysis were reduced from this value due to the vertex cut, effects of a density reduction and tritium decay as shown in the following sections (Sec. 3.2.1–3.2.3).

3.2.1 Vertex cut

The vertex z_T can be reconstructed for each spectrometer using Eq. (3.5). The vertex z_T reconstructed by using the tracking information of HRS-L is denoted as z_L, and the vertex z_T reconstructed by HRS-R as z_R. The vertex resolution can be improved by taking the average of both,

$$z_{\mathrm{mean}} = \frac{z_L + z_R}{2}. \tag{3.7}$$

Figure 3.7 shows the correlation between z_{mean} and $z_{\mathrm{diff}} = z_L - z_R$. The region in the red box corresponds to the events originating from the target nuclei, whereas the region in the black box corresponds to the events originating from the aluminum (Al) cell. The other events are considered to be accidental coincidence events originating from the cell and the target. The Al cell has atoms with the larger proton number than the gas target, which leads to the larger amount of electromagnetic background. In the region where z_{diff} is larger than the vertex

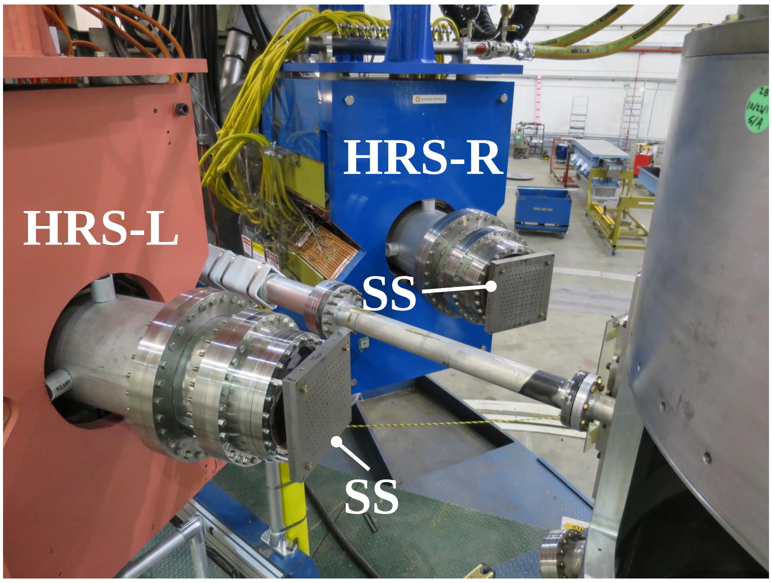

Figure 3.3 Picture of sieve slits set in front of the Q1 magnet. The sieve slits were removed in the production data taking.

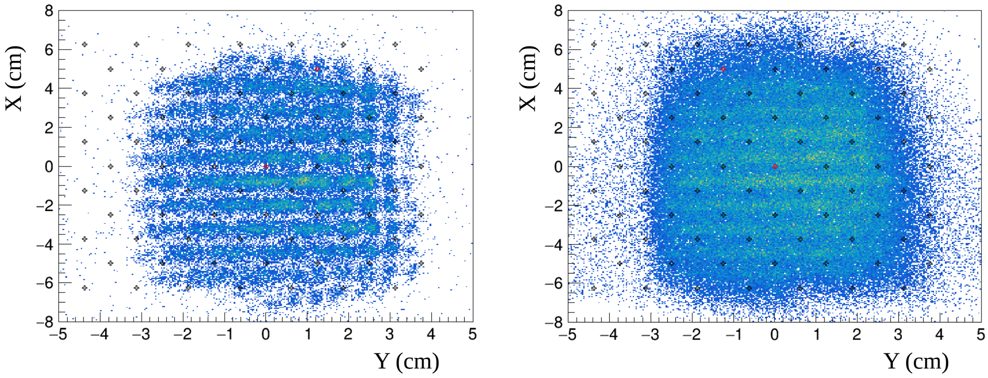

Figure 3.4 The sieve slit patterns reconstructed with the initial angle parameters of Eqs. (3.2) and (3.3). The left and right panels show the x vs. y images for HRS-L and HRS-R, respectively. The markers show the expected position of the hole. The black and red markers represent the positions for the small and large holes, respectively.

resolution, it consists of the following three elements of accidental coincidence:

$$\mathrm{Al}_{\mathrm{left}}\&\mathrm{Al}_{\mathrm{right}}, \tag{3.8}$$

$$\mathrm{Al}_{\mathrm{left}}\&\mathrm{Target}, \tag{3.9}$$

$$\mathrm{Al}_{\mathrm{right}}\&\mathrm{Target}. \tag{3.10}$$

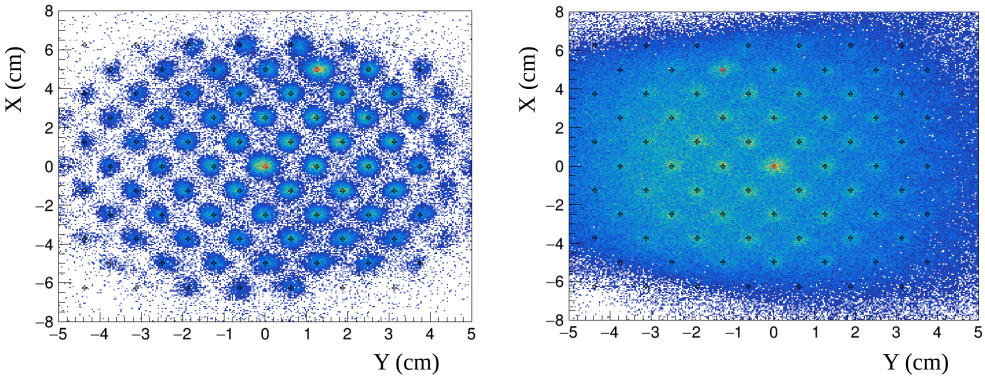

Figure 3.5 The sieve slit patterns reconstructed with the optimized parameters of Eqs. (3.2) and (3.3). Left and right panels show the x vs. y image for HRS-L and HRS-R, respectively. The markers show the expected position of the holes. The black and red markers represent the positions for small and large holes, respectively.

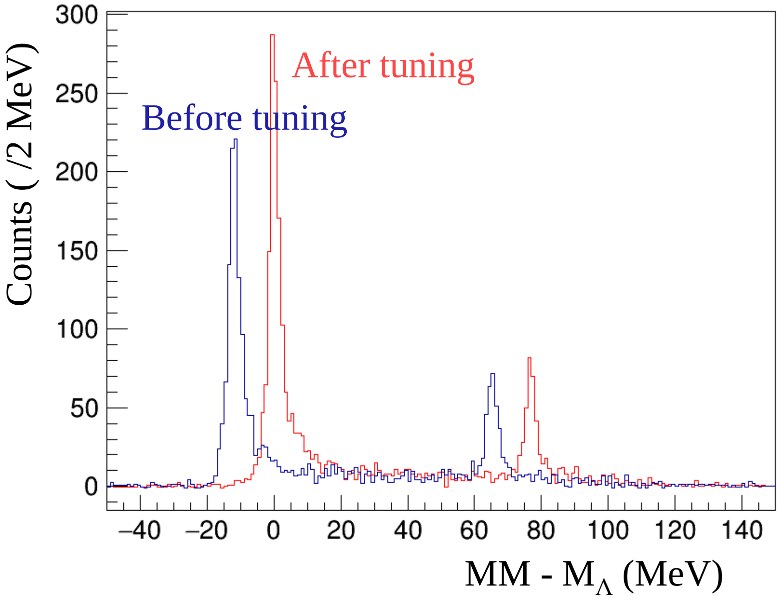

Figure 3.6 H$(e,e'K^+)\Lambda/\Sigma^0$ missing mass spectrum reconstructed by pre and post optimized parameters of Eq. (3.4).

Therefore, a cut condition of z_{diff} was required to remove these background events. The survival ratio due to the z_{diff} cut was estimated by using Λ production events from the hydrogen gas target. The $|z_{\text{diff}}|$ cut dependence of the survival ratio is shown in Fig. 3.8. In this analysis, the events in the range of $|z_{\text{diff}}| < 2.0$ cm were selected. This resulted in a target survival ratio of 84.3 ± 6.6%.

In addition, a z_{mean} cut was required to exclude the aluminum events from the entrance and

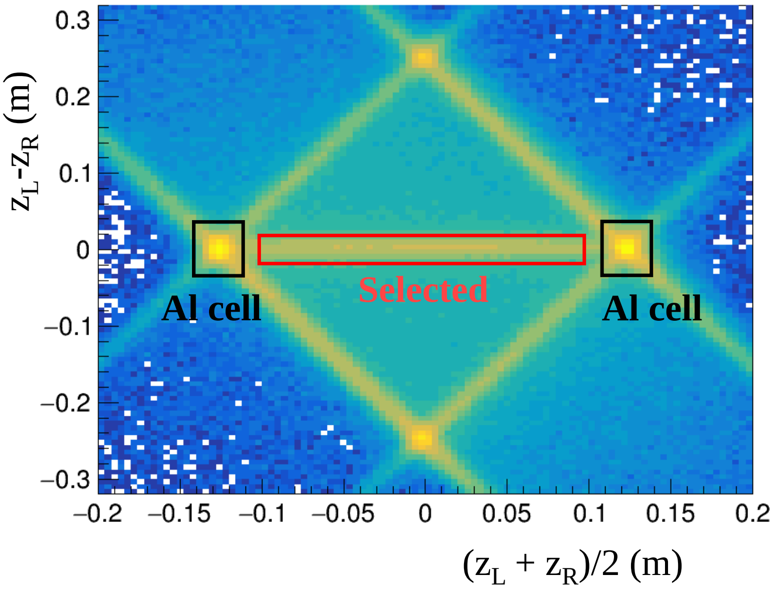

Figure 3.7 Correlation of subtraction $(z_L - z_R)$and average $(z_L + z_R)/2$ of the vertex profile in the log scale. The selected area and Al cell region are shown with red and black boxes, respectively.

exit of the Al cell. Figure 3.9 shows the z_{L} and z_{R} distributions when the above z_{diff} cut was applied. The peaks around ±12.5 cm are events from the Al cell, and those in between are events from the gas target. A spectral fit was performed to evaluate the survival ratio of the gas component after the Al-cell events are cut out with the z_T selection. A Gaussian function was assumed for events from the Al cell. For the gas target, a convolution of a quadratic function and a Gaussian function were used as shown in the following equation.

$$\mathrm{N(z)} = \int_{-\infty}^{\infty} dz f(z')G(z-z',\sigma) \tag{3.11}$$

where $f(z)$ is the quadratic function and $G(z-z',\sigma)$ denotes the Gaussian. We assumed that the width parameter of $G(z-z',\sigma)$ is the same as that of the Gaussian for the Al cell. Fit results for z_{L} and z_{R} are shown in Fig. 3.9. The thickness of the Al cell is thin enough ($\sim$ 400 μm) that the width of the Gaussian represents the vertex resolution. Obtained vertex resolution were $\sigma_{z_L} = 0.53 \pm 0.02$ cm and $\sigma_{z_R} = 0.50 \pm 0.02$ cm. Similarly, the vertex resolution for $\sigma_{z_{\mathrm{mean}}}$ was found to be 0.38 ± 0.02 cm. The survival ratio of the gas component as a function of $\mathrm{X}_{z_{\mathrm{mean}}}$ (; $|z_{\mathrm{mean}}| < \mathrm{X}_{z_{\mathrm{mean}}}$) is shown in the right panel of Fig. 3.10. The survival ratio was found to be 84.7 ± 0.8% with $\mathrm{X}_{z_{\mathrm{mean}}} = 10$ cm which is the condition used in the present analysis. The contamination of the Al-cell events was evaluated to be less than 0.1% relative to the remaining events in the case of $\mathrm{X}_{z_{\mathrm{mean}}} = 10$ cm.

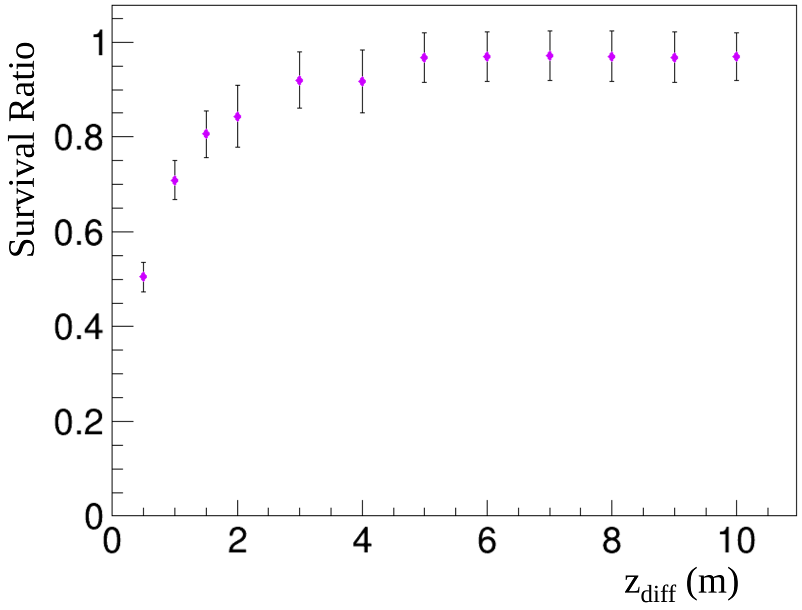

Figure 3.8 z_{diff} dependence of the survival ratio of the tritium target.

The excess of events can be seen on the left and right sides of the Al peaks. This is the area where the Gaussian function cannot represent the Al cell. Considering the possibility that this event also occurs inside the Al cell, we took this event as a systematic error. The difference between the data and the fitting function in the outer region of the cell was taken and inverted around the position of the cell, and the contamination rate was calculated assuming that the same amount of contribution from aluminum exists in the inner region of the cell. The systematic error of the survival ratio in this test was less than 0.1%. Combining the above cuts for z_{diff} and z_{mean}, the efficiency for vertex cuts was estimated to be 71.5 ± 5.6% and the Al contamination was less than 0.1% relative to the remaining events with these cuts.

3.2.2 Density change

The gas target was irradiated by a large number of electron beams. In this process, energy is lost at the cell entrance, cell exit and target, and heat of 15 W is produced. In contrast, the heat from tritium decay is negligible at 50 mW. The heat on the path of beam caused a density reduction of gas [45]. This effect depends on the beam current and target. The local density reaches equilibrium in a few seconds after the electron beam irradiates the cell, and if the current is constant, the local density remains constant.

This effect has already been estimated by measuring the electron scattering using HRS-

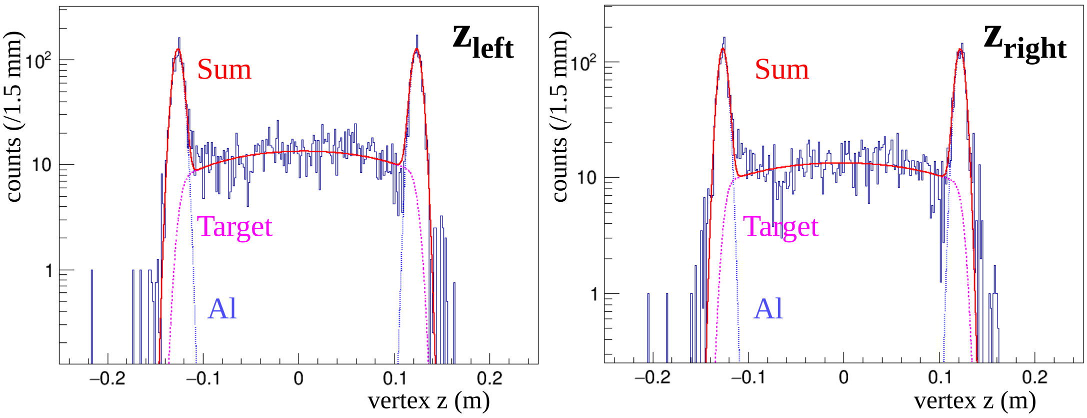

Figure 3.9 Distribution of z_L and z_R when z_{diff} cut was applied. The fitting results are also shown. See the text for the functions.

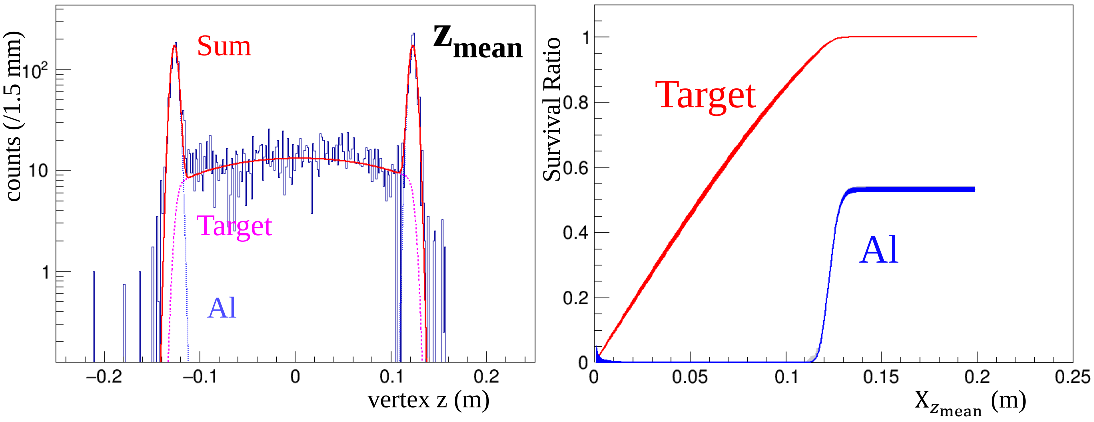

Figure 3.10 Survival ratio of the target with the z_{mean} cut. (Left) Distribution of z_{mean} (Right) Survival ratio of target and Al. These were calculated with the fitting result of the left figure.

L [45]. The density change of the gas was evaluated from a change of counting rate in the spectrometer. The results are shown in Fig. 3.11. The figure shows the density correction f when the beam current I_{beam} was set to one at 0 μA. The blue points are the data points, and the solid line is the value of the density correction f fitted by a quadratic function.

$$f(I_{\mathrm{beam}}) = aI_{\mathrm{beam}}^2 + bI_{\mathrm{beam}} + c \tag{3.12}$$

For the tritium target, $a = (1.06 \pm 0.36) \times 10^{-4}$, $b = (-6.8 \pm 0.89) \times 10^{-3}$, and $c = 1. \pm 0.003$. The 95% confidence interval due to statistical error is shown in the blue band, and the one including the systematic error is shown in the gray hatched area. This error is mainly due to the uncertainty in the current measurement of the BCM. The density is evaluated to be reduced to 0.901 ± 0.03 at the beam current of 22.5 μA.

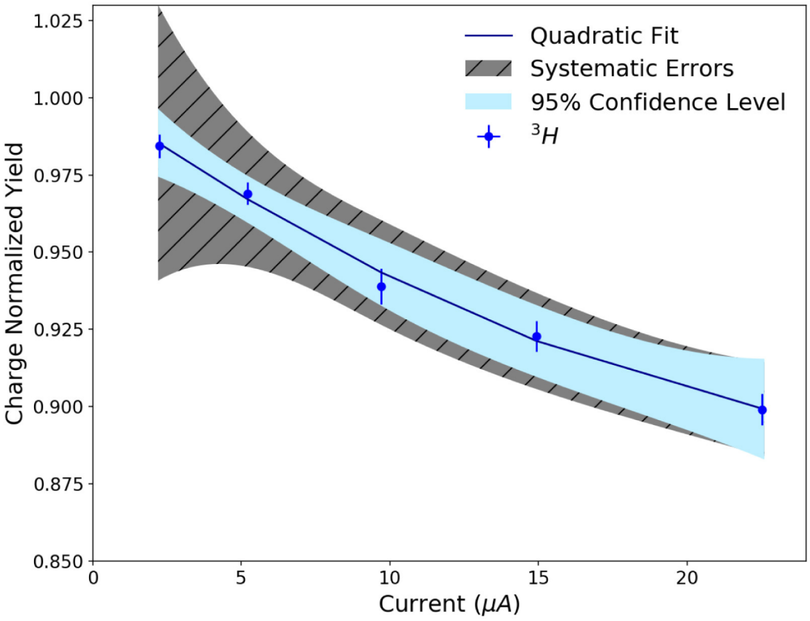

Figure 3.11 The change of the tritium gas density as a function of beam current. The local heat along the beam path caused the density reduction. The experiment for the $nn\Lambda$ measurement was performed at the beam current of 22.5 μA. The figure is taken from Ref. [45].

3.2.3 ^{3}H decay and contamination

Tritium nuclei decay in the weak decay mode as follows,

$$^{3}\mathrm{H} \longrightarrow {}^{3}\mathrm{He} + \mathrm{e}^{-} + \overline{\nu}_{\mathrm{e}}. \tag{3.13}$$

Therefore, the loss of the ^{3}H nuclei and the contamination of the ^{3}He nuclei need to be considered as

$$n_{^{3}\mathrm{H}}(t) = n^{0}_{^{3}\mathrm{H}} e^{-t/\tau_{^{3}\mathrm{H}}} \tag{3.14}$$

$$n_{^{3}\mathrm{He}}(t) = n^{0}_{^{3}\mathrm{He}} + n^{0}_{^{3}\mathrm{H}}(1 - e^{-t/\tau_{^{3}\mathrm{H}}}), \tag{3.15}$$

where $\tau_{^{3}\mathrm{H}}$ = (12.32 ± 0.02 years)/ln(2) is the lifetime of ^{3}H and n is the number of nuclei. The initial contamination of ^{3}He when the cell was filled with tritium gas was reported in Ref. [54];

$$\epsilon_{0} = \frac{n^{0}_{^{3}\mathrm{He}}(t)}{n^{0}_{^{3}\mathrm{He}}(t) + n^{0}_{^{3}\mathrm{H}}(t)} = 0.059\%. \tag{3.16}$$

Our experiment was conducted approximately 90 days after the gas was filled. From Eq. (3.14), we estimated that 1.4 ± 0.3% of the tritium had already decayed at the experiment.

^{3}He nuclei also produces a background event because a Λ is produced with the $p(e,e'K^+)\Lambda$ reaction. The ^{3}He contamination in the tritium cell was estimated to be 1.4 ± 0.3% from Eq. (3.15). The number of ^{3}He shown above is the number of nuclei and must be multiplied by the cross-section ratio. For this, we refer to Ref. [55]. This reports the Fermi momentum dependence of the proton in R(p) = $\sigma_{^3\mathrm{He}}(p)/\sigma_{^3\mathrm{H}}(p)$. We calculated the weighted average of R according to the Fermi momentum of tritium nucleus [56] and estimated as $\mathrm{R_{ave}} = 2.12 \pm 0.03$. The number of ^{3}He events in the $^3\mathrm{H}(e,e'K^+)X$ reaction was estimated to be 3.0 ± 0.7%.

The tritium cell also contained a small amount of hydrogen nuclei. The Λ production events from the hydrogen target produce a broad peak at $-B_\Lambda = 40 \sim 50$ MeV on the $^3\mathrm{H}(e,e'K^+)\mathrm{X}$ spectrum and does not affect the region of interest ($-B_\Lambda = -20 \sim 20$ MeV). It is noted that the events can be used for energy calibration as shown in Sec. 5.3.2.

3.3 Particle identification

Various particles other than electron and K^+ enter the HRS-L and HRS-R. In the HRS-L, π^- is major background, and in the HRS-R, π^+ and p are major background. Therefore, particle identification (PID) must be performed to remove them. PID was performed by analysis of time measurement (coincidence time analysis shown in Sec. 3.3.1) and light yields in the Cherenkov counters (Sec. 3.3.2).

3.3.1 Coincidence time method

We define t_0 as the timing when the hyperon production event occurs. Since the electrons and K^+ pass through the spectrometer ($\sim$ 23 m), the timings for the detector to measure the particles differ from t_0. These timings are denoted as $t_{e,\mathrm{det}}$ and $t_{K,\mathrm{det}}$. The velocity can be calculated by using the mass of the particles and the momentum reconstructed by BTM. Finally, the timing at the hyperon production can be calculated in each spectrometer ($t_{e,0}$, $t_{K,0}$) by using the velocity and the trajectory of the particle. If the particle assumptions are correct, the estimated timing should be the same ($t_{e,0} = t_{K,0}$). Therefore, if we define the coincidence time as follows:

$$t_{\mathrm{coin}} = t_{K,0} - t_{e,0}, \tag{3.17}$$

the coincidence events for electron and K^+ can be selected by choosing those with coincidence times near 0 ns. Figure 3.12 shows the calculation results of coincidence time when the electron and K^+ mass were assumed. The peak near 0 ns is the coincidence event between the electron and K^+. In contrast, the peak on the left ($t_{\mathrm{coin}} \sim -3$ ns) is the coincidence events between the electron and π^+ , and the peak on the right ($t_{\mathrm{coin}} \sim 8$ ns) is the coincidence events between the electron and p. There is also a periodic structure every 2 ns. This is accidental coincidence events due to the fact that the incident electron has a bunch structure every 2 ns. Since this structure also exists in the region of electron and K^+ coincidence events, we estimated the number of accidental coincidence events in the region using side-band data. Here, we selected four bunches in the region of t_{coin} = [3–5], [13–15], [15–17], [17–19] ns as side-band data. The black line in Fig. 3.12 shows the bunch structure estimated from the side-band data. The time resolution was estimated to be 0.3 ns by fitting the (e', K^+) coincidence peak. The events of $|t_{\mathrm{coin}}| < 0.7$ ns were selected to avoid π^+ contamination. The efficiency of the coincidence time cut is described in the next section.

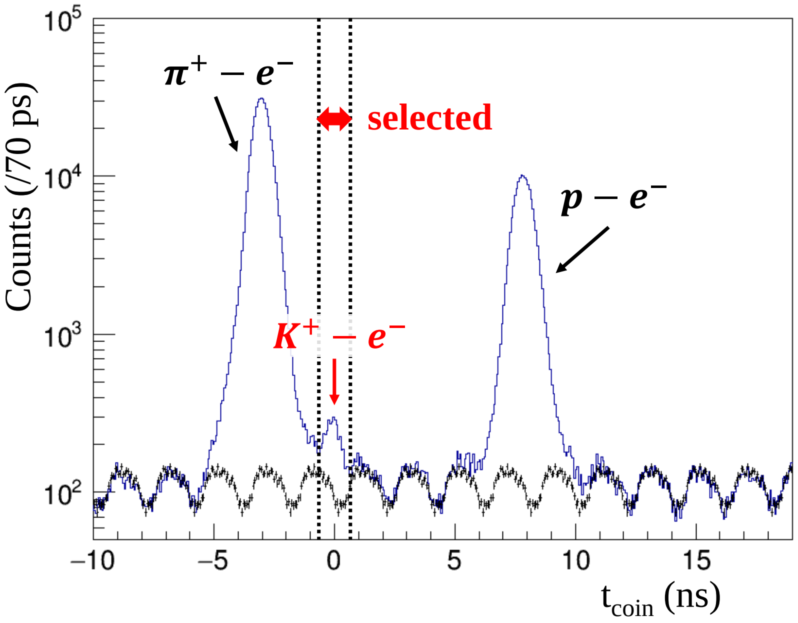

Figure 3.12 Coincidence time distribution without Cherenkov cut. The blue line shows the experimental data. The black line shows the accidental background evaluated by collecting some accidental bunches.

3.3.2 Cherenkov cut

The gas Cherenkov detector (GC) at HRS-L identified the electrons, and the aerogel detectors (AC1 and AC2) at HRS-R identified K^+. Figures 3.13 and 3.14 show the correlation between the number of photo-electrons and the coincidence time in AC1 and AC2. Events in the blue boxes are considered to be π^+ and p. K^+ events are seen in the red box around $t_{\mathrm{coin}} = 0$ ns. The following conditions were applied in the analysis to improve the purity of K^+:

$$\text{n.p.e. (AC1)} < 3.0,$$
$$1 < \text{n.p.e. (AC2)} < 23.0.$$

The K^+ efficiency with the Cherenkov cuts was obtained using events from the $p(e, e'K^+)\Lambda/\Sigma^0$ reactions. First, a missing mass distribution for (e', K^+) coincidence events was obtained without the Cherenkov cuts. The blue line in Fig. 3.15 shows the distribution. The background from (e', π^+) coincidence events exist in this distribution. Therefore, a missing mass distribution was reconstructed with (e', π^+) coincidence events to remove π^+ contamination. This distribution was scaled to π^+ contamination ratio as shown in Fig. 3.15 and was subtracted from the distribution for the (e', K^+) coincidence events. This distribution was compared to the distribution with the Cherenkov cuts. The scale with the smallest residuals of these distributions were searched for. This scale indicate the K^+ efficiency. While changing the π^+ contamination ratio, the scale where residuals were the smallest was set as the K^+ efficiency. The K^+ efficiency with the Cherenkov cuts was estimated to be 91.4 ± 6.3%.

The efficiency of coincidence time cut and π^+ contamination ratio were evaluated by fitting the coincidence time distribution. Here, the π^+ contamination ratio was defined as $N_\pi/(N_\pi + N_K)$. The fitting result with the double-Gaussian functions is shown on the left of Fig. 3.16. The accidental coincidence components have already been subtracted. The result shows that there are residual events to the right of K^+ peak. The π^+ peak may be distorted from the Gaussian function because the coincidence time was reconstructed with the assumption of K^+ mass for particles in HRS-R as shown in Sec. 3.3.1. A exponential function was added to represent this event, since the events on the right side of K^+ peak were assumed to be the tail due to π^+ events. The fitting result with the function with the exponential tail for π^+ is shown on the right of Fig. 3.16. We took the average of the cases with and without the exponential function. From these fittings, the contamination of π^+ was estimated to be 2.4 ± 1.8%. In contrast, the contamination from protons was negligibly small.

In addition, we selected the events with $|t_{\mathrm{coin}}| < 0.7$ ns to improve K^+ purity. The efficiency of the event selection was estimated to be 98.4 ± 0.5% from the fitting of Fig. 3.16. In addition, the data of the timing information was partly broken. Some bunch of events could be found where the coincidence time was shifted on the order of μs. When the number of events in a bunch is large enough, we could increase the statistics by correcting the coincidence time for proper timing. Some bunches had so few events that it was difficult to correct the coincidence time. These events were cut and taken into account as an efficiency, which was estimated to be 97.7 ± 0.2%. A total efficiency due to the coincidence-time event selections was estimated to be 96.1 ± 0.5%.

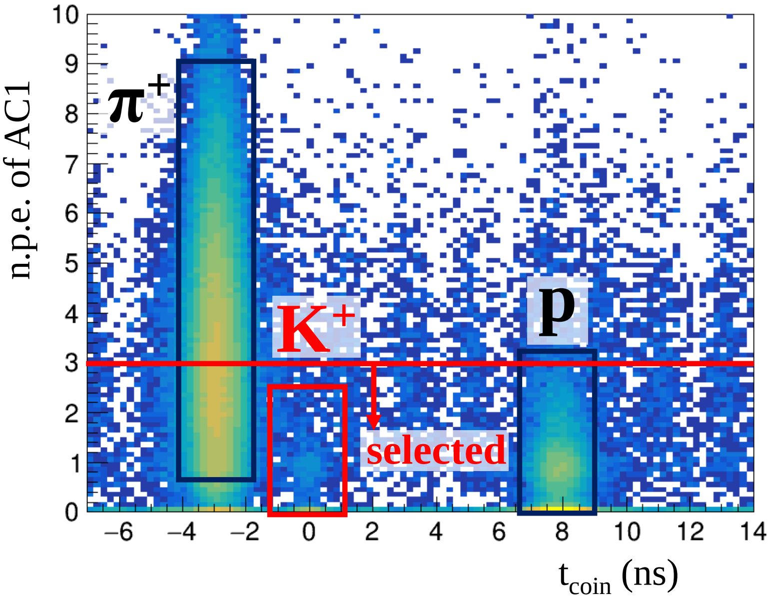

Figure 3.13 Correlation between the number of photo-electrons and the coincidence time of AC1. The typical regions of π^+, K^+ and p are shown in solid boxes.

3.4 Beam electron

The number of electrons incident on the target was counted for the cross-section analysis as shown in the following Section 3.4.1. The electron beam was periodically deflected in x and y directions (raster) to make the beam spot large enough to avoid damage on the target cell due to the heat (we called it raster beam). The beam spot size with the raster 2×2 mm^2 although the original beam size at Hall A is about rms = 100 μm which is negligibly small for beam optics analysis of spectrometers. The beam size due to the raster needed to be corrected event by event in the analysis as shown in Sec. 3.4.2.

3.4.1 Beam charge

The beam charge on the target was measured by BCM (Sec. 2.2.2). The amount of charge irradiated to each target was obtained by integrating the BCM data. The results are summarized in Tab. 3.1. The error was mainly due to the accuracy of the BCM.

3.4.2 Raster correction

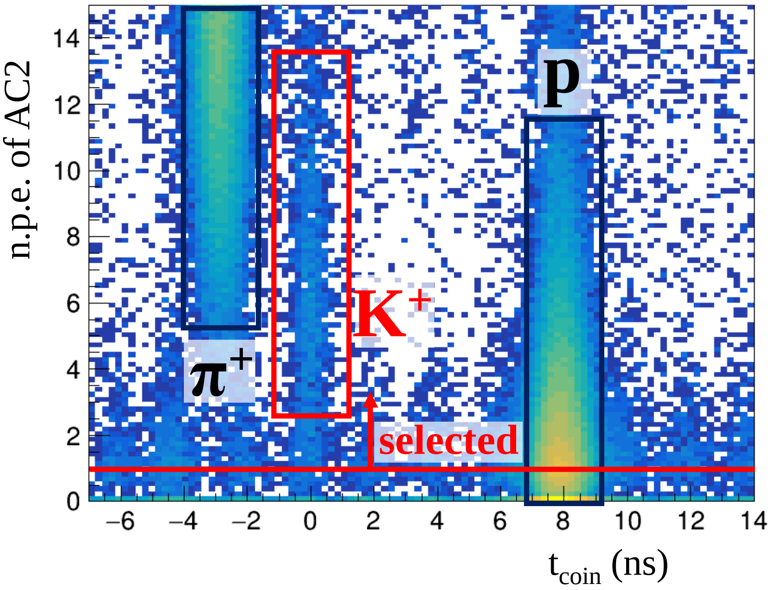

Figure 3.14 Correlation between the number of photo-electrons and the coincidence time of AC2. The typical regions of π^+, K^+, and p are shown in solid circles.

Table 3.1 The total beam charge irradiated to each target obtained by accumulating the BCM information on each run.

Target	Charge (C)
H_2	4.71±0.05
T_2	16.95±0.17

The incident electrons were bent by the magnetic field and irradiated to the target with a distribution of 2×2 mm^2 in the xy-plane to avoid heat concentration from the electron beam. Here, x and y directions are dispersive and non-dispersive directions, respectively. The distribution is shown in Fig. 3.17. Experimental analysis was performed under the assumption that events were produced at $(x, y) = (0, 0)$ mm. The vertex position was corrected with the y position as follows,

$$z'_T = z_T + \frac{y}{y'} \tag{3.18}$$

Here, z and z' are the vertex position before and after the correction and y' is the angle (p_y/p_z) of the particle at the target.

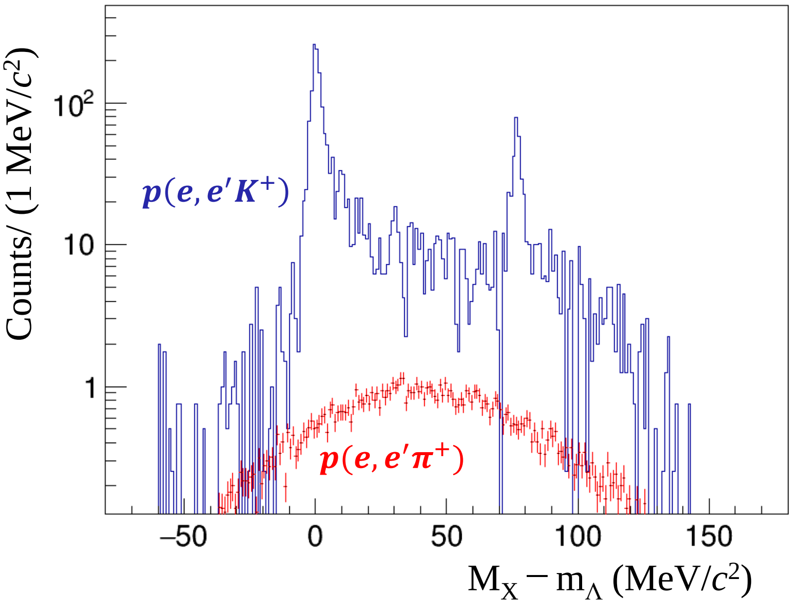

Figure 3.15 Missing-mass distribution of $p(e,e'K^+)$ reaction without Cherenkov cut and that of $p(e,e'\pi^+)$ reaction.

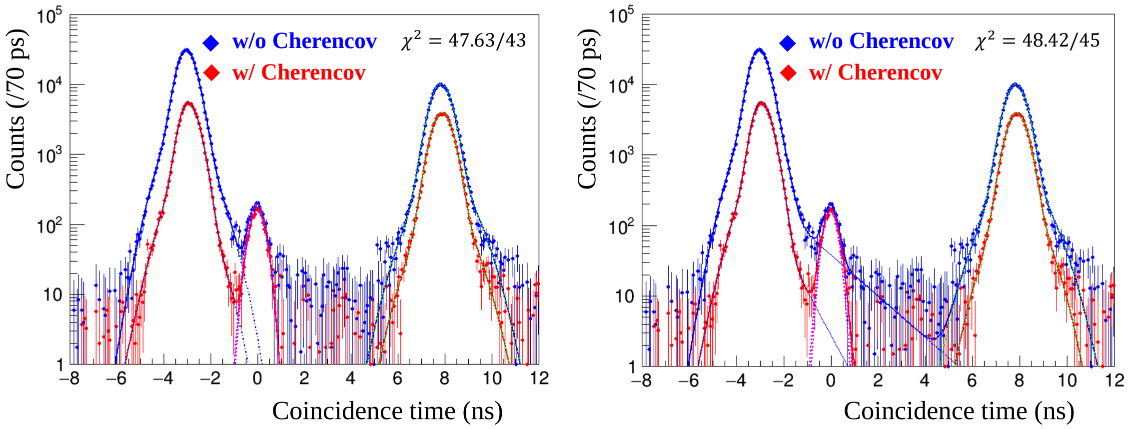

Figure 3.16 Coincidence time before and after Cherenkov cut. The left shows the fitting result assuming the Gaussian function as the π^+ peak. The right shows the fitting result assuming the Gaussian function and exponential tail as the π^+ peak.

3.5 Others

In this section, we discuss the efficiency evaluation, which has not been discussed above. In Sec. 3.5.1, tracking efficiency of VDCs will be discussed. In Sec. 3.5.2, the treatment of multiplicity data is described. A cut was applied to data with multiplicity of 2 or more because the multiplicity was small in this experiment. We will discuss the efficiency of the

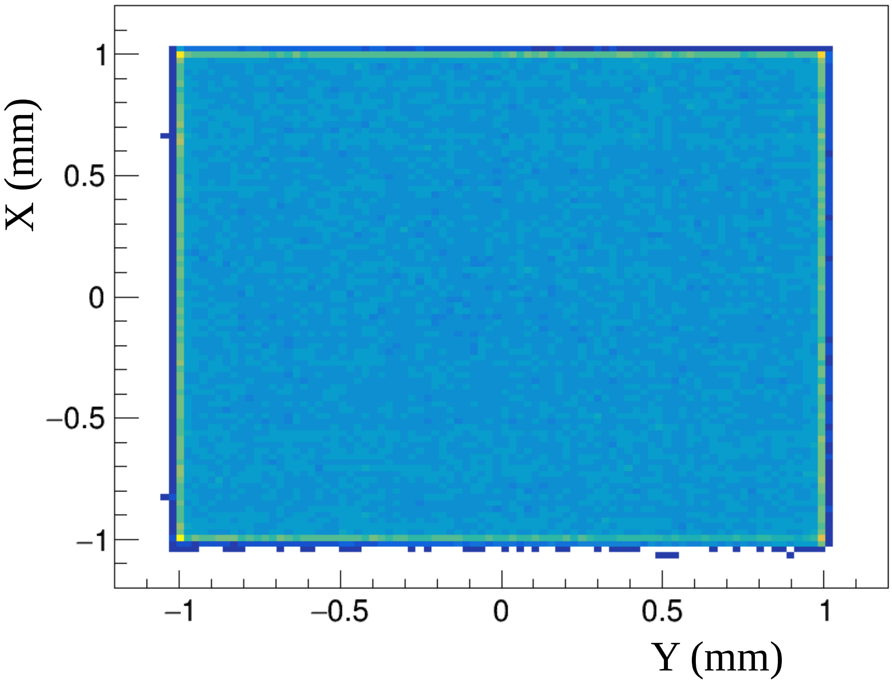

Figure 3.17 Beam image of x vs. y at the target, which was reconstructed by using the BPM information.

multiplicity cut. In Sec. 3.5.3, we will discuss DAQ efficiency.

3.5.1 Tracking efficiency

The VDCs were used for tracking, as described in Sec. 2.5.1. Tracking efficiency was estimated from the experimental data. First, as shown in the left panel of Fig 3.18, a wire efficiency was determined based on whether the center wire had a hit when neighbored wires at both sides of the wire had hits. The wire efficiency of a typical run is shown in the right panel of Fig. 3.18. The efficiency near the center is almost 1, and the efficiency decreases toward the edge. The hit distribution of the particles and the number of wires per hit were also estimated from the experimental data. The hit distribution of the particles is shown in Fig. 3.19.

The efficiency per layer (Plane efficiency) of each VDC was calculated using a MC simulation by using the wire efficiency. Here, we assumed that the wire efficiencies were independent with each other. The wire hit information is given to the wire in MC simulation according to the particle distribution as shown in Fig. 3.20. Then, the wire is set to be inefficient with a certain probability based on the wire efficiency. If the cluster is broken by this process, the efficiency decreases. By repeating this procedure, a plane efficiency of each VDC layer was obtained. The tracking efficiency per spectrometer was obtained as the product of the plane efficiency of each VDC layer. The efficiency for a typical run is summarized in Tab. 3.2. The tracking efficiency for each run was calculated and the result is shown in Fig. 3.21. The average result was 98.1% with an error of less than 0.1%.

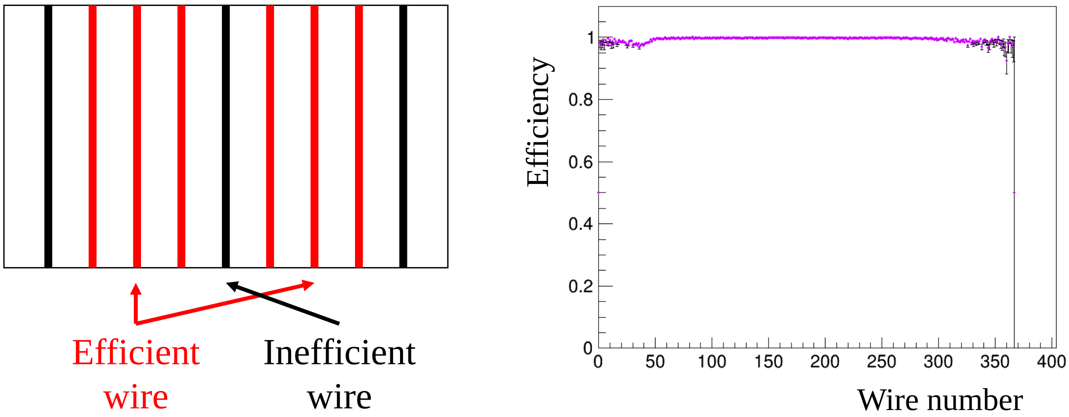

Figure 3.18 The estimation of the wire efficiency. (Left) Example of a wire hit pattern. (Right) Example of the wire efficiency of a layer.

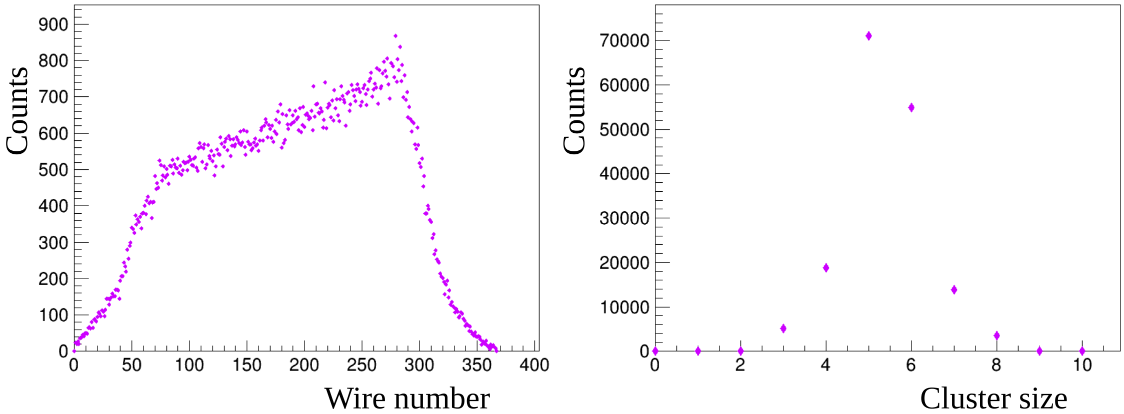

Figure 3.19 VDC hit information estimated from experimental data. (Left) Wire hit position in a layer. (Right) Cluster size of one particle.

3.5.2 Multiplicity

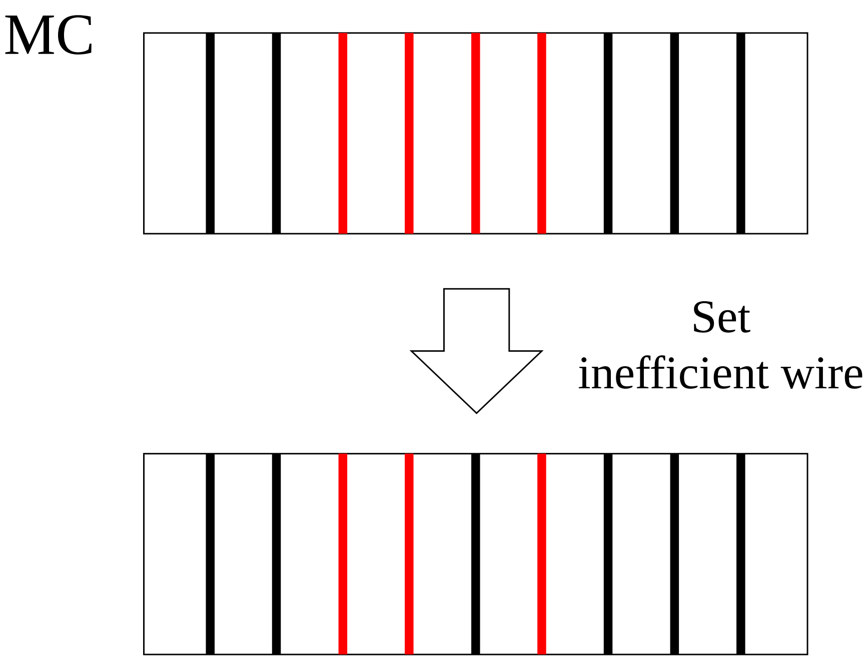

Figure 3.20 Strategy of MC simulation for plane efficiency estimation.

Table 3.2 VDC plane efficiency and tracking efficiency in a typical run.

Layer	LHRS Efficiency (%)	RHRS Efficiency (%)
VDC1 u	99.72	99.78
VDC1 v	99.65	99.64
VDC2 u	99.80	99.78
VDC2 v	99.73	99.80
Tracking efficiency	$98.90^{+0.12}_{-0.18}$	$99.18^{+0.09}_{-0.19}$

In this experiment, multiple particles may come into each spectrometer for one trigger. Since we are using multi-hit TDC, these events were recorded. The multiplicities per event of the left and right spectrometers are denoted as M_L and M_R, respectively. The multiplicity was low in this experiment, so data analysis was performed only in the case of $M_L = 1$ and $M_R = 1$. The loss of signals which is due to the cut of multiple hits needed to be taken into account for the cross-section analysis. The ratio of remaining events to that of the total number of signals after the multiple-hit cuts is defined as $\epsilon_{\mathrm{multi}}$.

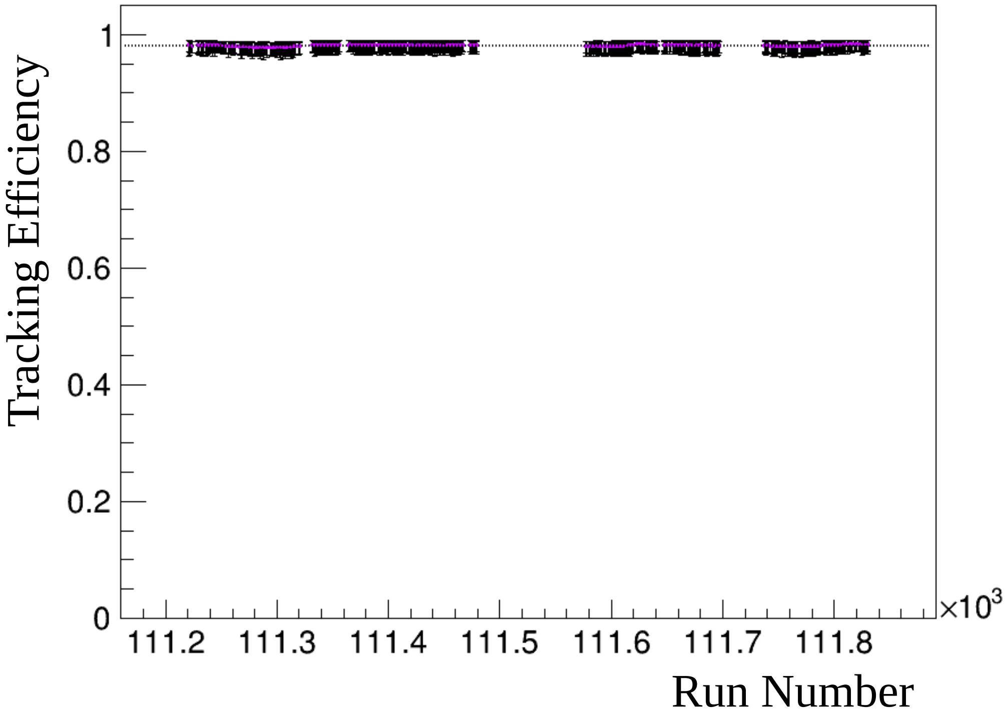

Figure 3.21 Run dependence of tracking efficiency.

First of all, we consider $(M_L, M_R) = (2,1), (1,2)$ as the excluded event. For example, in the case of $(M_L, M_R) = (2,1)$, two tracks (p_{L1}, p_{L2}) were recorded in HRS-L and one track (p_{R1}) in HRS-R. The possible events at this time are $p_{L1} \times p_{R1}$ and $p_{L2} \times p_{R1}$.

First, the case $(M_L, M_R) = (1,2)$ is considered. The timing information is shown in the upper part of Fig. 3.22. The coincidence time is calculated by considering the time difference between the trigger timing and K^+. Since the trigger timing is determined by the electrons, the coincidence time can be correctly calculated in both cases. The left panel of Fig. 3.23 shows the coincidence time when the event $(M_L, M_R) = (1,2)$ is selected. It shows the sum of the distributions of $p_{L1} \times p_{R1}$ and $p_{L1} \times p_{R2}$. The distribution of coincidence time is different from $(M_L, M_R) = (1,1)$, and no clear peak structure of K^+ could be observed in this condition. This may be because multiple events are mostly secondary particles that have been created by collisions with detectors or magnets, and the physical quantities such as momentum have changed. Therefore, the region of K^+ was fitted with an exponential function representing BG and a Gaussian function representing the K^+ events. The upper limit of the integral of the signal was estimated to be 0.86% and set as a systematic error.

Next, the case $(M_L, M_R) = (2,1)$ is considered. The timing information in this case is shown in the lower part of Fig. 3.22. In the first event $p_{L1} \times p_{R1}$, the coincidence time was calculated correctly, but in the second event $p_{L1} \times p_{R2}$, the coincidence time could not be calculated correctly because the time difference between the electron and K^+ could not be used. However, the probability that a true event is included is the same for both $p_{L1} \times p_{R1}$ and $p_{L1} \times p_{R2}$. Therefore, the upper limit was determined in $p_{L1} \times p_{R1}$, and the upper limit was doubled. The calculation was performed in the same manner as in $(M_R, M_R) = (1, 2)$ and the systematic error was estimated to be 0.42%.

The number of events with multiplicity higher than the above is several times less, so the difference in efficiency due to cutting these events is negligible. By taking the sum of both $(M_L, M_R) = (1, 2)$ and $(M_L, M_R) = (2, 1)$, the error due to the multiplicity was estimated to be 1.3%.

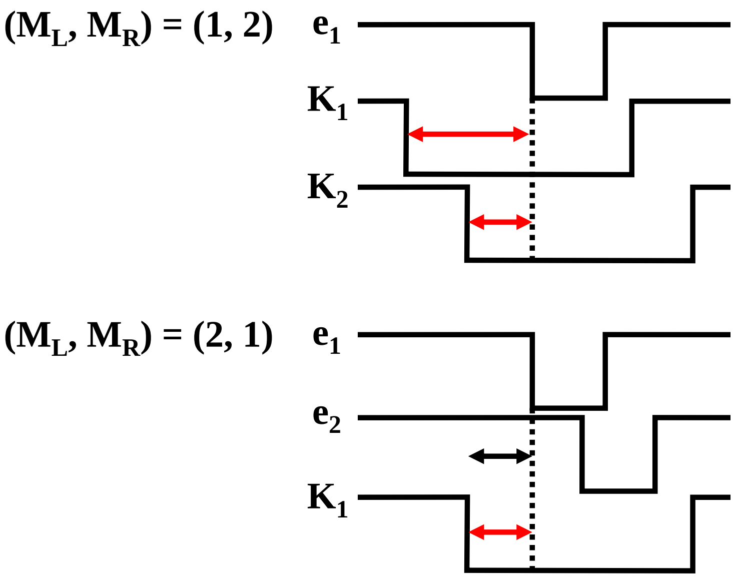

Figure 3.22 TDC timing information when a multiple hit event occurs.

3.5.3 DAQ efficiency

The run dependence of the DAQ dead time is shown in Fig. 3.24. The DAQ dead time differs between the initial runs and the subsequent runs. In the data acquisition, not only T5 (coincidence trigger) but also T1 and T4 (single trigger) were acquired to check the status of the single arm. In the beginning, the DAQ efficiency was poor because a lot of data were acquired by a single trigger. In the meantime, the ratio of the single trigger data acquisition

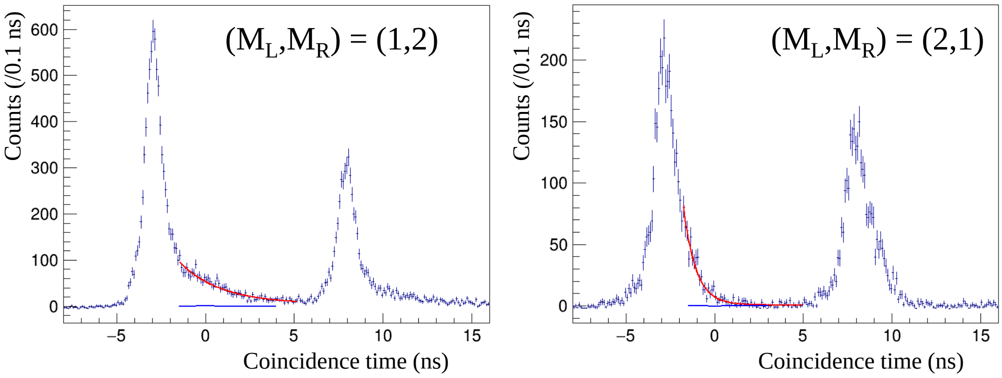

Figure 3.23 Coincidence time distribution in the multiplicity event. Left shows the distribution for $(M_L, M_R) = (1, 2)$ and right shows for $(M_L, M_R) = (2, 1)$, respectively.

was reduced by changing the pre-scale factor, so the DAQ efficiency improved. By averaging the DAQ dead time for each run with the weight of the number of events, the efficiency due to DAQ dead time was estimated to be 96.5%. The error was less than 0.1%.

In addition, the efficiency of S0 and S2, which are the trigger counters, was considered. This was estimated using experimental data and was found to be 98.1 ± 0.1% [44]. Combining the above, the efficiency associated with DAQ was estimated to be 94.6 ± 0.1%.

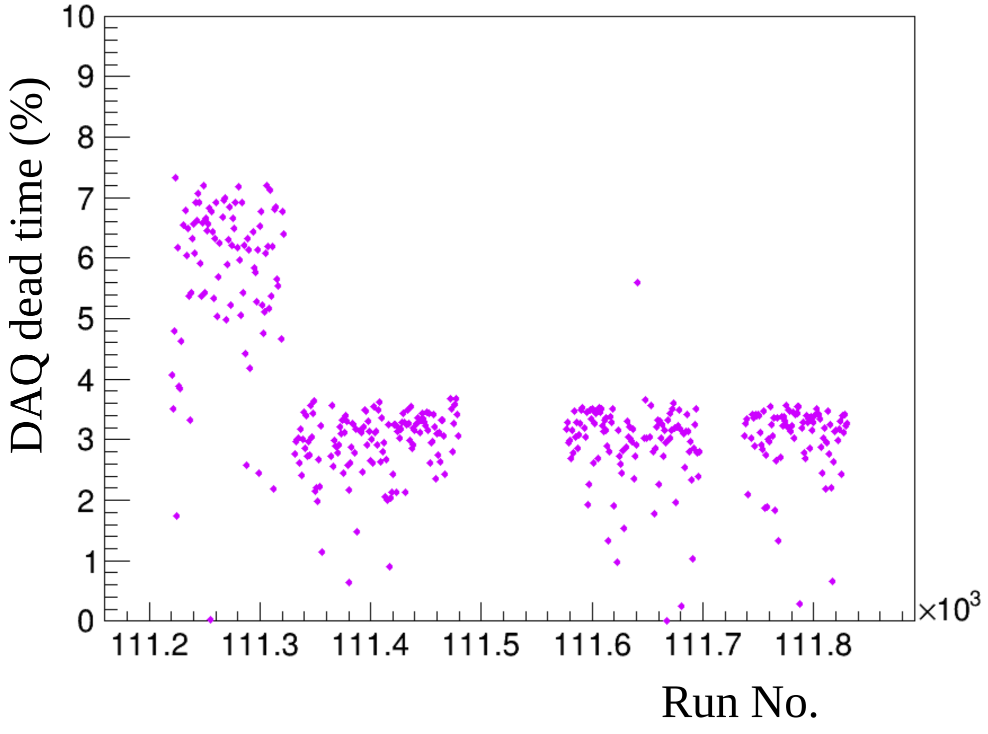

Figure 3.24 Run dependence of DAQ dead time.

Chapter 4

Monte Carlo Simulation

In this chapter, the Monte Carlo (MC) simulation used for data analysis is described. Some physical quantities, such as acceptances and resolution, could not be obtained from only the experimental data and they were evaluated by the MC simulation. The MC simulation was built based on Geant4. In this chapter, the outline of the Geant4 simulator is described first. Then, the event generator, which was used as inputs in the MC simulation, is explained. Next, a setup model of the MC simulation and its validity test by comparing with the experimental data are shown. Finally, various quantities evaluated by the optimized MC simulation are given.

4.1 Introduction

The MC simulation based on Geant4 was built to evaluate various quantities such as spectrometer acceptance, K^+ decay factor, and so on. There is an existing simulation SIMC [57]. SIMC uses the backward transfer matrix (BTM) which was obtained by using an optics calculation software. Therefore, the optics calculation needs to be redone to generate a new matrix as an input of SIMC when one studies different beam optics. SIMC runs much quicker than Geant4 because it calculates particle distribution based on the transfer matrix. However, we wanted to study the optics more detail by changing the magnetic field to quantitatively evaluate systematic errors on the cross-section results.

A new simulator was constructed by the Geant4 [58–60] to enable more detailed simulations for this analysis. This was built in C++ and provides a toolkit for Monte Carlo simulations. The Geant4 can change the magnetic field in the simulation, so we can easily modify the spectrometer optics. Since the optics of both HRS-L and HRS-R are identical, a simulator reproducing HRS-L (HRS Geant4) was constructed, and HRS-R was used as a reversal of the magnetic polarity of HRS-L.

The procedure for obtaining the missing mass distribution by the HRS Geant4 is shown in Fig. 4.1. First, the kinematics parameters $(p, x_T, x'_T, y_T, y'_T)$ of scattered electrons and K^+ are obtained using the event generator described in Sec. 4.2. Using this information as input, the particle position and angular distribution on the VDC (x, y, x', y') can be obtained by simulating the particle trajectory using the HRS Geant4. The BTM can be obtained using the Eqs. (3.2), (3.3), (3.4), and (3.5). Furthermore, by randomly varying these quantities with the position and angle resolutions of VDC, the VDC distribution that represents the experiment can be produced. The physical quantities at the target (x'_T, y'_T, p_T, z), which include the effects of resolution and bremsstrahlung, can be reconstructed using the BTM. The missing mass distribution can be calculated by applying this calculation to the scattered electron and K^+. Moreover, the resolution of each physical quantity can be estimated by comparing the quantity with the true value. The details of the resolution will be described in Sec. 5.2.

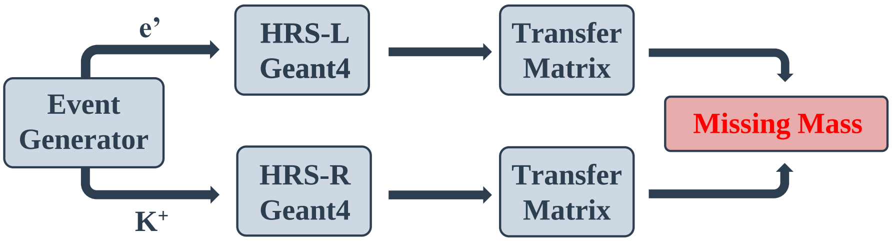

Figure 4.1 Strategy for missing mass reconstruction with Geant4.

4.2 Event generator

The MC simulation was used for the particle transportation, and it needed the particles' information of momentum vectors at the production point. We made a code to calculate the momentum vectors of e' and K^+ at the production point assuming the $(e, e'K^+)$ reaction. The schematic view of the event generation is shown in Fig. 4.2. First, the energy of the incident electron is determined, from which a virtual photon γ^* is emitted (Sec. 4.2.1–4.2.2). It then reacts with the target to produce K^+ and hyperon (Sec. 4.2.5). The calculation method is different for the hydrogen target and the tritium target. In the following sections, details of the generator are given.

4.2.1 Beam electron

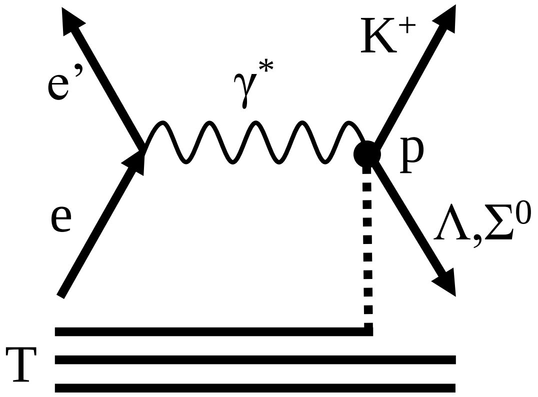

Figure 4.2 The schematic view of the ^{3}H$(e, e'K^+)X$ reaction.

The energy of the incident electrons was determined based on the distribution of the experimental data. The central momentum of the incident electrons was 4.31 GeV/c, and the energy resolution was $\Delta E/E \sim 1.0 \times 10^{-4}$ (FWHM). In addition, the energy was lost in the target cell. The energy loss was taken into account as shown in Sec. 4.4.3.

4.2.2 Scattering electron and virtual photon

The generator uses one-photon approximation, which assumes that the incident electron only emits one virtual photon. The number of virtual photons (N_{γ^*}) is expressed as

$$N_{\gamma^*} = N_e \iint \Gamma d\Omega_{e'} dE_{e'}. \tag{4.1}$$

Here, N_e is the number of the beam electrons. Γ is expressed as

$$\Gamma = \frac{\alpha}{2\pi^2 Q^2} \frac{E_\gamma}{1-\epsilon} \frac{E_{e'}}{E_e} \tag{4.2}$$

Each parameter is explained in Sec. 2.1.1. The four momentum of the scattered electron $p_{e'}$ are determined by using Eq. (4.2). The momentum of the virtual photon can be calculated as follows

$$p_{\gamma*} = p_e - p_{e'}. \tag{4.3}$$

4.2.3 Radiation effect

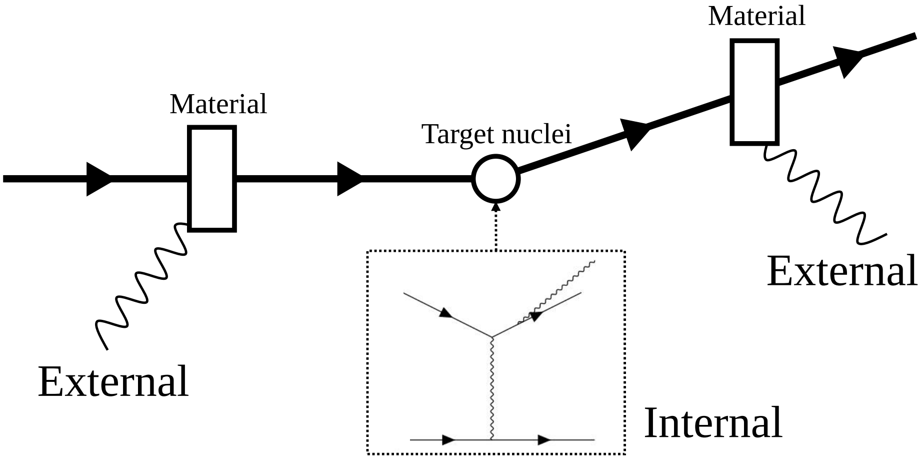

Figure 4.3 Schematic view of internal and external radiation.

In electron scattering experiments, the radiation effect due to the small mass of the electron cannot be ignored. The missing mass distribution has a large amount of radiative tails in the high mass side as shown in Fig. 3.6. These radiative tails can be categorized into two types: internal and external radiation. Internal radiation is caused by the scattering of electrons by the electric field of the target nucleus. In contrast, external radiation is caused by scattering of electrons by materials other than the target nucleus. The term "radiation" is usually used to refer to the external radiation. Since external radiation is included in the physics process of Geant4, the only radiation that needs to be included in the generator is the internal radiation.

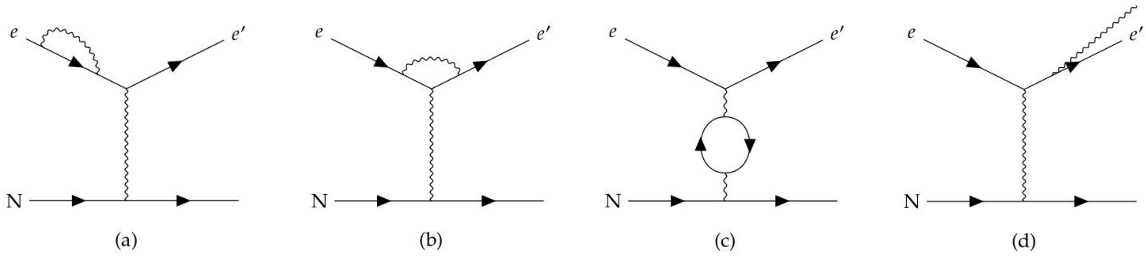

Figure 4.4 Feynman diagrams contributed to the internal radiation. Panels a, b, and c represent virtual internal radiation. Panel d represents the real internal radiation.

The internal radiation was calculated in the Ref. [61], and this calculation was incorporated in the generator. The correction of the cross-section by internal radiation can be expressed as follows:

$$\left(\frac{d\sigma}{d\Omega_{e'}}\right)_{\exp} = \left(\frac{d\sigma}{d\Omega_{e'}}\right)_{BORN} \frac{e^{\delta_{vertex}+\delta_R}}{(1-\delta_{vac}/2)^2}. \tag{4.4}$$

Here, δ_{vertex}, δ_{vac} and δ_R represent the vertex correction, the vacuum polarization correction and the real radiative correction, respectively. δ_{vertex} and δ_{vac} come from the Feynman diagrams in Fig. 4.4(a), (b), and (c), respectively. Since they denote the virtual internal radiation, they do not contribute to the experimental observables. δ_R comes from the Feynman diagram shown in Fig. 4.4(d), which contributes to the experiment as internal radiation. The discussion will therefore be limited to the e^{δ_R} part. δ_R is expressed as follows under $Q^2 \gg m_e^2$.

$$\delta_R = \frac{\alpha_{em}}{\pi}\left\{\ln\left(\frac{\Delta E_e \Delta E_{e'}}{E_e E_{e'}}\right)\left[\ln\left(\frac{Q^2}{m_e^2}\right)-1\right] - \frac{1}{2}\ln^2\left(\frac{\tilde{E}_e}{\tilde{E}_{e'}}\right) + \frac{1}{2}\ln^2\left(\frac{Q^2}{m_e^2}\right) - \frac{\pi^2}{3} + \mathrm{Sp}\left(\cos^2\frac{\tilde{\theta}_e}{2}\right)\right\}. \tag{4.5}$$

Here, the tilde symbol indicates the parameters in the center-of-mass frame, and ΔE_e and $\Delta E_{e'}$ are the energy loss of the incident and scattered electrons due to internal radiation, respectively. Sp denotes Spence's function, which is defined as follows:

$$\mathrm{Sp}(x) = -\int_0^x dt \frac{\ln(1-t)}{t}. \tag{4.6}$$

It is the first term in Eq. (4.5) that contains the energy loss term, and the other terms do not contribute to energy loss. Therefore, the contribution of internal radiation can be described as follows:

$$e^{\delta_R} \sim \left(\frac{\Delta E_e \Delta E_{e'}}{E_e E_{e'}}\right)^a \tag{4.7}$$

$$= \left(\frac{\Delta E_e}{E_e}\right)^a \left(\frac{\Delta E_{e'}}{E_{e'}}\right)^a, \tag{4.8}$$

where

$$a = \frac{\alpha_{em}}{\pi}\left[\ln\left(\frac{Q^2}{m_e^2}\right)\right]. \tag{4.9}$$

When an electron with energy E loses energy ΔE, the distribution is expressed as follows:

$$I_{\mathrm{int}}(E, \Delta E, a) = \frac{a}{\Delta E}\left(\frac{\Delta E}{E}\right)^a. \tag{4.10}$$

Here, $a/\Delta E$ is the normalization factor. This equation is the same function as that for external radiation, where the thickness of material t is replaced by a. In the generator, the energy loss was calculated for both the incident and scattered electrons. The result is shown in Fig. 4.5. The external radiation alone does not reproduce the experimental data, but the inclusion of internal radiation reproduces the data well.

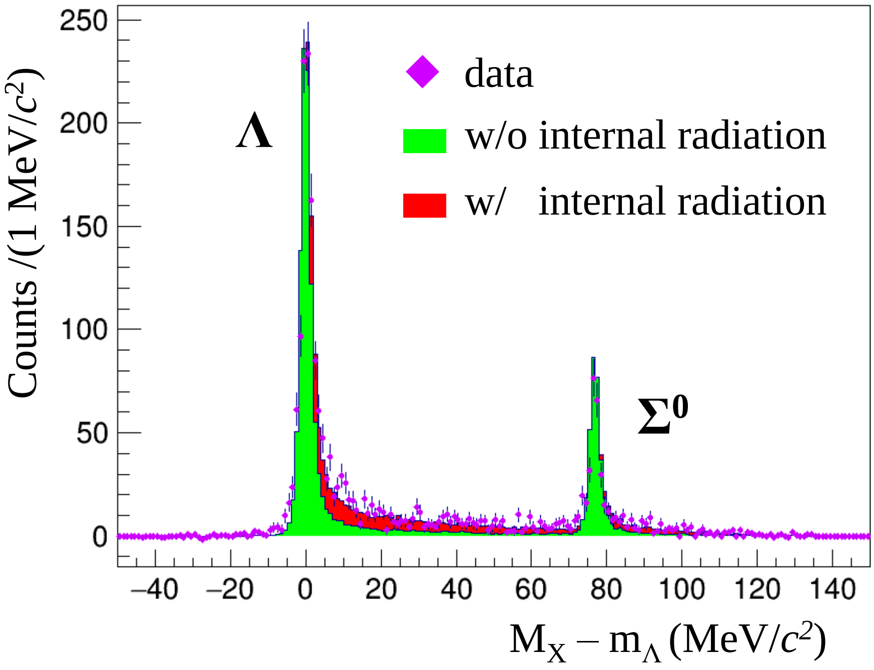

Figure 4.5 The effect of the internal radiation. The missing mass spectrum of the $p(e, e'K^+)\Lambda/\Sigma^0$ reactions with and without the internal radiation is shown using a green and red histogram, respectively.

4.2.4 Fermi motion and off-shell effect

The process of a virtual photon reacting with a proton in a target nucleus is considered. In this experiment, a hydrogen target and a tritium target were used. In the case of the hydrogen target, the proton is assumed to be at rest. In contrast, in the case of the tritium target, the protons are bound in the nucleus and have Fermi momentum.

Fermi motion was incorporated using the spectral function $S(E, k)$. The spectral function is the probability of finding a nucleon with momentum k in a state with removal energy E. The removal energy E is expressed as follows:

$$E = |E_A| - |E_{A-1}| + E^*_{A-1}, \tag{4.11}$$

where E_A is the binding energy of the target nucleus, E_{A-1} is the binding energy of the residual nucleus, and E^*_{A-1} is the excitation energy of the residual nucleus. The momentum of the proton $\vec{k_p}$ can be obtained by using the spectral function. In the case of a tritium target, the residual nucleus has two neutrons. By denoting their momentum as $\vec{k_{n1}}, \vec{k_{n2}}$, the following equation is obtained:

$$E^*_{A-1} = \frac{\vec{k}^2_{rel}}{M} = \frac{(\vec{k_{n1}} - \vec{k_{n2}})^2}{4M} \tag{4.12}$$

Here, $\vec{k}_{rel}$ is the relative momentum of the two neutrons. The angle of $\vec{k}_{rel}$ was uniformly distributed. Based on Eq. (4.12) and conservation of momentum, the magnitude of the momentum of the two neutrons can be determined as follows:

$$|\vec{k_{n1}}| = \sqrt{\vec{k}^2_{rel} + \frac{\vec{k}^2_p}{4} + |\vec{k}_{rel}||\vec{k}_p| \cos\theta}, \tag{4.13}$$

$$|\vec{k_{n2}}| = \sqrt{\vec{k}^2_{rel} + \frac{\vec{k}^2_p}{4} - |\vec{k}_{rel}||\vec{k}_p| \cos\theta}. \tag{4.14}$$

Theoretical calculations by Ciofi were used as the spectral function. For the tritium target, the result published in 1980 [62] is shown in Fig. 4.6. However, since the calculations used are outdated and there is a lack of experimental information to confirm this, the spectral function result [63, 64] for ^{3}He is used in this work. Assuming isospin symmetry, the theoretical calculations for neutrons and protons in ^{3}He were used to calculate the momentum of protons and neutrons in ^{3}H. The uncertainty of assumption has been reported by one of the JLab tritium experiments [55] and was estimated to be less than 3% based on the Fermi momentum calculation by Wiringa [56].

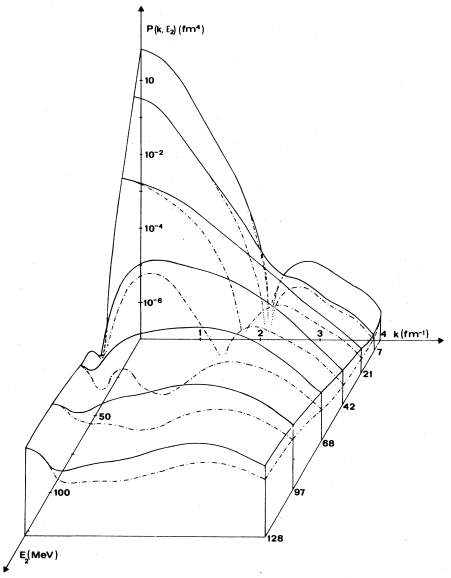

Figure 4.6 Spectral function of the process ^{3}H(e, e′p)2n. This figure is taken from Ref. [62].

Nucleons in nuclei are off-mass shells because they have Fermi momentum. However, as will be discussed in a later section, the $\gamma + N \rightarrow K^+ + Y$ reaction was calculated using the cross-section results from the CLAS experiment [41]. The target of the CLAS experiment is hydrogen, so the proton is an on-mass shell. The on-mass-shell approximation [65] was applied to solve this issue. The proton mass (M_{p*}) assumed to be off-mass shell as follows:

$$M_{p*}^2 = \left(M_T - \sqrt{M_n^2 + |\vec{k_{n1}}|^2} - \sqrt{M_n^2 + |\vec{k_{n2}}|^2} \right)^2 - |\vec{p_F}|^2 \tag{4.15}$$

where M_T and M_n are the masses of the tritium nucleus and neutron, respectively, and $\vec{p_F}$ is the momentum of the proton.

4.2.5 Hyperon production

The reaction between the virtual photon and the target nucleus is considered here. In the case of a tritium target, the reaction $\gamma^* +^3 \mathrm{H} \to K^+ + Y$ should be considered. However, the impulse approximation, in which γ^* reacts with a single nucleon, can be used due to the high energy of the virtual photon. Therefore, the reaction $\gamma^* + p \to K^+ + Y$ is considered. Since experimental data and theoretical calculations on hyperon production with virtual photons are scarce, the reaction is assumed to be with real photons. There are three types of hyperon production reactions to be considered:

$$\begin{aligned} &\gamma + p \to K^+ + \Lambda, \\ &\gamma + p \to K^+ + \Sigma^0, \\ &\gamma + n \to K^+ + \Sigma^-. \end{aligned} \tag{4.16}$$

The data from the CLAS experiment [41] were used to take into account the energy and angular dependence of these reaction cross-sections. The CLAS experiment was performed at Hall B in JLab and measured the hyperon-production cross section on a proton target using real photons over wide energy and angular ranges. The experimental results are shown in Fig. 4.7 and 4.8. Since there were no data available for the neutron target, the energy and angle dependence of $\gamma + p \to K^+ + \Lambda$ reaction were applied assuming isospin symmetry. These results were used to obtain the four momenta of K^+ and the hyperons.

4.3 Geant4 setup

The momentum vectors of the scattered electrons and K^+ created by the generator are used as input for the HRS Geant4. The construction of the HRS Geant4 is described below.

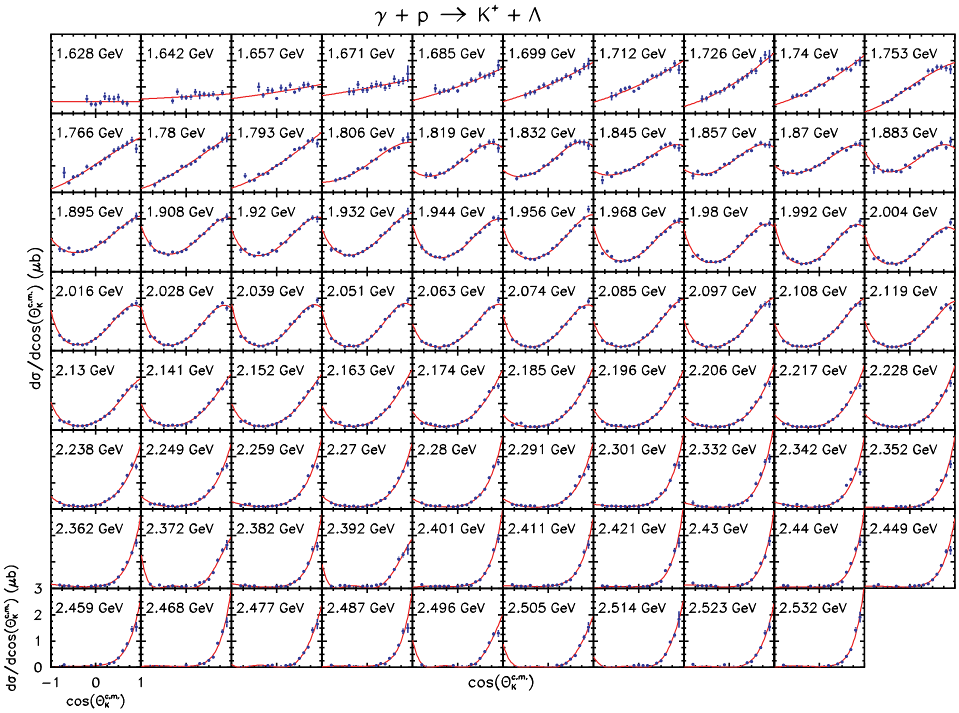

Figure 4.7 Differential cross sections for $\gamma + p \rightarrow K^+ + \Lambda$ [41]. The number in each panel shows $W(= \sqrt{s})$.

4.3.1 Geometry

The geometrical information of the HRS spectrometer was taken from Ref. [66]. The visualized result of the HRS Geant4 is shown in Fig. 4.9. Since the Q1 and D magnets considerably contribute to acceptance, the design was reproduced by 3D-CAD and incorporated into the simulator. In contrast, Q2 and Q3, which do not contribute significantly to the acceptance, were incorporated in a simple cylindrical shape. The target cell is also incorporated in its actual shape because it is important for the calculation of the energy loss. As for detectors, the position and size of the VDC and S2 were also incorporated. The target chamber, vacuum films, air, etc. were also incorporated to calculate the energy loss in the spectrometer path correctly. The material list is summarized in Tab. 4.1.

4.3.2 Magnetic field

The magnetic field is one of the most important parameters that determine the yield and resolution of an experiment. For the dipole magnet, the magnetic field was calculated using the TOSCA code. TOSCA is a software which can calculate the 3D magnetic field maps using

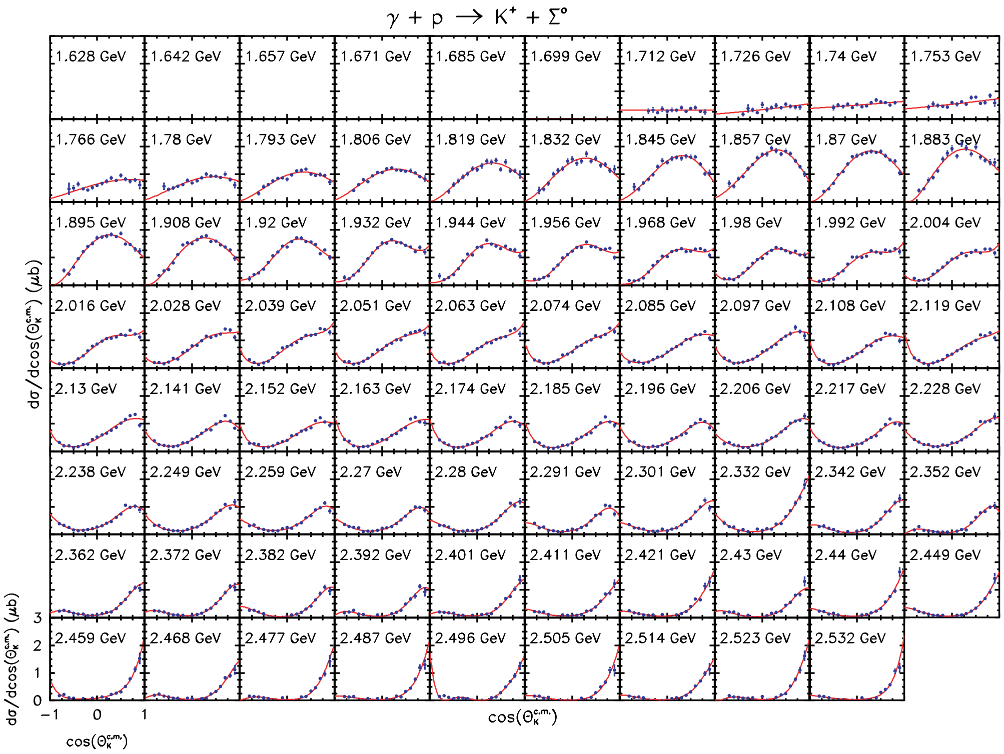

Figure 4.8 Differential cross sections for $\gamma + p \to K^+ + \Sigma^0$ [41]. The number in each panel shows $W (= \sqrt{s})$.

the finite element method. In contrast, for the quadrupole magnets (Q1, Q2, Q3), an empirical formula, the Kato formula [67], was used.

$$B_x = gy\left[H(s) - \frac{y^2 + 3x^2}{12G^2}\frac{d^2H(s)}{ds^2}\right] \tag{4.17}$$

$$B_y = gx\left[H(s) - \frac{x^2 + 3y^2}{12G^2}\frac{d^2H(s)}{ds^2}\right] \tag{4.18}$$

$$B_z = g\frac{xy}{G}\frac{dH(s)}{ds} \tag{4.19}$$

$$s = \frac{z}{G} \tag{4.20}$$

$$H(s) = (1 + \exp(C_0 + C_1 s + C_2 s^2 + C_3 s^3))^{-1} \tag{4.21}$$

$$C_0 = -0.9842, C_1 = 6.3375, C_2 = -3.5134, C_3 = 0.9895 \tag{4.22}$$

The z direction is the depth direction of a quadrupole magnet. G is the bore radius and g is the magnetic field gradient.

As described above, an empirical formula was used for the magnetic field, which does not completely reproduce the actual magnetic field. Therefore, the magnetic field was optimized to reproduce the experimental values such as VDC hit distributions. The optimization process

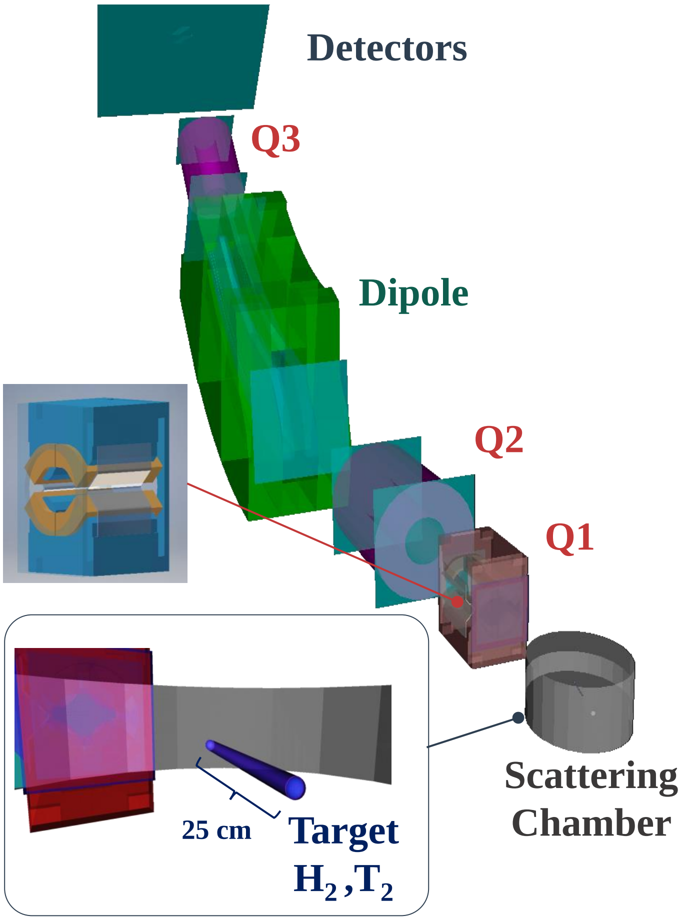

Figure 4.9 Visualization of the HRS Geant4 simulator.

is described below. Since the optics are equal for both HRS-L and HRS-R arms, the parameters of the magnetic field were varied while keeping the ratio of each magnetic field strength as follows:

$$B_{D_L} : B_{Q1_L} : B_{Q2_L} : B_{Q3_L} = B_{D_R} : B_{Q1_R} : B_{Q2_R} : B_{Q3_R}, \tag{4.23}$$

where B_D is the magnetic field of the dipole magnet, B_Q is that of the quadrupole magnet, L stands for HRS-L, and R stands for HRS-R. Furthermore, the ratio of B_{Q2} to B_{Q3} did not change since the same magnets were used for Q2 and Q3. Therefore, the parameters to be optimized were B_D, B_{Q1}, and B_{Q2}. The B_D was adjusted so that the central ray passed through the central orbit, and the momentum and mass distributions were consistent with the experimental data. The B_{Q1} and B_{Q2} were determined so that the angle distribution at VDC and target would be consistent between the experimental data and the simulation. The details of the optimization are shown in Appendix B. The residuals of the distributions from the experimental data were

Table 4.1 Material list of the particle trajectory in HRS. The total amount of thickness is shown in two different ways because S2 does not affect to the K^+ absorption.

Section	Element	Density (g/cm^3)	Length (cm)	Thickness (g/cm^2)
Gas Target	T_2	3.16×10^{-3}	25.0	0.079
Target Cell	Al7075	2.81	0.04/sin(13.2)	0.492
Scattering Chamber	Al7075	2.81	0.0279	0.078
Vacuum Entrance	Ti	4.54	0.0127	0.058
Vacuum Exit	Ti	4.54	0.0127	0.058
Air	Air	1.29×10^{-3}	139+50	0.248
VDC	Al	2.7	0.0069	0.037
S0	CH2	1.03	1.0	1.03
S2	CH2	1.03	5.08	5.23
AC1		0.10	9.0	0.90
AC2		0.20	5.0	1.00
Total				10.22
Total(w/o S2)				4.99

calculated by changing the B_{Q1} and B_{Q2}. The magnetic field setting where the residual was the minimum value was adopted as the best setting. The results are shown in Fig. 4.10. The axis shows the ratio with respect to the best setting. The experimental settings are shown as black dots. There is a difference of up to 3% in the magnetic field between the experimental setting and the best setting. The difference can be attributed to the accuracy of the HRS Geant4 setup, such as geometry and magnetic field. Therefore, the region within the red line in Fig. 4.10, which includes the experimental settings, was adopted as B_{Q1} and B_{Q2}. The difference in this line was assumed to be a systematic error.

4.3.3 Missing mass

The missing mass distribution calculated by the HRS Geant4 for a proton target is shown in Fig. 4.11. The purple points show the experimental data, and the colored histogram is the result of the simulation. Green represents $p(e,e'\mathrm{K}^+)\Lambda$ events, and red represents $p(e,e'\mathrm{K}^+)\Sigma^0$ events. The HRS Geant4 can reproduce the mass resolution and the tail of the high mass region of the peaks since the HRS Geant4 includes matter in the particle path and radiation effects. Systematic errors resulting from the difference of the missing mass distribution between the experimental data and the simulation are discussed in Sec. 5.4.1.

The missing mass distribution for a tritium target is shown in Fig. 4.12. The left figure shows

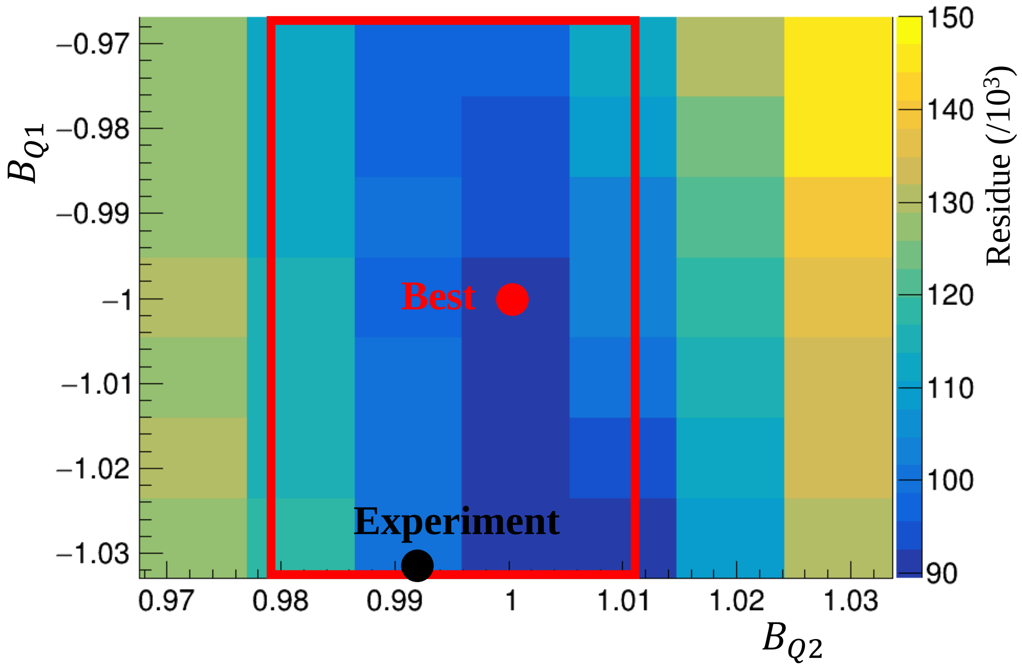

Figure 4.10 Residuals between the experimental data and the simulation. The residuals were calculated for the angular distribution at VDC and target. The B_{Q1} and B_{Q2} are the ratios with respect to the best setting.

the missing mass distribution calculated assuming a tritium target, and the right figure shows the missing mass distribution calculated assuming a hydrogen target. The left figure shows that the data and the simulation agree well in the high mass side. In contrast, near the threshold, there is a discrepancy between the data and the simulation due to the Λn final state interaction or on-mass-shell approximation. As can be seen from the right figure, the partial contamination of the proton target results in contamination of events generated by the $p(e,e'K^+)\Lambda$ reaction. The number of quasi free Σ^0 events is negligibly small in this kinematic setting.

4.4 Evaluation results

The HRS Geant4 simulator was used to calculate the various quantities required for analysis.

4.4.1 K^+ decay and absorption

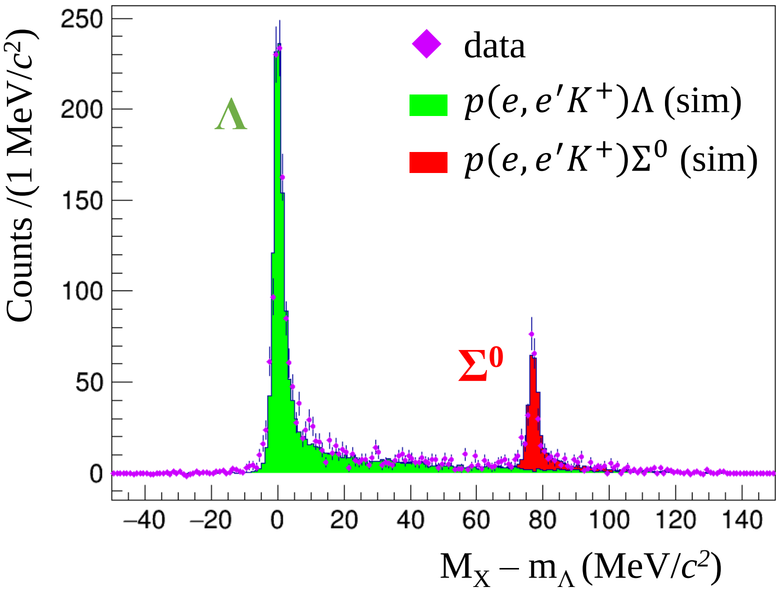

Figure 4.11 Comparison with the Geant4 simulation and data in the case of hydrogen target. The experimental data are shown in purple dots. The simulation results for the $p(e,e'K^+)\Lambda$ and $p(e,e'K^+)\Sigma^0$ reactions are shown in green and red histograms, respectively.

Most K^+ ($c\tau$ = 3.7 m) will decay in the HRS path since the HRS has a long path length of $\sim$ 23 m. This decay rate depends not only on the momentum of K^+ but also on the path length of the particles in the spectrometer. This was investigated using the HRS Geant4 simulator. The results are shown in Fig. 4.13. In the region with large momentum, the survival ratio is larger because the time to reach the spectrometer is shorter. Typically, the survival ratio is 15% for the central momentum (p_K = 1.82 GeV/c).

The K^+ passes through various materials such as target chambers and vacuum membranes before being detected by the detector. Since the K^+N interaction is relatively large, it is necessary to consider the absorption effect of K^+ in the material to derive the production cross section. Absorption here refers to the K^+ that were produced but did not reach the detector. Therefore, it also includes multiple scattering in addition to true nuclear absorption. The materials that exist on the trajectory of K^+ are shown in Tab. 4.1. The absorption rate f_{abs} in the material is obtained by the HRS Geant4 simulation. For a typical value of the central momentum p_K = 1.82 GeV/c, the result is 8.9%. In the actual analysis, the absorption ratio depends on momentum, and the data were corrected for each event.

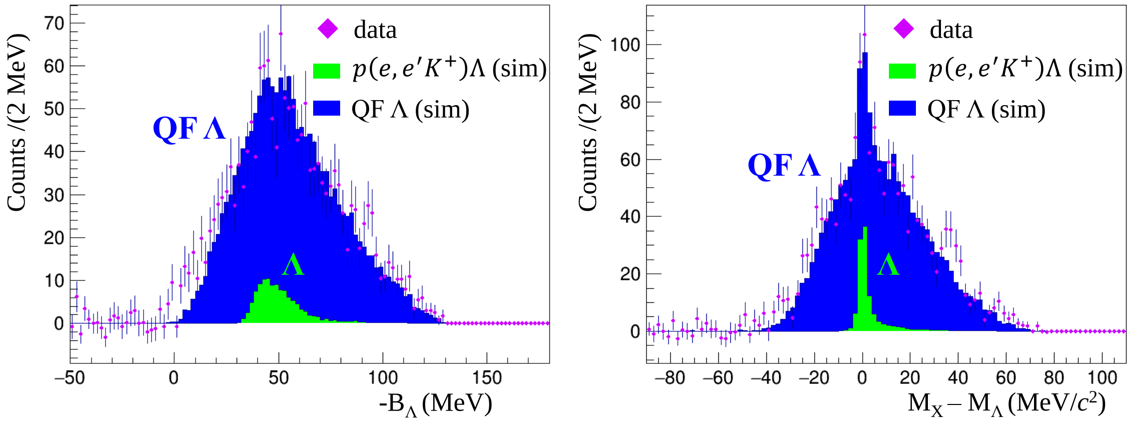

Figure 4.12 Comparison with Geant4 simulation and data in the case of tritium target. The experimental data are shown as purple dots. The simulation results are shown as colored histograms. Left and right figures show missing mass spectra calculated assuming the tritium target and hydrogen target, respectively.

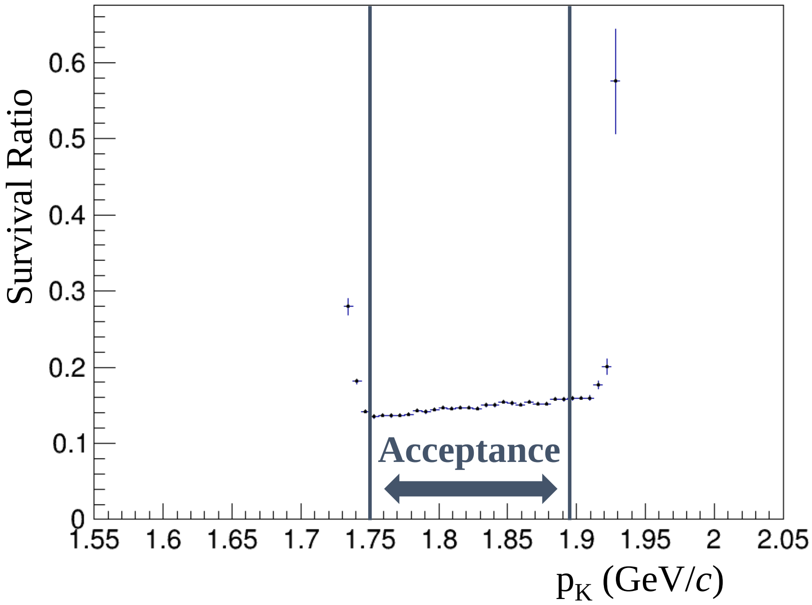

Figure 4.13 K^+ momentum dependence of K^+ survival ratio in HRS-R path. The acceptance region ($|\delta p/p| < 4\%$) is also shown as a blue line.

4.4.2 Acceptance

Acceptance is the solid angle at which the spectrometer can detect particles. The acceptances of spectrometers are a function of momentum. Therefore, the momentum-dependent acceptances of each spectrometer, $\Delta\Omega_{e'}(p_{e'})$ and $\Delta\Omega_K(p_K)$, were obtained and used in the analysis. The momentum and angular distributions of the particles were uniformly produced when estimating the acceptance. When $N_{\rm gen}$ particles ejected in the range of $\Omega_{\rm gen}$ (msr) and N_{acc} are detected, the acceptance $\Delta\Omega(p)$ for a given momentum p is expressed as follows:

$$\Delta\Omega(p) = \frac{N_{\rm acc}(p, \cos\theta)}{N_{\rm gen}(p, \cos\theta)}\Omega_{\rm gen}. \tag{4.24}$$

The magnetic field was taken from the one described in Sec. 4.3.2. The red point in Fig. 4.10 was used as the central value, and the deviations from the central value of the magnetic field within the red line in Fig. 4.10 were treated as systematic errors. The results of the acceptance for HRS-L are shown in Fig. 4.14. The blue dots indicate the acceptance of the central value, and the shaded area indicates the systematic error. The red line is the result of SIMC, i.e., the conventionally used simulator. From this result, the number of virtual photons N_{γ^*} can be obtained. The number of virtual photons is expressed as follows: $N_{\gamma^*} = \Gamma_{\rm int}N_e$, where

$$\Gamma_{\rm int} = \iint \Gamma d\Omega_{e'} dE_{e'}. \tag{4.25}$$

Γ is a quantity calculated using the Eq. (2.7).

The systematic errors were obtained by calculating the acceptance for the magnetic field within the red line in Fig. 4.10, as described above. The errors shown below are averaged over the momentum acceptance of the experiment. The error of the $\Delta\Gamma_{\rm int}$ was estimated to be 8.5%. If we define $\Delta\Omega_K \times \epsilon_{\rm decay} \times \epsilon_{\rm absorp}$ as $\Delta\Omega_{\rm all}$, the error of $\Delta\Omega_{\rm all}$ was estimated to be 7.6%. Here, $\epsilon_{\rm decay}$ and $\epsilon_{\rm absorp}$ represent the efficiencies of K^+ decay and absorption, respectively. The difference of from SIMC in $\Gamma_{\rm int}$ was also 2%, which was within the range of systematic errors.

4.4.3 Energy loss correction

The particles lose their energy in the material. Therefore, the momentum measured by BCM and HRS spectrometers are different from the momentum at the hyperon production. The momentum loss should be corrected to calculate the missing mass accurately. The momentum used for mass reconstruction $p^{\rm real}$ is represented as

$$p_e^{\rm real} = p_e^{\rm mea} - \Delta p_e \tag{4.26}$$
$$p_{e'}^{\rm real} = p_{e'}^{\rm mea} + \Delta p_{e'} \tag{4.27}$$
$$p_K^{\rm real} = p_K^{\rm mea} + \Delta p_K, \tag{4.28}$$

where $p_e^{\rm mea}$ is the momentum measured with BCM and $p_{e'}^{\rm mea}$, $p_K^{\rm mea}$ are the momentum measured in HRS-L, HRS-R, respectively. Δp is the momentum loss in the material. Especially,

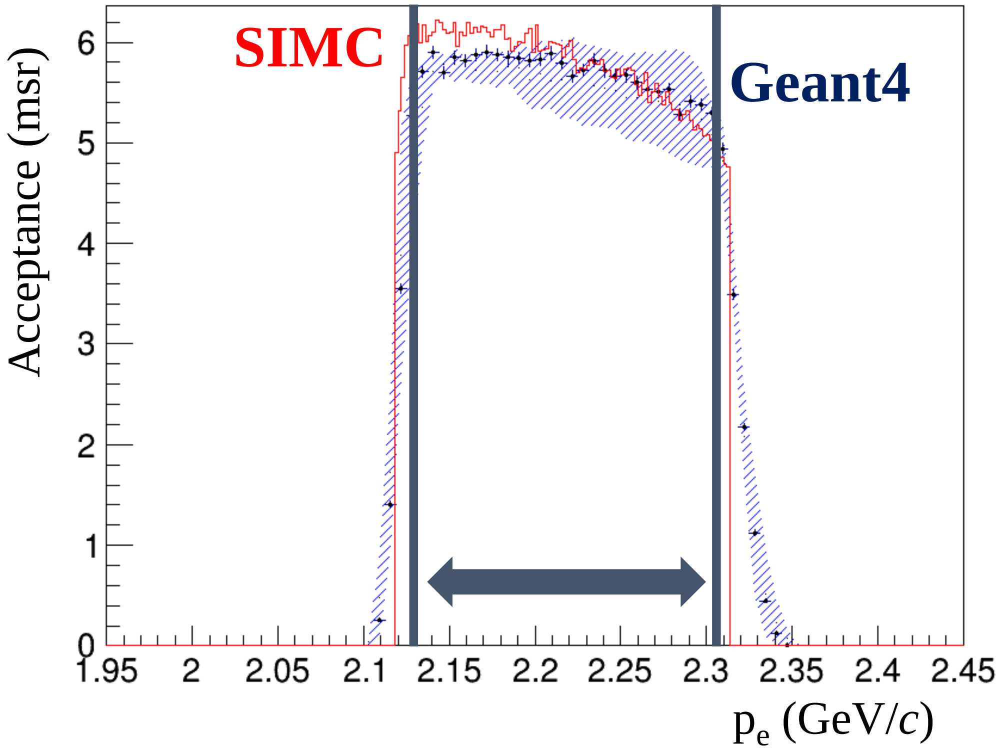

Figure 4.14 Acceptance estimated by the HRS Geant4 and SIMC. The result of the HRS Geant4 is shown as blue points, and the blue shaded area represents the systematic error. The result of SIMC is shown as a red solid line.

the target cell and air have significant effects on the energy loss. The electrons lose their energy more than K^+ due to the radiation effect.

As for the target cell, special corrections are required because of the shape. The thickness of the target cell is shown in Tab. 4.2 and the name scheme is shown in Fig. 4.15. The thickness of the target cells for H and ^{3}H are typically 424.83 μm and 427.50 μm, although it has a systematic error of 25% and 7.6% depending on the position of the cell, respectively. The cell, which is called the cigar-type cell, can be separated into two parts based on the difference in the energy loss as shown in Fig. 4.16. The central part is cylindrical and the downstream part is hemispherical. We measured the particles at 13.2° to the beam direction; thus, the particles pass through a distance of $1./\sin 13.2^\circ$ (≈ 4.4) times their actual thickness when the particle crosses the cylindrical part. In this case, the energy loss is $\sim$ 1 MeV and has a significant effect on the energy accuracy and resolution. Moreover, this has y'_T dependence because the actual thickness depends on the particle angle. In the case of the hemispherical part, particles pass through the actual cell thickness and the energy loss is relatively small. We distinguished whether the particles passed the cylindrical or hemispherical part depending on the reaction point z_T. From the geometric calculations, the division point was determined to be $z_T = 8.0$ cm, which is downstream in the target.

The results of these energy loss estimations are shown in Fig. 4.17. This shows the y'_T angle dependence of energy loss. The solid line shows the energy loss of the cylindrical part, and the dotted line shows that of the hemispherical part. Polynomial functions were used as the correction function. The momentum of the particles were corrected event by event with these functions. The systematic error of cell thickness affect the mass accuracy and will be described in Sec. 5.3.2.

The energy loss of each particle follows a Landau distribution. If the MPVs of two Landau distributions are x MeV and y MeV, the MPV of the sum of the two Landau distributions is not $x + y$ MeV because the Landau distribution is asymmetric. Therefore, even if the energy loss is corrected for each particle, there will be a discrepancy when the missing mass is reconstructed. This was also estimated by reconstructing the missing mass in the HRS Geant4.

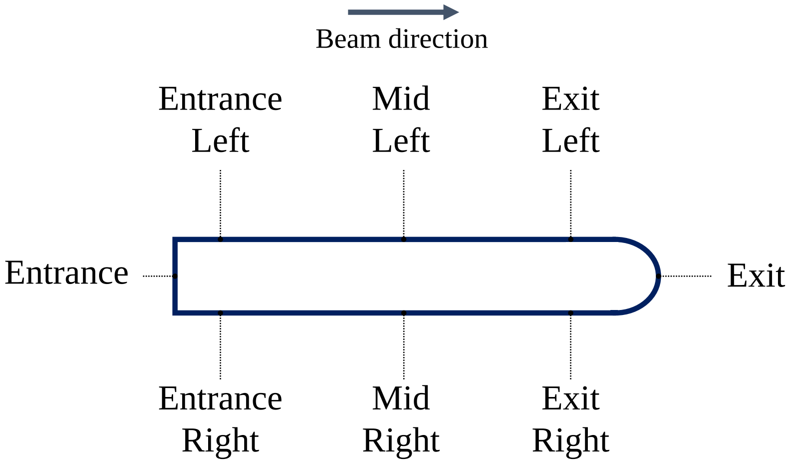

Figure 4.15 The name scheme of cell thickness.

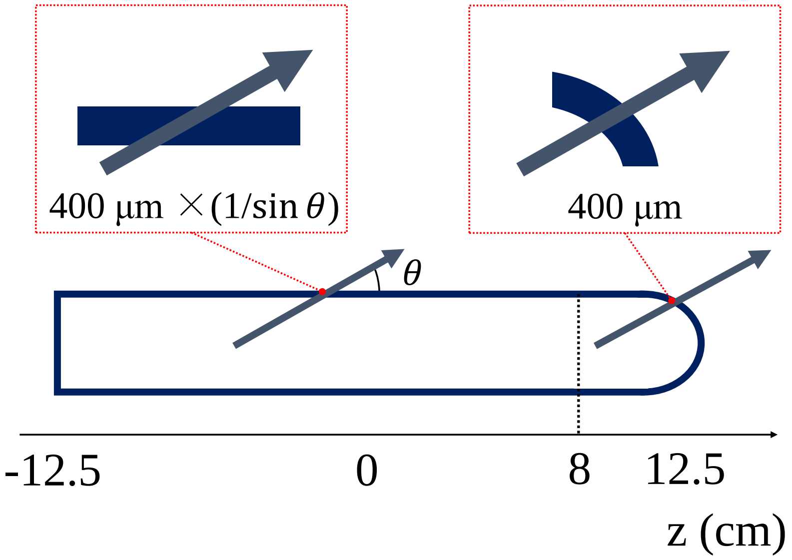

Figure 4.16 An illustration of the energy-loss correction for the the target cell.

Table 4.2 The measurement values of cell thickness. The names of location are shown in Fig. 4.15. These data are taken from [45]. Unit in mm.

Location	Empty cell	^{3}H Cell	^{1}H Cell	^{2}H Cell	^{3}He Cell
Entrance	0.254±0.005	0.253±0.004	0.311±0.001	0.215±0.004	0.203±0.007
Exit	0.279±0.005	0.343±0.047	0.330±0.063	0.294±0.056	0.328±0.041
Exit left	0.406±0.005	0.379±0.007	0.240±0.019	0.422±0.003	0.438±0.010
Exit right	0.421±0.005	0.406±0.004	0.519±0.009	0.361±0.013	0.385±0.016
Mid left	0.457±0.005	0.435±0.001	0.374±0.004	0.447±0.009	0.487±0.060
Mid right	0.432±0.005	0.447±0.004	0.503±0.005	0.371±0.012	0.478±0.007
Entrance left	0.508±0.005	0.473±0.003	0.456±0.010	0.442± 0.005	0.504±0.003
Entrance right	0.424±0.005	0.425±0.003	0.457±0.006	0.332±0.011	0.477±0.011

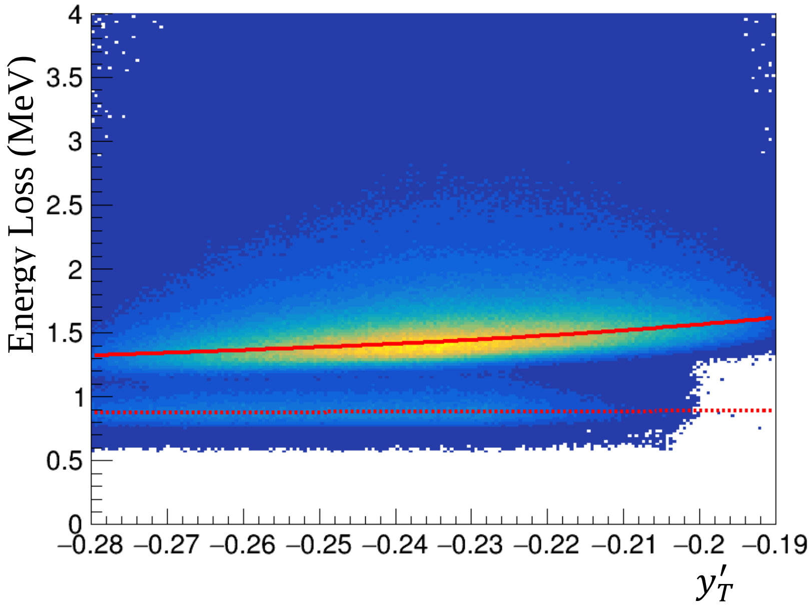

Figure 4.17 y'_T dependence of energy loss of electron in HRS-L. The solid line shows the energy loss of the cylindrical part, and the dotted line shows that of the hemispherical part.

Chapter 5

Results and Discussion

5.1 Derivation of the differential cross section

The cross section of the hypernuclear electro-production by the $\gamma^{(*)}p$ reaction is defined as follows:

$$\overline{\left(\frac{d\sigma}{d\Omega_K}\right)} = \frac{\int_{\mathrm{HRS-R}} d\Omega_K \left(\frac{d\sigma}{d\Omega_K}\right)}{\int_{\mathrm{HRS-R}} d\Omega_K}$$
$$= \frac{1}{N_T}\frac{1}{N_{\gamma^*}}\sum_{i=1}^{N_{\mathrm{HYP}}}\frac{1}{\epsilon_i \Omega_i^{\mathrm{HRS-R}}}, \tag{5.1}$$

where N_T and N_{γ^*} are the number of target nuclei and virtual photon, ϵ_i is the efficiency, and $\Omega_i^{\mathrm{HRS-R}}$ represents the HRS-R acceptance estimated by the HRS Geant4. The efficiencies are summarized in Tab. 5.1. The cross section of this experiment is shown in Fig. 5.1.

Although the accidental background can be estimated using the side-band data of the coincidence time, mixed event analysis was used to improve the statistics. First, we divided the distribution of coincidence time into 2 ns intervals, which are the cycles of the beam electron. Next, we selected two different accidental regions of the distribution. The missing mass was reconstructed by randomly selecting an event for each region as shown in Fig. 5.2. By scaling this to the correct number of events, the accidental background with increased statistics can be obtained. The bunches selected for the side-band data are the same as described in Sec. 3.3.1. The systematic error was 1.9%, which was determined by the number of events used in the mixed event analysis.

The missing mass distribution of the $^3\mathrm{H}(e,e'K^+)nn\Lambda$ reaction appear to be some excess around the $nn\Lambda$ threshold ($-B_\Lambda \sim 0$ MeV). To evaluate this excess quantitatively, the spectral fit should be performed. The mass resolution and shape of the $nn\Lambda$ signal were required to perform the fit and will be estimated in the following section.

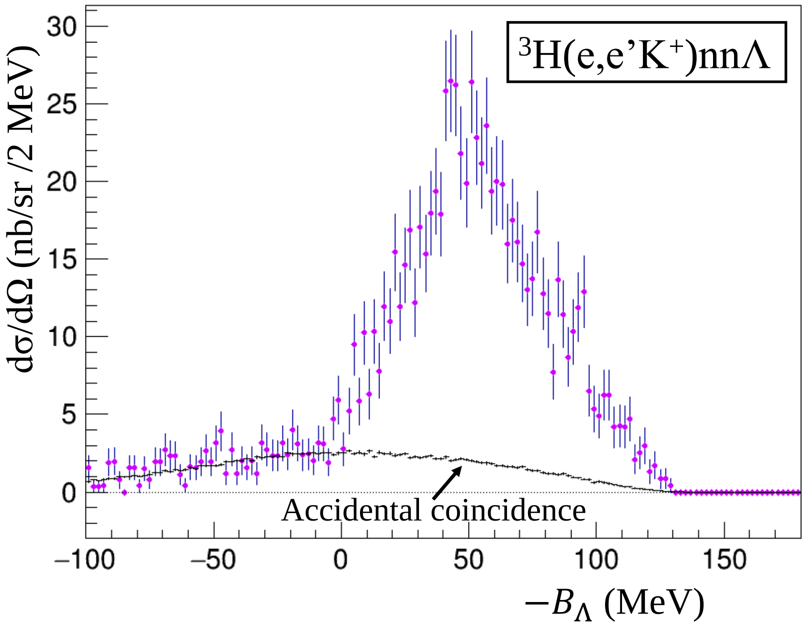

Figure 5.1 Differential cross section for the ^{3}H$(e, e'K)nn\Lambda$ reaction. The only statistical errors are shown in this histogram. The black points show the accidental coincidence background. The distribution was obtained with mixed event analysis using the experimental data.

5.2 Missing mass resolution

The mass resolution in the ^{3}H$(e, e'K^+)nn\Lambda$ reaction needs to be estimated to search for $nn\Lambda$ state. However, since the significant peak has not been observed in the spectrum for the tritium target, it cannot be estimated from the experimental data itself. Therefore, the HRS Geant4 was used to estimate the mass resolution.

The missing mass can be calculated using the following equation:

$$M_X = \sqrt{(E_e + M_t - E_K - E_{e'})^2 - (\vec{p_e} - \vec{p_k} - \vec{p_{e'}})^2}, \tag{5.2}$$

where M_t is the mass of target. The mass resolution is represented with the error propagation method as follows:

$$\Delta M = \sqrt{\left(\frac{\partial M}{\partial p_e}\Delta p_e\right)^2 + \left(\frac{\partial M}{\partial p_{e'}}\Delta p_{e'}\right)^2 + \left(\frac{\partial M}{\partial p_K}\Delta p_K\right)^2 + \left(\frac{\partial M}{\partial \theta_{ee'}}\Delta \theta_{ee'}\right)^2 + \left(\frac{\partial M}{\partial \theta_{eK}}\Delta \theta_{eK}\right)^2} \tag{5.3}$$

Table 5.1 Efficiencies and correction factors used for the cross-section calculation in Eq. (5.1).

Item	Efficiency or correction factor
ϵ_{track}	0.981
ϵ_{decay}	0.15 at $p^{\text{cent.}}$
ϵ_{T}	0.986
$1/\epsilon_{\text{He}}$	0.97
ϵ_{DAQ}	0.95
ϵ_{ctime}	0.96
ϵ_{absorp}	0.91 at $p^{\text{cent.}}$
$\epsilon_{\text{density}}$	0.901
ϵ_{vertex}	0.71
ϵ_{PID}	0.91
$1/\epsilon_{\pi}$	0.98

The differential coefficients are represented as follows:

$$\frac{\partial M}{\partial p_e} = \frac{1}{M_{HYP}}\left\{\frac{p_e}{E_e}(M_t - E_K - E_{ep}) + p_{ep}\cos\theta_{ee'} + p_K\cos\theta_{eK}\right\}, \tag{5.4}$$

$$\frac{\partial M}{\partial p_{e'}} = -\frac{1}{M_{HYP}}\left\{\frac{p_{e'}}{E_{e'}}(M_t + E_e - E_K) - p_e\cos\theta_{ee'} + p_K\cos\theta_{e'K}\right\}, \tag{5.5}$$

$$\frac{\partial M}{\partial p_K} = -\frac{1}{M_{HYP}}\left\{\frac{p_K}{E_K}(M_t + E_e - E_{e'}) - p_e\cos\theta_{eK} + p_{e'}\cos\theta_{e'K}\right\}, \tag{5.6}$$

$$\frac{\partial M}{\partial \theta_{ee'}} = -\frac{1}{M_{HYP}}p_e p_{e'}\sin\theta_{ee'} - p_{e'}p_K\sin(\theta_{ee'} + \theta_{eK}), \tag{5.7}$$

$$\frac{\partial M}{\partial \theta_{eK}} = -\frac{1}{M_{HYP}}p_e p_K\sin\theta_{eK} - p_{e'}p_K\sin(\theta_{ee'} + \theta_{eK}), \tag{5.8}$$

where M_{HYP} is a mass of the hypernuclei. Here, $\theta_{e'K} = \pi - \theta_{ee'} - \theta_{eK}$ is assumed because the reaction plane angle at which K^+ is generated is approximately zero. From Eqs. (5.7) and (5.8), which represent the angular resolution, we can see that the contribution of the angle is inversely proportional to M_{HYP}. In contrast, Eqs. (5.4), (5.5), and (5.6), which represent the momentum resolution, show that the contribution of M_{HYP} is small and is less dependent on the target mass number (A). Although the mass resolution was directly estimated with the HRS Geant4 as shown in Sec. 4.1, each component needs to be checked for the confirmation of the A dependence of mass resolution.

5.2.1 Angular resolution

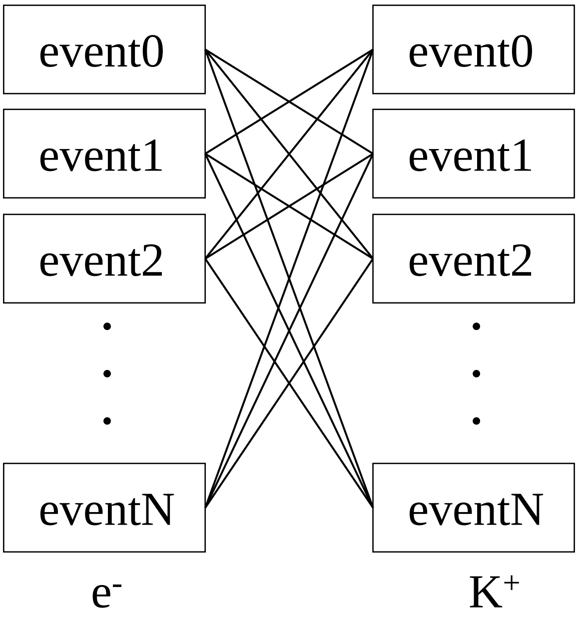

Figure 5.2 Strategy of the mixed event analysis. The accidental coincidence event can be reproduced with randomly mixed events.

The angular resolution was evaluated using the sieve-slit data. It was necessary to subtract the size effect of the sieve-slit hole because the hole itself has a finite size. In addition, the solid angle appears to be smaller toward the edge because the sieve-slit has a thickness of 2.54 cm. Here, $\Delta x'$ and $\Delta y'$ were used as angle parameters since it was easier to estimate $\Delta x'$ and $\Delta y'$ than $\Delta\theta$.

A simple Monte Carlo simulation was performed to estimate the angular resolution. A schematic diagram is shown in Fig. 5.3. We took the sieve-slit data with several carbon foils. The particle direction was uniformly distributed and the straight line was extended to the sieve slit from the position of carbon foils. When the intersection of the line and the sieve slit was in the position of holes, the particle was accepted. The thickness of the sieve slit was also considered. This represents the maximum resolution, i.e., $\Delta x' = 0$ rad and $\Delta y' = 0$ rad. The results of the simulation in this state are shown on the left in Fig. 5.4. The straight line was randomly varied with a Gaussian distribution. An example is shown on the right of Fig. 5.4. The sigma of the Gaussian was determined to match the simulation results and the sieve-slit data (Fig. 3.5). The results are shown in the following.

At first, only the central hole was simply used although the sieve slit has many holes.

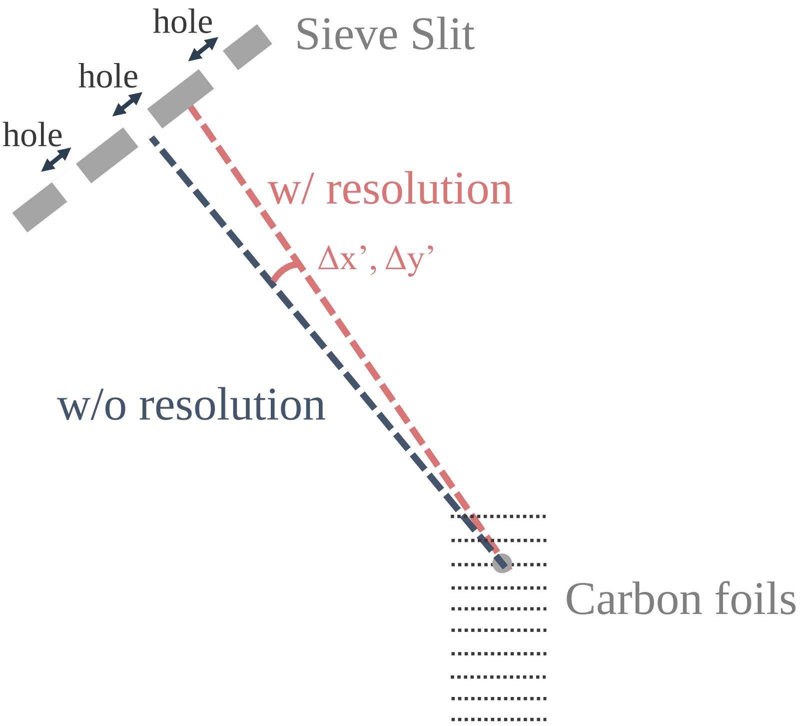

Figure 5.3 Strategy of the simple Monte Carlo simulation for angle resolution estimation.

The central hole was extracted from the data and projected in the x and y directions. The one-dimensional histograms were compared to the simulation. MINUIT method was used for the comparison, and the resolution as the one with the smallest residue was searched. The results are shown in Fig. 5.5. In this case, the resolution was $\Delta x' = 2.23 \times 10^{-3}$ rad and $\Delta y' = 8.95 \times 10^{-4}$ rad.

To examine the resolution including the edge of the sieve slit, the data of an entire row and column were also examined. The resolution in this case was $\Delta x' = 2.37 \times 10^{-3}$ rad and $\Delta y' = 1.52 \times 10^{-3}$ rad. The $\Delta y'$ is worse than that estimated from only the central hole. This may be because the accuracy of y becomes worse toward the edge of the acceptance, as can be seen from the sieve-slit data.

The angular resolution was expected to be worse by Al cell. The Al cell has a thickness of ~ 400 μm, and the particles have an angle of 13.2°, so that it has an effective thickness of $400/\sin 13.2°$ and the effect of multiple scattering is significant as mentioned in Sec. 4.4.3. This effect was estimated by the HRS Geant4 simulator. Materials on the HRS path were incorporated to include the multiple scattering effect. As a result of the simulation, it was found that the case with the Al cell was worse than the case with carbon foil by $\Delta x' =$

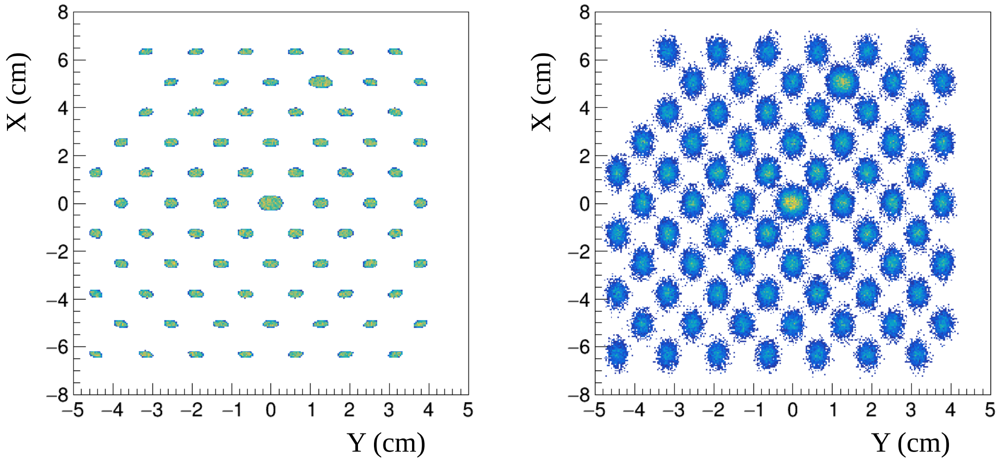

Figure 5.4 Result of Monte Carlo simulation for the sieve slit. The left figure shows the sieve pattern not including resolution. The right figure shows including resolution.

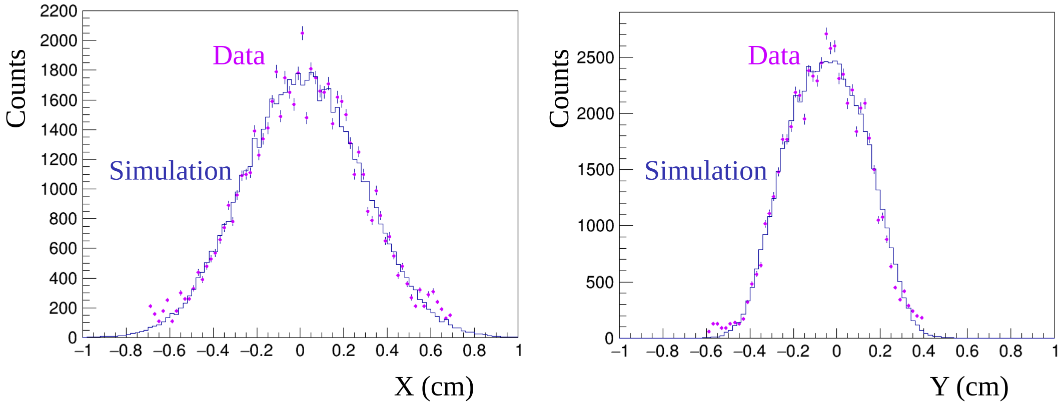

Figure 5.5 Comparison between simulation and data of sieve-slit pattern. Figures show the projection of the center hole profile. Left and right show the x- and y-projections, respectively.

5.0×10^{-4} rad and $\Delta y' = 8.5 \times 10^{-4}$ rad. Finally, the angle resolution with the tritium target was estimated to be $\Delta x' = 2.4 \times 10^{-3}$ rad and $\Delta y' = 1.7 \times 10^{-3}$ rad.

5.2.2 Momentum resolution

The momentum resolution was also estimated with the HRS Geant4 since we did not acquire reference data for momentum resolution. In Sec. 9.2.2 of Ref. [66], results of the elastic scattering of electrons are described. In this study, it is reported that a resolution of $\Delta p/p = 1.1 \times 10^{-4}$ was achieved in the acceptance region at $\delta p/p = 1.5\%$. The momentum resolution was estimated with the HRS Geant4 under the same conditions and was found to be $\Delta p/p = 1.1 \times 10^{-4}$. This agrees with the result of Ref. [66].

The momentum resolution under the same conditions as in the present experiment was estimated with the HRS Geant4. The air and other materials were also taken into account for estimating multiple scattering effects. The momentum resolution for the scattered electrons is shown in Fig. 5.6. The blue line shows $\Delta p/p = 1.3 \times 10^{-4}$ with $z = 0$ and without material, the purple line shows $\Delta p/p = 1.8 \times 10^{-4}$ with z = target length and without material, and the red line shows $\Delta p/p = 4.7 \times 10^{-4}$ with z = target length and with material, which is the same set up as in this experiment.

In actual analyses, a correction function was used to compensate for the energy loss, as shown in Sec. 4.4.3. The red line shifts due to the energy loss. By correcting the energy loss effect, not only the momentum shift is corrected, but also the width is expected to be improved. A Geant4 simulator that implements only the target was constructed, and the difference in momentum resolution between the cases with and without energy loss correction was compared to estimate this effect. The result is shown in Fig. 5.7. The blue line is the result without correction, and the red line is that with the correction. The resolution without energy loss correction is 150 keV. The angular dependence can be corrected, resulting in an increase in the resolution to 100 keV.

The momentum resolution can be decomposed into three items: intrinsic resolution of the spectrometer, energy straggling, and multiple scattering. The intrinsic resolution can be calculated as $1.8 \times 10^{-4} \times 2218$ MeV = 400 keV. Moreover, the overall resolution is known to be $4.7 \times 10^{-4} \times 2218$ MeV = 1040 keV; thus, the contribution of multiple scattering is calculated to be 950 keV. The decomposition of the momentum resolution is shown in Tab. 5.2. The resolution after correction is $\Delta p/p = 4.7 \times 10^{-4}$ as shown in the black line in the Fig. 5.6, which has no large difference due to the large contribution of multiple scattering. The momentum resolution of incident electrons was $\Delta p/p \approx 1.0 \times 10^{-4}$ in FWHM.

Table 5.2 Decomposition of momentum resolution.

	Δp (w/o Ene. Cor.)	Δp (w/ Ene. Cor.)
Spectrometer	400 keV	400 keV
Straggling	150 keV	100 keV
Multi. Scat.	950 keV	950 keV
All	1040 keV	1040 keV

5.2.3 Result

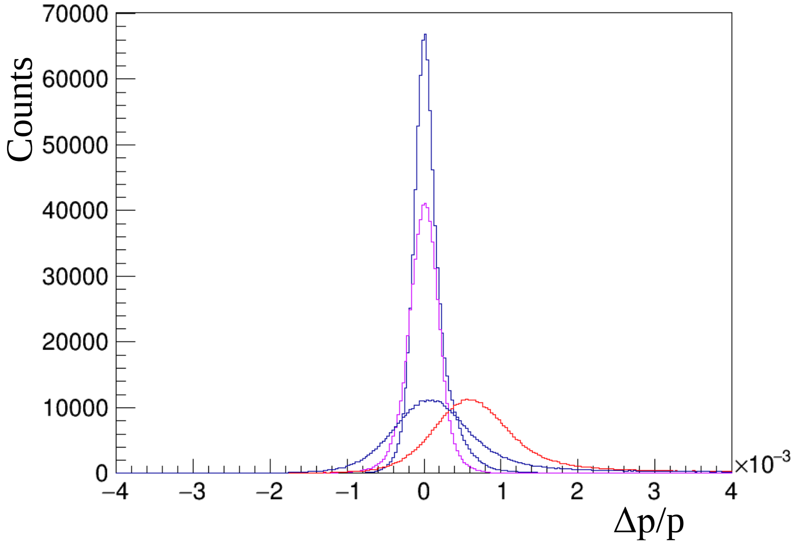

Figure 5.6 Momentum resolution estimated by the HRS Geant4. The blue line shows with $z = 0$ and without material. The purple line shows with $z \in [-12.5, 12.5]$ and without material. The red line shows with $z \in [-12.5, 12.5]$ and with material. The black line shows after the energy loss correction for the red line.

The mass resolution was estimated using the HRS Geant4 and found to be $\sigma = 1.4 \pm 0.1$ MeV/c^2 for Λ. This agrees with the experimental value of $\sigma = 1.3 \pm 0.1$ MeV/c^2. In the same way, the mass resolution for $nn\Lambda$ was found to be $\sigma = 1.5 \pm 0.2$ MeV/c^2. The above systematic error is mainly due to the error in the magnet setting described in Sec. 4.3.2.

5.3 Systematic uncertainties

5.3.1 Cross section

Systematic errors related to efficiencies have been discussed in Chap. 3 and Chap. 4. These systematic errors are summarized in Tab. 5.3. ΔN_{HYP} will be discussed in Sec. 5.4.1. Table 5.3 shows common systematic errors for the events, and the total result is shown as a sum of these squares. The systematic errors due to $\Delta\Omega_K$ were calculated separately because they were used for each event.

5.3.2 Mass accuracy

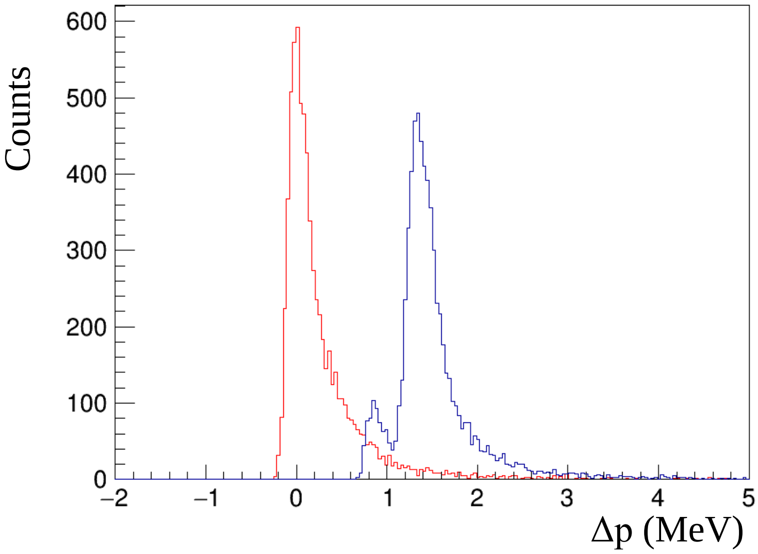

Figure 5.7 Momentum distribution before (blue) and after (red) energy correction.

If the number of signals is N and the resolution is σ, the mass accuracy from the statistics is expressed as $\sigma/\sqrt{N}$. In this analysis, the resolution was estimated with the Gaussian function; thus, N was also estimated with the Gaussian integral. The data points in Fig. 4.11 were fitted with the Gaussian function. Here, the number of Λ's in the region represented by the Gaussian was 830, and the number of Σ^0's was 220. The accuracy from the statistics was calculated to be $\Delta B_\Lambda = \pm 0.1$ MeV. The accuracy becomes worse by the number of events missed in the radiative tale. The number of $p(e, e'K)\Lambda/\Sigma^0$ reactions in the whole region was 1899, which means that 45% events are included in the radiative tale. The systematic error of B_Λ from transfer matrix tuning was already studied in Ref. [30] and was estimated to be less than 0.1 MeV.

The uncertainty of the thickness of the Al cell causes the largest error in the mass measurement. The thickness of hydrogen cell and tritium cell have uncertainties of 25% and 7.6%, respectively, as described in Sec. 4.4.3. If the thickness is estimated improperly, the energy loss cannot be corrected properly. We denote ΔM_H^Λ as the mass difference in Λ resulting from the uncertainty in the thickness of the hydrogen cell, and ΔM_T^Λ as the mass difference in Λ resulting from the uncertainty in the thickness of the tritium cell. If the hydrogen cell thickness is incorrectly estimated, there will be a shift in the peak mass of Λ in the setting of $M_{\text{calib.}}$. Since matrix tuning uses the mass of Λ, Σ^0 as a reference, the momentum matrix is distorted to reproduce the peak value of Λ, Σ^0. This distortion is reflected in the setting of $M_{\text{phys.}}$; thus, there will be a deviation of ΔM_H^Λ in the tritium cell, even if the thickness of the

Table 5.3 Relative errors for the efficiencies and correction factors that contributed to the uncertainty on the cross-section calculation in addition to the acceptance uncertainties.

Item	Relative error
$\Delta\epsilon_{\mathrm{track}}$	0.2%
$\Delta\epsilon_{\mathrm{T}}$	0.3%
$\Delta\epsilon_{\mathrm{He}}$	0.7%
$\Delta\epsilon_{\mathrm{DAQ}}$	0.1%
$\Delta\epsilon_{\mathrm{ctime}}$	0.5%
$\Delta\epsilon_{\mathrm{density}}$	1.1%
$\Delta\epsilon_{\mathrm{vertex}}$	7.8%
$\Delta\epsilon_{\mathrm{PID}}$	6.9%
$\Delta\epsilon_{\pi}$	1.8%
$\Delta\epsilon_{\mathrm{multi}}$	1.3%
$\Delta\Gamma_{\mathrm{int}}$	8.5%
ΔN_e	1.0%
ΔN_T	0.9%
ΔN_{HYP}	6.8%
Side band estimation	1.9%
Total	15%

tritium cell is estimated correctly. In contrast, if the thickness of the tritium cell is incorrectly estimated, an error ΔM_T^{Λ} will be caused by the error in the correction function. To prevent the deterioration of the mass accuracy due to the above effects, calibration was performed using the hydrogen contamination in the tritium cell. Since the tritium cell contained several percent of hydrogen, the Λ peak could be observed by recalculating the missing mass assuming the mass of hydrogen. This is shown in Fig. 5.8. Since there is a large amount of background due to the quasi free Λ coming from the tritium, fitting was performed by representing the BG as a polynomial and the signal as a Gaussian function. The function is shown by the red line in Fig. 5.8. The position of the Λ peak was -0.3 ± 0.3 MeV. Therefore, this value was used to correct for the shift. The error in the accuracy resulting from $\Delta M_{H,T}^{\Lambda}$ was estimated to be $\Delta B_{\Lambda} = \pm 0.3$ MeV.

Furthermore, a systematic error $\Delta M^{nn\Lambda}$ exists due to the difference in kinematics between Λ and $nn\Lambda$. Since the above correction for the hydrogen in the tritium cell is based on the assumption of a hydrogen target, it is necessary to estimate how much the peak position can be shifted in the case of a tritium target. Figure 5.9 shows the simulation results for the case of a tritium cell with a thickness of 428 μm. In the figure, the peak position of Λ is 425 ± 11 keV and

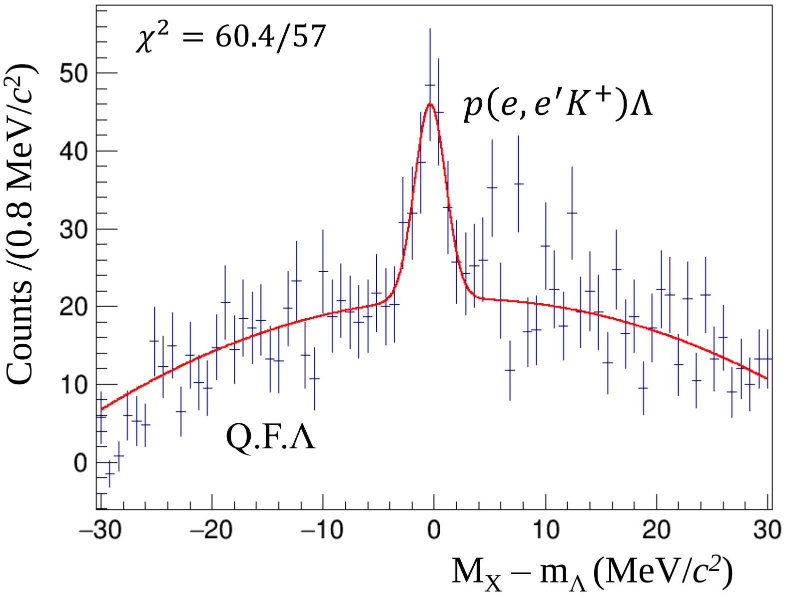

Figure 5.8 Missing mass distribution of ^{3}H$(e, e'K^+)X$ reaction assuming hydrogen target.

that of $nn\Lambda$ is 513 ± 25 keV, indicating a significant difference. The difference was estimated to be $\Delta B_\Lambda = \pm 0.1$ MeV by changing the cell thickness in the range of uncertainties. This is thought to be because the contribution from the momentum correction is stronger when the mass number is larger. Summarizing all the above uncertainties, the error of the mass accuracy was estimated to be 0.4 MeV.

5.4 Upper limit

5.4.1 Fitting function

Three response functions for accidental background, quasi-free Λ (QF) production, and $nn\Lambda$ signal are necessary for the fitting.

The shape of the accidental background was obtained from the mixed event analysis as described in Sec. 5.1. The function is flat around the threshold and does not make sharp peaks as shown by the black points in Fig. 5.1. This was fitted with a quadratic function in the fitting region. The scale was fixed from the number of events; thus, this function including the scale was fixed when fitting.

In general, QF is considered to rise at $-B_\Lambda = 0$ MeV and to increase monotonically. The line

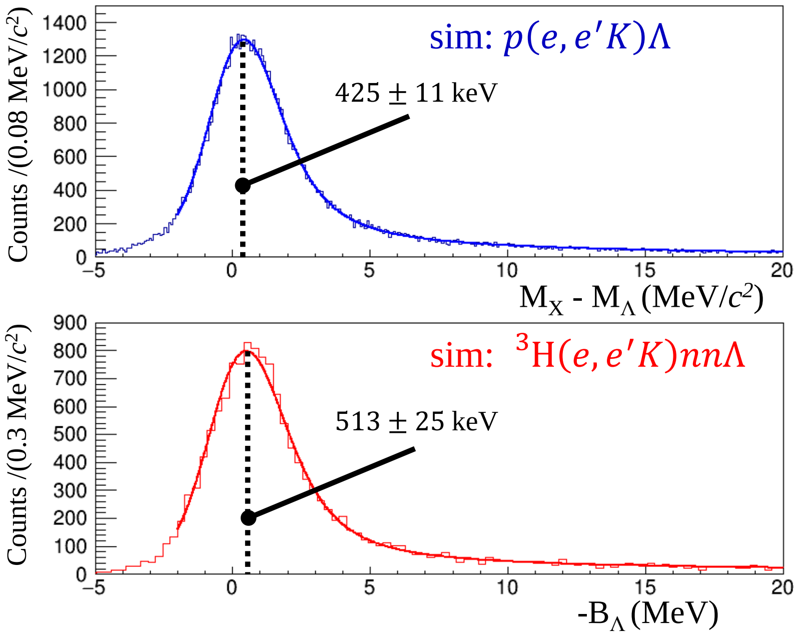

Figure 5.9 Missing mass distributions for $p(e,e'K^+)\Lambda$ and ^{3}H$(e,e'^+)nn\Lambda$ reactions estimated with the HRS Geant4.

shape near the binding threshold may be affected by the Λn final state interaction (FSI); however, this has not been confirmed either in theory or through experimental results. Therefore, a linear function, which is the simplest assumption, was adopted in the present analysis. The above linear function was convoluted with a Gaussian function assuming the experimental resolution to consider the leakage of QF events below $-B_\Lambda < 0$ MeV.

For the $nn\Lambda$ signal, a template function was created. As can be seen from Fig. 3.6 of the $p(e,e'K^+)\Lambda/\Sigma^0$ reactions, the contribution of the radiative tale is significant. Similarly, the $nn\Lambda$ signal is also expected to have a large radiative tale. To obtain a shape that incorporates the radiative tale and the experimental resolution, the HRS Geant4 simulation was used to obtain the spectrum of the $nn\Lambda$ response. The template function was obtained by fitting to this spectrum. This is shown in Fig. 5.10. In addition, to incorporate the natural width of $nn\Lambda$, the function was convoluted with a Breit-Wigner function of the natural width Γ. This is shown in Fig. 5.11. This function was used as a template function.

However, the function estimated by the HRS Geant4 has a slightly smaller number of radiative tails than the experimental data. Since this difference may also exist in $nn\Lambda$, the contribution to the $nn\Lambda$ production cross section was estimated through a simple test. In this test, the strength of the tale in the radiative region was adjusted to reproduce the experimental spectrum of $p(e,e'K^+)\Lambda$ as shown in Fig. 5.12. The black line is the function originally obtained by the HRS Geant4. The red line shows the result of adjusting the radiative region, where

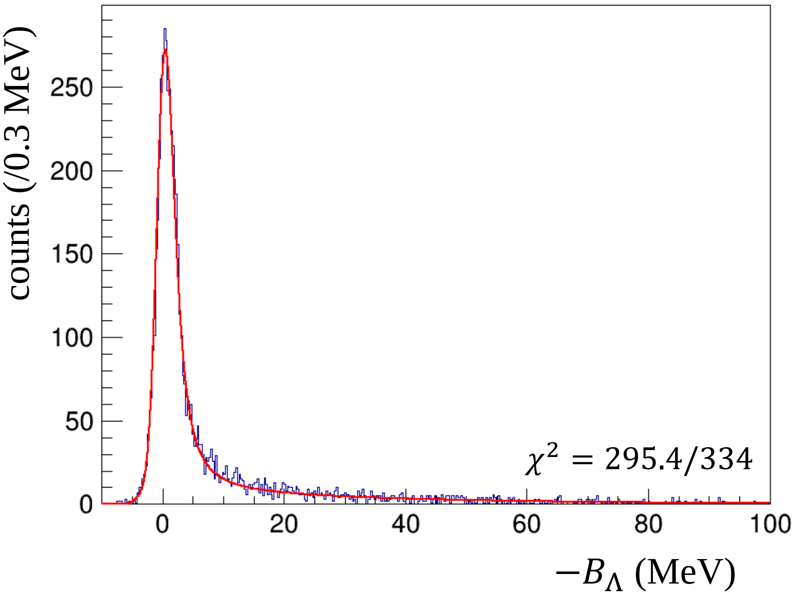

Figure 5.10 $nn\Lambda$ signal estimated with the HRS Geant4.

the number of events in the radiative tails is equal for the experimental data and simulation. This change was also assumed to exist in the $nn\Lambda$ signal. The cross-sections were estimated under this condition, and the difference from the case of the original function was taken as the systematic error. The effect to the cross section was $\Delta M_{\mathrm{HYP}} = \pm 6.8\%$. The differences in the left side of the $p(e, e'K^+)\Lambda$ peak between the HRS Geant4 and the experimental data were also examined in the same test and found to be negligibly small.

5.4.2 Spectral fit

A systematic error due to the binning effect was large in the threshold region where the number of events was limited. The missing mass distribution for the ^{3}H$(e, e'K^+)$X reaction when the binning was changed are shown in Fig. 5.13. The upper left figure is the same as Fig. 5.1, with binning at 2 MeV. The upper right figure shows the result when the splitting is shifted by 1 MeV while maintaining the binning width. The lower left figure and the lower right figure show the results for the binning width of 4 MeV and 6 MeV, respectively. Bin-dependent fitting results in large systematic errors, as can be seen from these figures. Therefore, fitting was performed using the unbinned-maximum-likelihood method. The

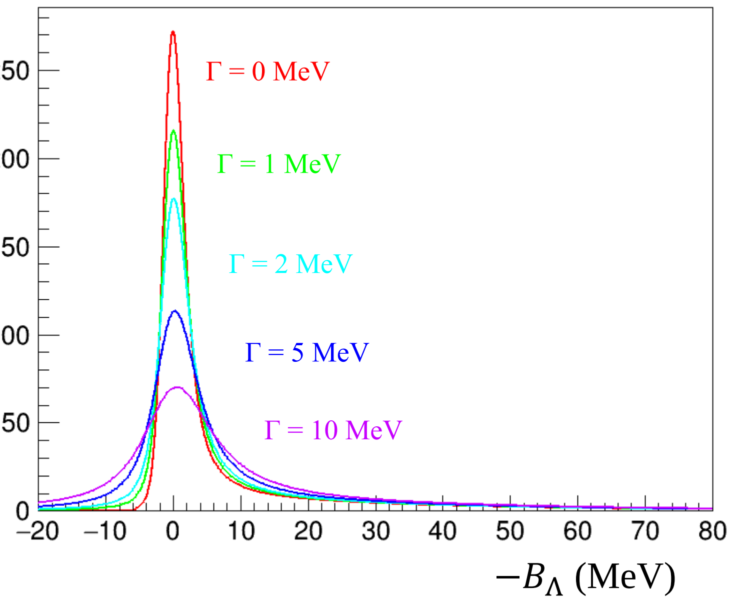

Figure 5.11 Template functions for the $nn\Lambda$ signal. The functions with several widths of Breit-Wigner distributions are shown.

Likelihood was maximized with the parameter θ:

$$L(\boldsymbol{x};\boldsymbol{\theta}) = \prod_{i=1}^{N} f(x_i, \boldsymbol{\theta}), \tag{5.9}$$

where $\boldsymbol{x} = x_1, x_2, ..., x_N$ denotes the cross-section data for each event. $f(x_i, \boldsymbol{\theta})$ is the probability density function (PDF). In this fitting, the sum of QF distribution, accidental background, and $nn\Lambda$ signal were normalized. The $s\sigma$ statistical error is defined as the point where the likelihood difference from the minimum (ΔL) is $s^2/2$. However, since the vertical axis is not in a count but a cross section, correction is necessary. This correction was incorporated as a form of correction to the Hessean matrix that represents the error [68, 69].

5.4.3 Discussion

The upper panel of Fig. 5.14 shows the fitting results assuming that the $nn\Lambda$ signal corresponds to the theoretical prediction $(-B_{\Lambda}, \Gamma) = (0.25, 0.8)$ [19] and $(0.55, 4.7)$ MeV [23], respectively. The red line is the assumed QF distribution, the black dotted line is the accidental background, and the blue line is the $nn\Lambda$ signal. The differential cross sections for the $nn\Lambda$ signal were obtained to be $11.2 \pm 4.8(\text{stat.})^{+4.1}_{-2.1}(\text{sys.})$ nb/sr and $18.1 \pm 6.8(\text{stat.})^{+4.2}_{-2.9}(\text{sys.})$ nb/sr, respectively. In addition, the bottom figure in Fig. 5.14 shows the fitting results when the

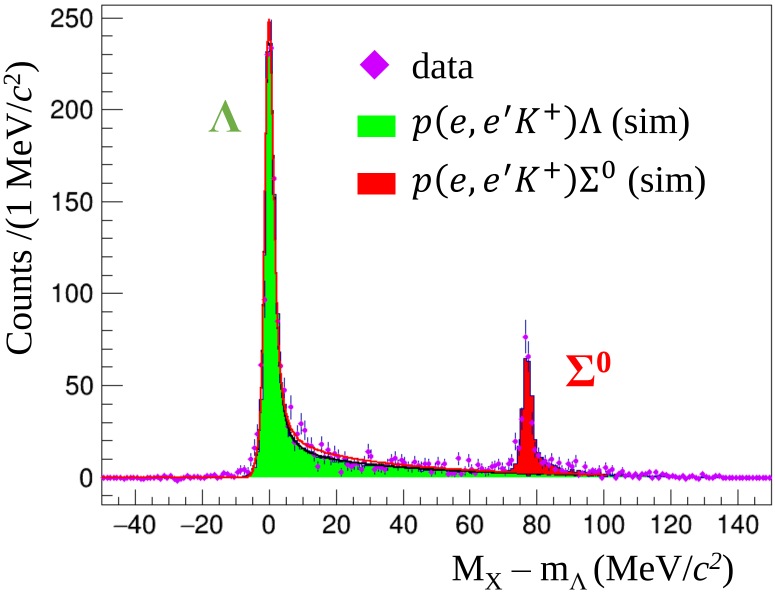

Figure 5.12 The correction for the radiative tale. Black line shows the fitting result without the modification. Red line shows the fitting result with the modification.

binding energy is varied while keeping the width of this theoretical line shape. The horizontal axis shows the peak position of the $nn\Lambda$ signal. The black line shows the 1σ statistical error, and the systematic error is indicated by the selection symbol. Although an excess event can be found around $-5 < -B_\Lambda < 5$ MeV, the statistical significance was not greater than 3σ. Here, a sharp drop in cross section was observed in the $-B_\Lambda > 10$ MeV region. This is considered because the slope of the QF distribution becomes steeper due to the presence of an excess near $-B_\Lambda \sim 0$ MeV, and the cross section of the $nn\Lambda$ signal was reduced in $-B > 10$ MeV to compensate for this. In addition, the fit range is limited to $-B_\Lambda < 20$ MeV because the QF distribution cannot be reproduced by the linear function above $-B_\Lambda > 20$ MeV. Moreover, systematic errors that are not considered in the present analysis are expected in the region where $-B_\Lambda$ is large because the $nn\Lambda$ signal has a large tail on the high mass side.

Since no significant peak were found, the 90%-confidence level (C.L.) of the upper limit of the differential cross section was obtained. The statistical error of 90% C.L. was calculated as follows

$$\frac{\int_0^x g(x)dx}{\int_0^\infty g(x)dx} = 0.90, \tag{5.10}$$

where $g(x)$ denotes the Gaussian function. The final upper limit is the sum of the statistical error and the systematic error. The upper limit assuming $(-B_\Lambda, \Gamma) = (0.25, 0.8), (0.55, 4.7)$ MeV is 21 nb/sr and 31 nb/sr, respectively. In addition, to obtain results independent of the

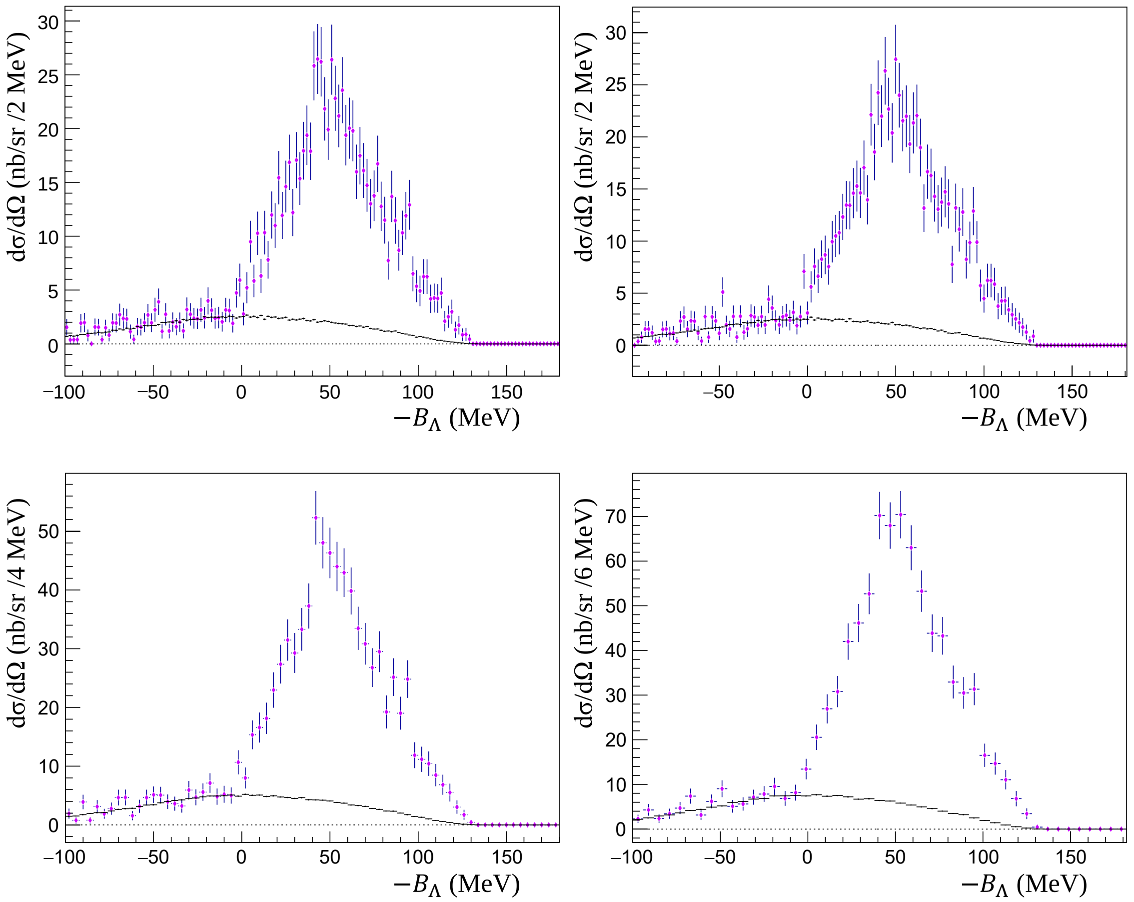

Figure 5.13 The change in histograms for ^{3}H$(e, e'K^{+})nn\Lambda$ reaction due to binning. The upper left figure is the same as the one shown in Fig. 5.1. The upper right figure shows the same binning width but with the binning internally shifted by 1 MeV. The lower left figure and the lower right figure show the histogram when the bin width is doubled and tripled, respectively.

theoretical predictions, two-dimensional scans of $-B_\Lambda$ and Γ were performed. The results are shown in Fig. 5.15. The horizontal axis shows the peak position of the $nn\Lambda$ signal and the vertical axis shows the natural width.

In the current results, a significant peak exceeding 3σ was not found. The reason that the peak structure could not be observed may be due to the small cross section or the broad width of the resonance. In contrast, there are some events around $nn\Lambda$ threshold over the background but we cannot draw definitive conclusions due to the low statistics. It is desired that further experiments would confirm this structure. Schäfer [24, 25] suggests the existence of the resonance is highly depend on the model of Λn interactions. It is calculated that the physical resonance appears with in the NSC97f and Chiral EFT (NLO) but not in the Alexander B and Chiral EFT (LO). In contrast, Afnan's calculations show that there are no resonance in

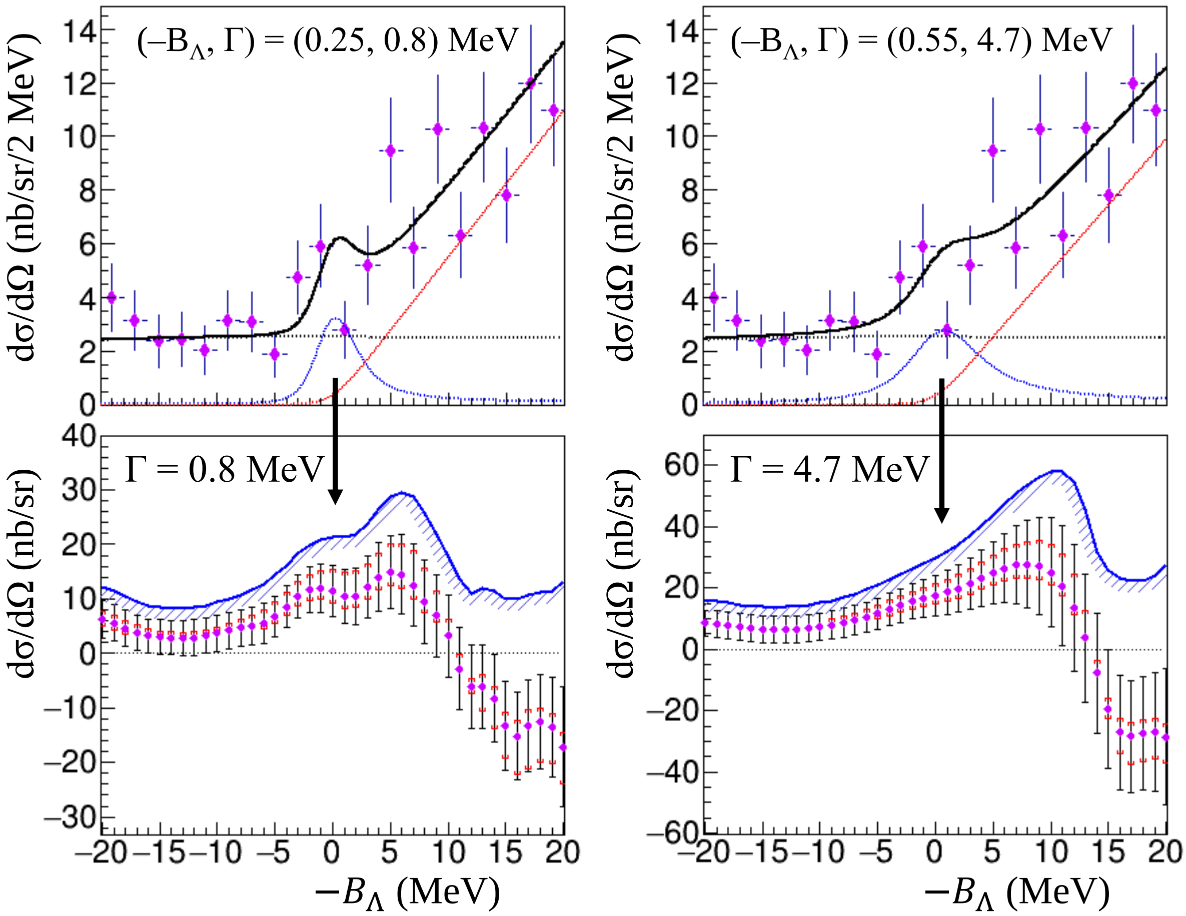

Figure 5.14 The results of the spectral fit assuming the $nn\Lambda$ signal by theoretical calculations. The top figures show the fitting results assuming $(-B_\Lambda, \Gamma) = (0.25, 0.8)$ MeV [19] and $(0.5, 4.7)$ MeV [23], respectively. The blue, red and black dotted lines show the $nn\Lambda$ signal, QF and accidental background, respectively. The black solid line shows the sum of the functions. The bottom figures show the results of the cross section as a function of $-B_\Lambda$ when the natural widths are assumed. The 90% C.L. upper limits are shown in blue solid line.

any interaction. No Λn scattering data exist so far, and the Λn interaction is highly uncertain. If the results of the cross section calculations exist, we can expect to impose limitations on these interactions and calculation methods. However, there are no theoretical work on the production cross section of the $nn\Lambda$ signal in this reaction. It is strongly interesting to compare with the calculation.

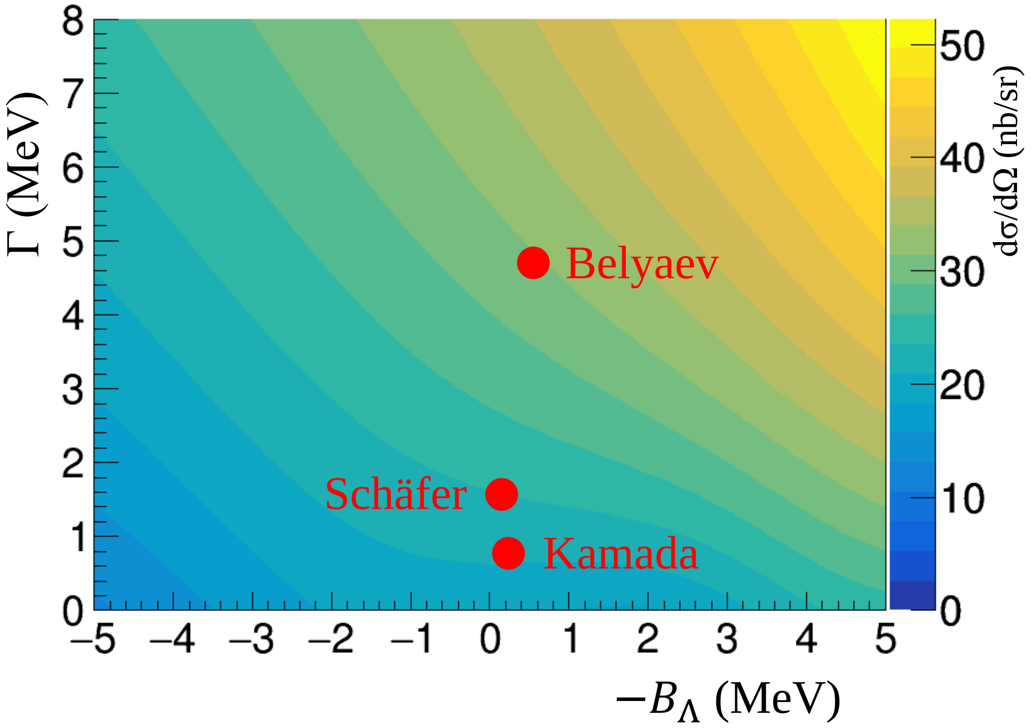

Figure 5.15 The 90% C.L. of the upper limit of the $nn\Lambda$ cross section when the spectral fit was performed by changing B_{Λ} and natural width.

Chapter 6

Summary

The existence of the $nn\Lambda$ state was claimed by the HypHI collaboration at GSI. However, considering that ${}^{3}_{\Lambda}$H with $I = 0$ is a weakly bound state, it is difficult for the $nn\Lambda$ state with $I = 1$ to be bound. For example, the existence of a bound state ($-B_{\Lambda} < 0$) is considered difficult in theoretical calculations using the models that explains the currently observed few-body hypernuclei. In contrast, some papers suggest the existence of a resonant state ($-B_{\Lambda} > 0$), but the results strongly depend on the Λn interaction, which is currently uncertain.

We performed a search experiment for the $nn\Lambda$ state using the ^{3}H$(e, e'K^{+})X$ reaction at JLab in 2018. We used a 4.32-GeV/c electron beam at CEBAF in JLab. In the electro-production of hypernuclei, high mass accuracy can be achieved by using $p(e, e'K^{+})\Lambda/\Sigma^{0}$ reactions as reference. It is also possible to explore a wide range of binding energy from bound to resonant state. Scattered electrons and K^{+} were measured with two spectrometers, HRS-L and HRS-R. The central momenta of the electron and K^{+} were 2.22 GeV/c and 1.82 GeV/c, respectively, and the central angles of HRSs were set at 13.2° with respect to the electron beam.

To estimate some physical quantities, such as acceptance and resolution, we developed a Monte Carlo simulator (HRS Geant4) for this experiment. The HRS Geant4 was successful to reproduce the experimental data. The estimated mass resolution for Λ is 1.4 ± 0.1 MeV/c^{2}, which agrees with the experimental value of 1.3 ± 0.1 MeV/c^{2}. The mass resolution for the $nn\Lambda$ state was also estimated to be 1.5 ± 0.2 MeV/c^{2} by using the simulation. The differential cross section of the ^{3}H(γ^{*}, K^{+})X was calculated by estimating efficiencies and correction factors with the experimental data and the HRS Geant4.

The obtained missing-mass spectrum for the ^{3}H$(e, e'K^{+})nn\Lambda$ reaction shows some excess around the $nn\Lambda$ threshold. We performed a spectral fit to this distribution to evaluate the excess above expected background events quantitatively. The Breit-Wigner (BW) function for the decay width was convoluted with a response function estimated by the HRS Geant4 to obtain the functional form of the $nn\Lambda$ signal. Typical theoretical predictions that show the small and large decay widths were used for the BW function, which are $(-B_\Lambda, \Gamma) = (0.25, 0, 8)$ and $(0.55, 4.7)$ MeV. The unbinned maximum likelihood was used for the spectral fit since the statistics near the threshold was limited. As a result, no peak that was statistically significant above 3σ was observed. The cross-section upper limits at the 90%-confidence level for the $^3\mathrm{H}(\gamma^*, K^+)nn\Lambda$ reaction were obtained to be 21 nb/sr and 31 nb/sr, when $(-B_\Lambda, \Gamma) = (0.25, 0.8)$ and $(0.55, 4.7)$ MeV were assumed. In addition, the cross-section upper limit with various B_Λ and Γ other than the above fixed assumptions were obtained to provide data that are independent on the theoretical predictions.

Currently, no other experimental or theoretical information is available for the $nn\Lambda$ production cross section. The present data is the first result for the upper limit of the cross section. This has a significant impact on the existence of $nn\Lambda$. In the theoretical calculations, the existence of $nn\Lambda$ resonant states strongly depends on the Λn interactions and calculation methods. Schäfer [24, 25] suggests the resonance peak exists in the NSC97f and Chiral EFT (NLO) but not in the Alexander B and Chiral EFT (LO). The present data will constrain the Λn interaction models by comparing with theoretical calculations. Therefore, theoretical calculations on the cross section are strongly desirable.

In this experiment, we did not observe clear signals of the $nn\Lambda$ state reported by the HypHI collaboration. The next $nn\Lambda$ search experiment is currently being prepared and will be carried out in the spring of 2022 by the HypHI collaboration. Furthermore, a new experiment at JLab can also be designed based on the present result. Experimental attempts such as the above new experiments are indispensable to solve the existence puzzle of the $nn\Lambda$ state.

Acknowledgment

I would like to express my sincere gratitude to my advisor, Prof. Gogami, for his exceptional cooperation. He has always given me a lot of time for my research and has accompanied me for many discussions on minor to major issues. Thanks to his generous spirit, I was able to consult him easily and proceed with my research. It would have been difficult for me to write this paper without his help. In particular, it would have been impossible to publish the paper in three years. Meeting him in graduate school and having the opportunity to do research with him has been a great treasure in my career.

I would also like to thank Prof. Nakamura of Tohoku University for his great support. During our daily meetings, I received a lot of ideas and made considerable progress in my research. Due to the nature of our research, most of our meetings were held in the evening, but he spent a lot of time on the research of JLab, including me. Because of the atmosphere in the group created by Prof. Nakamura, I was able to enjoy my research activities.

I am indebted to Prof. Nagae since I entered the graduate school. He was always concerned about the progress of my research and gave me advice on a wide range of topics, including my research and my career path. The comments he gave me at various times helped me a lot when I was stuck in my research.

I thank all the spokespersons for this experiment for their exceptional help. Prof. Tang, Prof. Reinhold, Prof. Markowitz, Prof. Urciuoli, and Prof. Garibaldi provided me with a great number of discussions that enabled me to complete my research despite the time difference. I would also like to thank them for their assistance during my visit to JLab in the U.S.

I also want to thank Mr. Itabashi, Dr. Bishun, Mr. Okuyama, and Prof. Nagao for conducting the research analysis together. I believe that we were able to create a better paper by conducting numerous analyses and cross-checking together. I have been able to grow as a scientist by working with such talented people.

I wish to thank Mr. Toyama, Mr. Akiyama, Mr. Kaneta, and all the other members of ELS at Tohoku University. Listening to your presentations every month has motivated me to do my own research. In addition, thank you very much for accepting me when I visited Tohoku University.

I would like to express my appreciation to Prof. Miyagawa for his cooperation in the theoretical aspect of my research. He took time out of his busy schedule for me and patiently guided me because I was not familiar with the theory. I also received theoretical guidance in the elementary process from Schäfer and Bydẑovský in a conference in Czech Republic.

I also received a lot of support from the staff of the Nuclear hadron physics laboratory at Kyoto University. Prof. Naruki was especially helpful for my master's thesis. What I learned during this time will be useful in my future career. Prof. Murakami, Prof. Zenihiro, and Prof. Dozono also gave me advice which I was able to utilize in my research. I also enjoyed talking with them about miscellaneous things other than research, and I was able to enjoy my research activities. The "laissez-faire" attitude of the laboratory suited me very well. I was free to do the research I wanted to do, and I could ask questions and discuss with the professors if I got stuck in my research. This atmosphere helped me to acquire the ability to take action.

I would also like to thank everyone who helped us complete our experiments at JLab. Conducting experiments with tritium was very challenging, but we were able to complete our research thanks to their help.

Finally, I would like to thank my family for raising me so far.

Appendix A

Summary of theoretical study

A.1 Bound state

B. W. Downs and R. H. Dalitz (1959) [12]

The first theoretical calculation for a three-body system including hyperons was reported by Downs and Dalitz in 1958, only six years after the discovery of the hyperon. The calculations were carried out by the variational method. As a trial function, the following exponential function with 6 parameters was used.

$$\psi = (e^{-ar_1} + xe^{-br_1})(e^{-ar_2} + xe^{-br_2})(e^{-a_3r_3} + ye^{-b_3r_3}), \tag{A.1}$$

where r_1 and r_2 are the distances between individual nucleons and the Λ particle, and r_3 is the distance between two nucleons. They concluded that it is difficult to bound the $NN\Lambda$ system with I = 1.

K. Miyagawa *et al.* (1995) [13]

Miyagawa *et al.* used the Faddeev method to calculate the $NN\Lambda$ three-body system. The Nijmegen89 potential was used as the YN interaction. The main feature of this calculation is that it incorporates the Λ-Σ conversion. The binding energy of the Hypertriton for $(I, J) = (0, 1/2)$ was successfully explained without heavily relying on NN interactions (Nijmegen93, Paris, Bonn B). Furthermore, the interaction due to Λ-Σ conversion was found to be attractive and played an important role in the binding of hypertriton.

In contrast, the same method was applied to the $I = 1$ state. The interactions used were the Nijmegen89 YN interaction and the Bonn B NN interaction, which successfully explained the hypertriton. As a result of this calculation, there was no bound state for both $J = 1/2$ and $J = 3/2$. Therefore, it was examined by scaling the entire YN interaction to see whether a bound state would appear. For $(I, J) = (1, 1/2)$, the bound state appeared at 1.2 times, and for

$(I, J) = (1, 3/2)$, the bound state did not appear even at 1.32 times. Furthermore, the effect of the Λ-Σ conversion was suggested to be an attractive force for $(I, J) = (1, 1/2)$ and a repulsive force for $(I, J) = (1, 3/2)$.

■ E. Hiyama *et al.* (2014) [14]

Hiyama *et al.* performed variational calculations following the report on the observation of the $nn\Lambda$ bound state at GSI in 2013. The NN interaction is AV8 potential, and the YN interaction is NSC97f, which incorporates ΛN-ΣN coupling. The advantage of using the above interactions is that the binding energies of ${}^{3}_{\Lambda}$H, ${}^{4}_{\Lambda}$H, ${}^{4}_{\Lambda}$He are well reproduced at 0.19, 2.33, 2.28 MeV. Even with these interactions, the $nn\Lambda$ bound state does not exist.

Therefore, by modifying some interactions, a way for the $nn\Lambda$ state to be bound while maintaining the above binding energy was explored. First, the tensor components of the ΛN-ΣN coupling were scaled. Then, the bound state appeared after scaling by 1.2. However, the binding energy of the ${}^{3}_{\Lambda}$H was found to be over bound at $-B_{\Lambda} = 0.72$ MeV, and the excited state of $J = 3/2$, which was not confirmed in the experiment, was also bound. When T=1, the ${}^{1}S_{0}$ component of nn was scaled, and it was found that $nn\Lambda$ was bound by a factor of 1.35. However, since di-neutron (nn) is bound by a factor of 1.13, the $nn\Lambda$ state could not be interpreted by the present nuclear physics.

■ A. Gal and H. Garcilazo (2014)

Gal and Garcilazo discussed the $nn\Lambda$ bound state, and compared the experimental results on the current few-body systems (Λp scattering, ${}^{3}_{\Lambda}$H, ${}^{4}_{\Lambda}$H). As a result, they found that the $nn\Lambda$ bound state cannot be explained by the current understanding of hypernuclei. In particular, Faddeev calculations that incorporate ΛN-ΣN coupling were performed for the comparison with ${}^{4}_{\Lambda}$H. For the YN interaction, the G-matrix $0s_N 0s_Y$ effective interaction developed by Akaishi [70] *et al.* based on the NSC97 was used. Even under this condition, $nn\Lambda$ was unbound, and even when the interaction was adjusted to be bound, dineutron (nn) was bound first. This calculation does not incorporate the effect of the $NN\Lambda$ three-body force which is not directly related to the ΛN-ΣN conversion. However, even if other three-body forces are considered, such as those involving $\Sigma(1385)$, the effect of the attractive force on the $nn\Lambda$ state is still considered to be small compared to that on the ${}^{3}_{\Lambda}$H, and its existence would be still difficult.

■ H. Garcilazo and A. Valcarce (2007, 2014) [16,17]

Garcilazo *et al.* used the chiral constituent quark model to derive interactions. In this model, a baryon is represented as a three-body cluster of constituent quarks, and its mass is generated by spontaneous breaking of chiral symmetry. Here, ΛN-ΣN conversion is incorporated, which includes not only the S-wave but also the D-wave tensor component. The Faddeev equation was solved to calculate the $nn\Lambda$ bound state using this interaction. As a result of the calculation, it was found that the bound state of $nn\Lambda$ is difficult. In contrast, for simplicity, Faddeev calculations were also performed for separate potentials containing only S waves, but the results did not significantly change.

■ Shung-Ichi Ando *et al.* (2015) [18]

Ando *et al.* calculated the $nn\Lambda$ state by solving the coupled integral equation using pionless effective field theory ($\not\pi$EFT) of the leading order. The Lagrangian of this model incorporates three body forces as the contact terms. As a result of this calculation, the possibility of the existence of Effimov states was suggested. However, since the experimental data to determine the parameters of this three-body force are very scarce, no quantitative discussion has been presented.

A.2 Resonant state

■ V. B. Belyaev *et al.* (2008) [19]

Belyaev *et al.* were the first to discuss resonant states in $nn\Lambda$ three-body systems. The resonant state was searched for by calculating the zeros of the three-body Jost function. The model proposed by Nemura *et al.* [20] was used as the interaction. This model is based on the Minnesota potential used for NN potential, and its parameters were determined to reproduce the $A = 3, 4$ Λ-hypernuclei. There are three Λn potentials which were proposed by Nemura *et al.*, and they are denoted A, B, and C. Figure 1.4 shows the potential of the S-state under the assumption of these potentials. In all of them, there is a pocket of weak attraction. The results are shown in Tab. 1.1. It can be seen that there is a broad resonance in A and B, while there is no resonance in C. The results highly depend on how the ΛN potential. These do not incorporate the ΛN-ΣN channel, which may result in a narrower width and closer to the threshold. When this potential was scaled, a bound state appeared at 1.5 times the potential.

■ I. R. Afnan and B. F. Gibson (2015) [21]

Afnan *et al.* performed a Faddeev calculation using the separate potential. The separable potential of a two-body S-wave is described as follows

$$V(k,k') = \frac{1}{k^2+\beta^2} C \frac{1}{k'^2+\beta^2}, \tag{A.2}$$

where C and β are the parameters determined by the scattering length and effective range of the Nijmegen model D potential, respectively. The calculations were performed with and without the tensor force, respectively. These models do not incorporate the ΛN-ΣN conversion and the three-body force. When the calculations were performed without tensor force, the result was $E = -0.154 - i0.753$ MeV and no resonant state existed. However, by multiplying the strength of ${}^1S_0$, ${}^3S_1$ components by 1.07, a resonant state appeared, and by multiplying it by 1.35, a bound state appeared. A similar calculation was performed with various Λn interactions including tensor forces, and no significant differences were observed. Figure A.2 shows the results of the calculations with Nijmegen model D, Chiral EFT, Nijmegen NSC97f, and Julich. The calculation result was $-0.107 - i0.622$ MeV, and no resonant state existed. However, by multiplying ${}^1S_0$, ${}^3S_1$ by 1.05, a resonant state appeared, and by multiplying by 1.25, a bound state appeared.

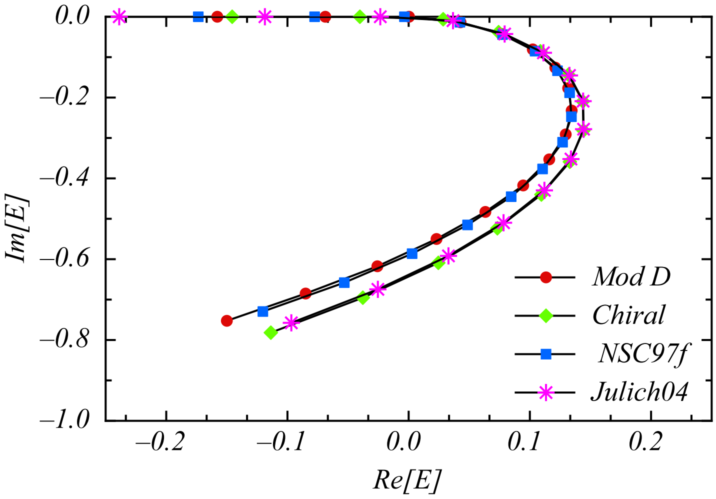

Figure A.1 The pole trajectory of $nn\Lambda$ state taken from Refs. [21]. The trajectories show the dependence of the Λn interaction.

■ I. Filikhin *et al.* (2016) [22]

NSC97f was used as the ΛN potential and MT-I-III semi-realistic NN potential was used as the NN potential. As a result of this calculation, a rather wide range of resonant states in the $E = 0.2 - i1$ MeV range was found. In addition, the following were perturbatively incorporated as three-body forces.

$$V_{3bf}(\rho) = -\delta \exp(-\alpha\rho^2) S(s_\Lambda, s_{NN}) \tag{A.3}$$

where ρ is the hyper-radius:$\rho^2 = x^2 + y^2$ and x, y are mass scaled Jacobi coordinates. In addition, $S(s_\Lambda, s_{NN})$ is a parameter that depends on the spin, and the following two cases were attempted.

$$\frac{S(1/2,1)}{S(1/2,0)} = 1 \tag{A.4}$$

$$\frac{S(1/2,1)}{S(1/2,0)} = 1/3 \tag{A.5}$$

However, it was not possible to create a $nn\Lambda$ bound state while maintaining the bound energy of ${}^{3}_{\Lambda}$H.

■ H. Kamada *et al.* (2016) [23]

YN Nijmegen potential (NijmYN89) was used as the YN interaction and NN Nijmegen potential (Nijm93) as the NN interaction. ΛN-ΣN coupling was also incorporated. The Faddeev equation was calculated by using these interactions. Partial waves were incorporated up to $J_{max} = 4$ or 5. Thus, the resonant states of $E = 0.25 - i0.40$ MeV were found. Moreover, when the YN interaction was changed to NSC97f, the result of $E = 0.60 \pm 0.05 - i(0.25 \pm 0.05)$ MeV was obtained. Furthermore, the YN potential of NSC97f was scaled, and the bound state appeared by multiplying it by 1.2.

■ M. Schäfer *et al.* (2020,2021) [24,25]

The pionless effective field theory ($\not{\pi}$EFT) of the leading order was used as an interaction. The s-wave contact interaction was included as the two-body and three-body force. These parameters were determined to fit the experimental data and theoretical calculations for the A=3, 4 system. For the calculation of bound states, the three-body Schrödinger equation was solved using the stochastic variational method (SVM). In addition, two independent methods—the inverse analytic continuation in the coupling constant method (IACCC) and the complex scaling method (CSM)—were used to enable the calculation of the resonant states. Thus, no $nn\Lambda$ bound state was found, but there existed a resonant state depending on the interaction. The interaction models NSC97f and Chiral EFT (NLO) showed the existence of resonant states, while Alexander B and Chiral EFT (LO) showed no resonant states. The pole position of the resonant state differs depending on the model, but it exists in the energy range of $E \leq 0.3$ and the width range of $1.16 \leq \Gamma \leq 2.00$ MeV.

Appendix B

Determination of the magnetic setting of the HRS Geant4

As described in Sec. 4.3.2, the quadrupole magnetic field setting of the HRS Geant4 was adjusted to satisfy the following,

$$D_L : Q1_L : Q2_L : Q3_L = D_R : Q1_R : Q2_R : Q3_R. \tag{B.1}$$

Q2 and Q3 are identical quadrupole magnets, and the ratio of their magnetic fields is fixed. Therefore, the optimal magnetic field setting was searched by varying the magnetic field of Q1 and Q2. Comparisons were made between experimental data and simulations, and residuals were obtained. As examples, the results of the search for the momentum distribution and y' are shown in Fig. B.1 and B.2. In particular, Fig. B.2 shows that the distributions differ significantly depending on the magnetic field of Q1 and Q2. In Fig. B.1, the distributions also show a slight change. The red line is the region that we adopted as the systematic error in this study, as mentioned in the text. The distributions used for the search are the momentum distributions and the angular distributions at the VDC (x', y'), and the angular distributions at the target (x'_{tg}, y'_{tg}). The residuals were taken for all of these, and the results are shown in Fig. 4.10. A comparison of each distribution in the best setting is shown in Fig. B.3. We found that the momentum distributions agree well when the momentum cut ($|\delta p/p| < 4\%$) was applied. The momentum acceptance and resolution for varying magnetic field of Q1 and Q2 are also shown in Fig. B.4 and B.5, respectively.

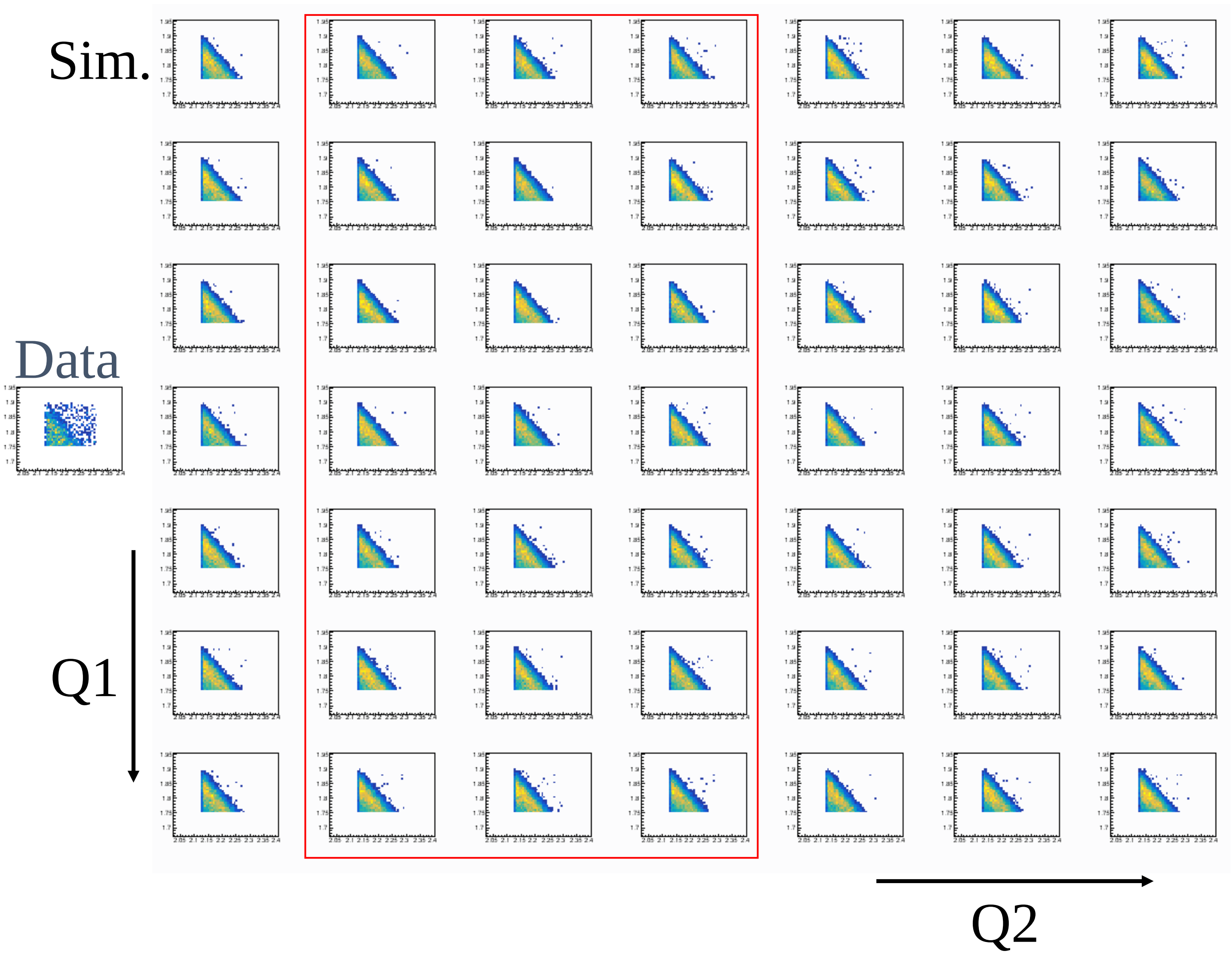

Figure B.1 The momentum acceptance of HRS-L and HRS-R. The left figure shows experimental data. The right figures show the simulation result with changing the magnetic field of Q1 and Q2.

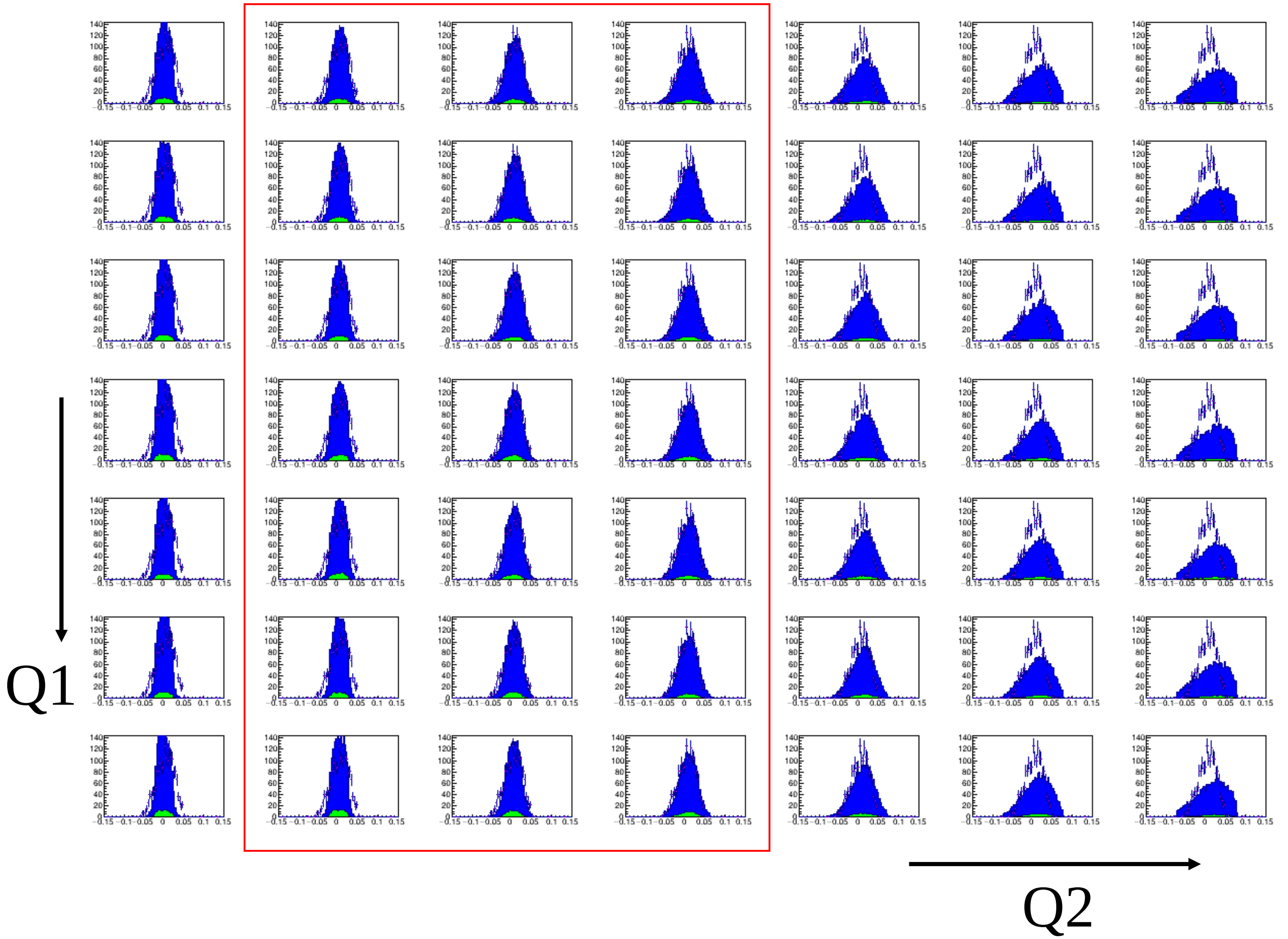

Figure B.2 The y' distribution at VDC. Purple dots show experimental results. Colored histograms show the simulation results. Green shows the events of $p(e,e'K^+)\Lambda$ reaction and blue shows the events of quasi-free Λ.

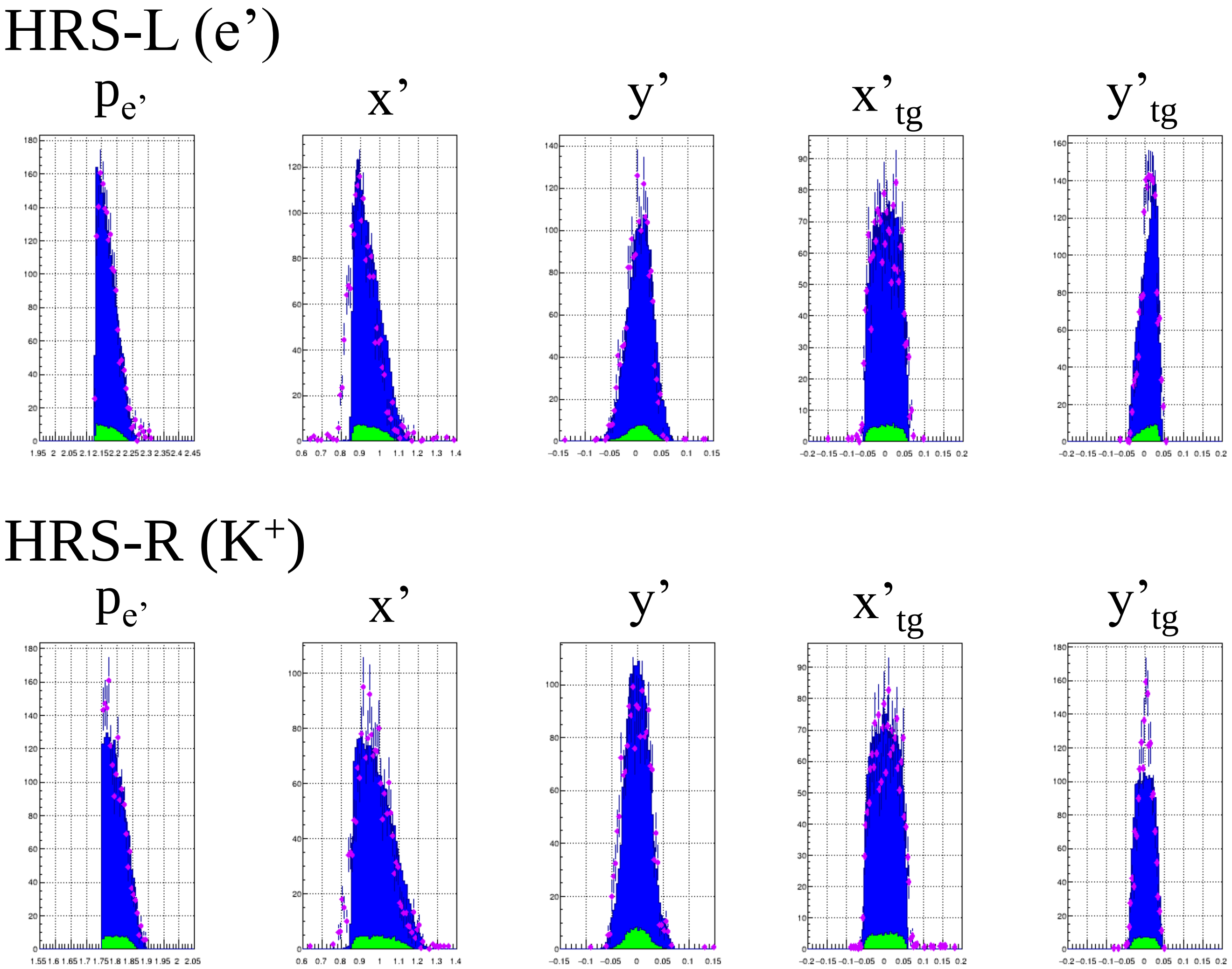

Figure B.3 The comparison between experimental result and simulation. Purple dots show experimental results. Colored histograms show the simulation results. Green shows the events of $p(e,e'K^+)\Lambda$ reaction and blue shows the events of quasi-free Λ.

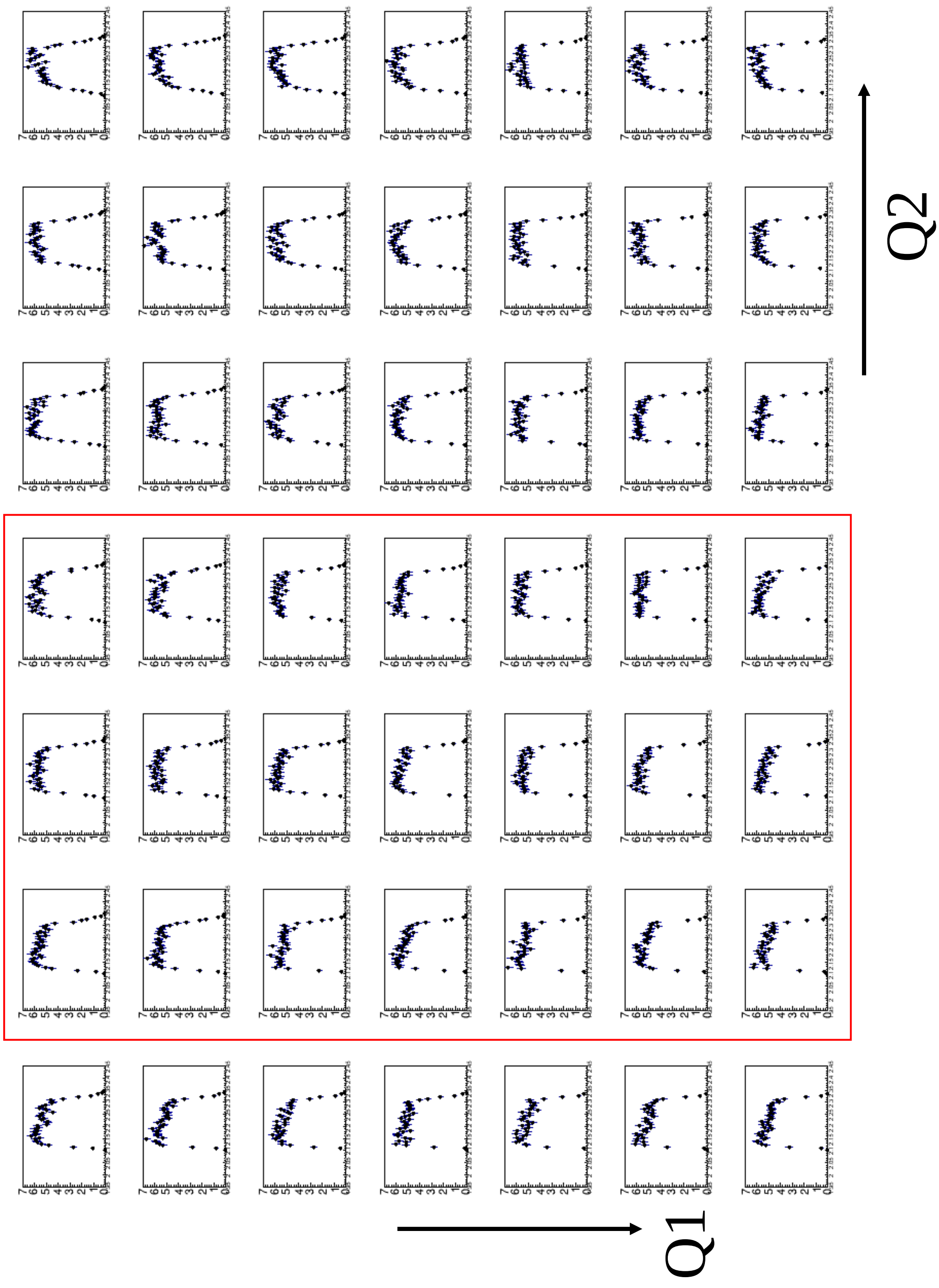

Figure B.4 The simulation results of momentum acceptance.

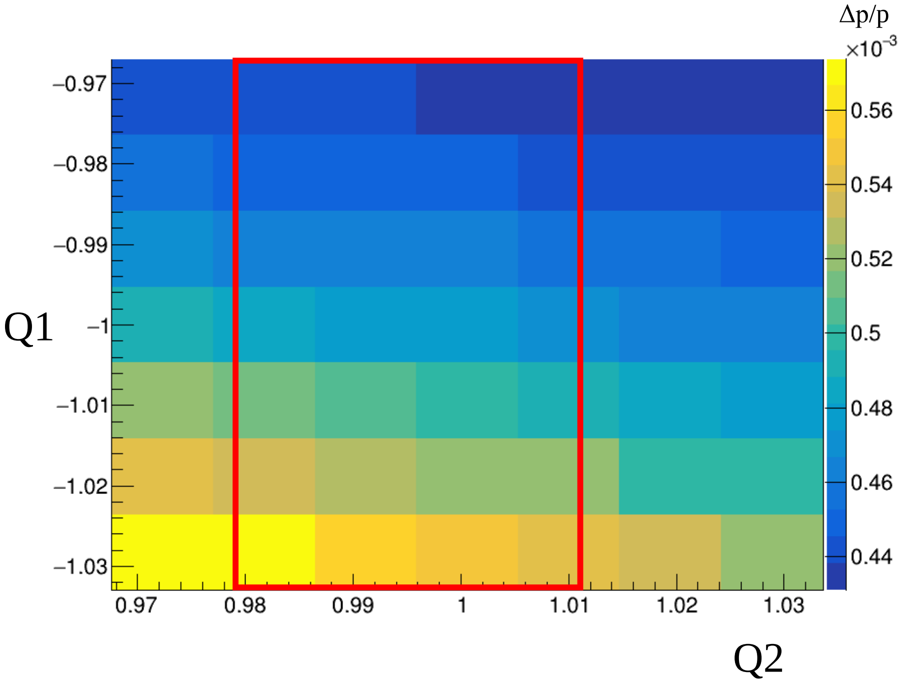

Figure B.5 The simulation results of momentum resolution. The axis shows the ratio with respect to the most consistent magnetic field setting. See the text about the red line.

References

[1] R. B. Wiringa, V. G. J. Stoks, and R. Schiavilla. *Phys. Rev. C*, Vol. 51, p. 38, 1995.

[2] R. Machleidt, F. Sammarruca, and Y. Song. *Phys. Rev. C*, Vol. 53, p. R1483, 1996.

[3] V. G. J. Stoks, R. A. M. Klomp, C. P. F. Terheggen, and J. J. de Swart. *Phys. Rev. C*, Vol. 49, p. 2950, 1994.

[4] A. Esser, et al. *Phys. Rev. Lett.*, Vol. 114, p. 232501, 2015.

[5] T. O. Yamamoto, et al. *Phys. Rev. Lett.*, Vol. 115, p. 222501, 2015.

[6] M. Jurič, et al. *Nucl. Phys. B*, Vol. 52, pp. 1–30, 1973.

[7] J. Adam, et al. *Nature Physics*, Vol. 16, p. 409, 2020.

[8] C. Rappold, et al. *Nucl. Phys. A*, Vol. 913, p. 170, 2013.

[9] C. Rappold, et al. *Phys. Lett. B*, Vol. 728, p. 543, 2014.

[10] C. Rappold, et al. *Phys. Lett. B*, Vol. 747, p. 129, 2015.

[11] C. Rappold, et al. *Phys. Rev. C*, Vol. 88, p. 041001, 2013.

[12] B. W. Downs and R. H. Dalitz. *Phys. Rev.*, Vol. 114, p. 593, 1959.

[13] K. Miyagawa, H. Kamada, W. Glöckle, and V. Stoks. *Phys. Rev. C*, Vol. 92, p. 054608, 2015.

[14] E. Hiyama, B. F. Gibson S. Ohnishi, and Th. A. Rijken. *Phys. Rev. C*, Vol. 89, p. 061302, 2014.

[15] Avraham Gal, et al. *Phys. Lett. B*, Vol. 736, pp. 93–97, 2014.

[16] H. Garcilazo, A. Valcarce, and T. Fernandez-Carames. *Phys. Rev. C*, Vol. 76, p. 034001, 2007.

[17] H. Garcilazo and A. Valcarce. *Phys. Rev. C*, Vol. 89, p. 057001, 2014.

[18] S. Ando, U. Raha, and Y. Oh. *Phys. Rev. C*, Vol. 92, p. 024325, 2015.

[19] V. B. Belyaev, S. A. Rakityansky, and W. Sandhas. *Nucl. Phys. A*, Vol. 803, pp. 210–226, 2008.

[20] H. Nemura, Y. Suzuki, Y. Fujiwara, and C. Nakamoto. *Prog. Theor. Phys.*, Vol. 103, pp. 928–958, 2000.

[21] Iraj R. Afnan and Benjamin F. Gibson. *Phys. Rev. C*, Vol. 92, p. 054608, 2015.

[22] Igor Filikhin, Vladimir Suslov, and Branislav Vlahovic. *EPJ Web of Conf.*, Vol. 113, p. 08006, 2016.

[23] H. Kamada, K. Miyagawa, and M. Yamaguchi. *EPJ Web Conf.*, Vol. 113, p. 07004, 2016.

[24] M. Schäfer, et al. *Phys. Lett. B*, Vol. 808, p. 135614, 2020.

[25] M. Schäfer, et al. *Phys. Rev. C*, Vol. 103, p. 025204, 2021.

[26] T. Miyoshi, et al. *Phys. Rev. C*, Vol. 90, p. 232502, 2003.

[27] F. Dohrmann, et al. *Phys. Rev. Lett.*, Vol. 93, p. 242501, 2004.

[28] F. Dohrmann, et al. *Phys. Rev. C*, Vol. 76, p. 054004, 2007.

[29] S. N. Nakamura, et al. *Phys. Rev. Lett.*, Vol. 110, p. 012502, 2013.

[30] T. Gogami, et al. *Nucl. Instrum. Methods, Phys. Res. Sect. A*, Vol. 900, pp. 69–83, 2018.

[31] T. Gogami, et al. *Phys. Rev. C*, Vol. 94, p. 021302(R), 2016.

[32] T. Gogami, et al. *Phys. Rev. C*, Vol. 93, p. 034314, 2016.

[33] T. Gogami, et al. *Phys. Rev. C*, Vol. 103, p. L041301, 2021.

[34] L. Tang, et al. *Phys. Rev. C*, Vol. 90, p. 034320, 2014.

[35] F. Garibaldi, et al. *Phys. Rev. C*, Vol. 99, p. 054309, 2019.

[36] O. Hashimoto and H. Tamura. *Prog. Part. Nucl. Phys.*, Vol. 57, p. 564653, 2006.

[37] J. Adam Jr., J. Mareš, O. Richter, M. Sotona, and S. Frullani. *Czech. J. Phys.*, Vol. 42, p. 11, 1992.

[38] M. Sotona and S. Frullani. *Progr. Theoret. Phys. Suppl.*, Vol. 177, p. 151, 1994.

[39] Ed V. Hungerford. *Progr. Theoret. Phys. Suppl.*, Vol. 117, pp. 135–149, 1994.

[40] K. Okuyama. *Study of the hyperon electroproduction using the* $p(e, e'K^+)\Lambda/\Sigma^0$ *reaction*. Master thesis, Tohoku University, 2021.

[41] R. Bradford, et al. *Phys. Rev. C*, Vol. 73, p. 035202, 2006.

[42] S. N. Santiestebana, L. Tracy, D. Flay, D. W. Higinbotham, D. Marchand, P. Vernin, and A. Saha. Precise Beam Energy Determination for Hall A after the CEBAF 12 GeV Upgrade. 10 2021.

[43] J. Berthot and P. Vernon. *Nucl. Phys. News*, Vol. 9N4, pp. 12–16, 1999.

[44] R. Cruz-Torres. *Two-Nucleon Short-Range Correlations in Light Nuclei*. Ph.D. thesis, Massachusetts Institute of Technology, 2020.

[45] S. N. Santiesteban, et al. *Nucl. Instrum. Methods, Phys. Res. Sect. A*, Vol. 940, pp. 351–358, 2019.

[46] K. G. Fissum, et al. Vertical drift chambers for the Hall A high-resolution spectrometers at Jefferson Lab. *Nucl. Instrum. Meth. A*, Vol. 474, pp. 108–131, 2001.

[47] M. Iodice, et al. *Nucl. Instrum. Methods, Phys. Res. Sect. A*, Vol. 411, pp. 223–237, 1998.

[48] S. Marrone, et al. Performance of the Two Aerogel Cherenkov Detectors of the JLab Hall A Hadron Spectrometer. *Nuovo Cim. B*, Vol. 124, pp. 99–114, 2009.

[49] D. W. Higinbotham and T. Keppel. 2017 version: Jefferson lab hall a standard equipment manual, 2018.

[50] F. James and M. Roos. *Comput. Phys. Commun.*, Vol. 10, pp. 343–367, 1975.

[51] R. Brun and F. Rademakers. *Nucl. Instrum. Methods, Phys. Res. Sect. A*, Vol. 389, pp. 81–86, 1997.

[52] P.A. Zyla, et al. *Prog. Theor. Exp. Phys.*, Vol. 2020, p. 083C01, 2020.

[53] M. Wang, et al. *Chinese Phys. C*, Vol. 45, p. 030003, 2021.

[54] D. Meekings. Hall a tritium target: Engineering report tgt-rpt-17003.

[55] R. Cruz-Torres, et al. *Phys. Lett. B*, Vol. 797, p. 134890, 2019.

[56] R. B. Wiringa, Steven C. Pieper R. Schiavilla, and J. Carlson. *Phys. Rev. C*, Vol. 89, p. 024305, 2014.

[57] Simc monte carlo. `https://hallcweb.jlab.org/wiki/index.php/SIMC_Monte_Carlo`.

[58] S. Agostinelli, et al. *Nucl. Instrum. Methods, Phys. Res. Sect. A*, Vol. 506, pp. 250–303, 2003.

[59] S. Allison, et al. *IEEE Transactions on Nuclear Science*, Vol. 53, pp. 270–278, 2006.

[60] S. Allison, et al. *Nucl. Instrum. Methods, Phys. Res. Sect. A*, Vol. 835, pp. 186–225, 2016.

[61] M. Vanderhaeghen, et al. *Phys. Rev. C*, Vol. 62, p. 025501, 2000.

[62] C. Ciofi degli Atti, E. Pace, and G. Salme. *Phys. Rev. C*, Vol. 21, p. 805, 1980.

[63] C. Ciofi degli Atti and L. P. Kaptari. *Phys. Rev. C*, Vol. 66, p. 044004, 2002.

[64] C. Ciofi degli Atti and L. P. Kaptari. *Phys. Rev. C*, Vol. 71, p. 024005, 2005.

[65] M. Adbel-Bary, et al. *Eur. Phys. J. A*, Vol. 29, pp. 353–361, 2006.

[66] J. Alcorn, et al. *Nucl. Instrum. Methods, Phys. Res. Sect. A*, Vol. 21, pp. 294–346, 2004.

[67] S. Kato. *Nucl. Instrum. Methods, Phys. Res. Sect. A*, Vol. 611, pp. 1–13, 2009.

[68] W. Verkerke and D. Kirkby, 2003. arXiv:physics/0306116.

[69] F. James. *Statistical Methods in Experimental Physics 2nd Edition*. World Scientific, 2006.

[70] Y. Akaishi, T. Harada, S. Shinmura, and Khin Swe Myint. *Phys. Rev. Lett.*, Vol. 84, p. 3539, 2000.